SANDIA REPORT

SAND94—0024 • UC—902
Unlimited Release
Printed October 1994

Lidar Technologies for Airborne and Space-Based Applications

Tammy D. Henson, Randal L. Schmitt, Tim J. Sobering,
Thomas D. Raymond, David A. Stephenson

Prepared by
Sandia National Laboratories
Albuquerque, New Mexico 87185 and Livermore, California 94550
for the United States Department of Energy
under Contract DE-AC04-94AL85000

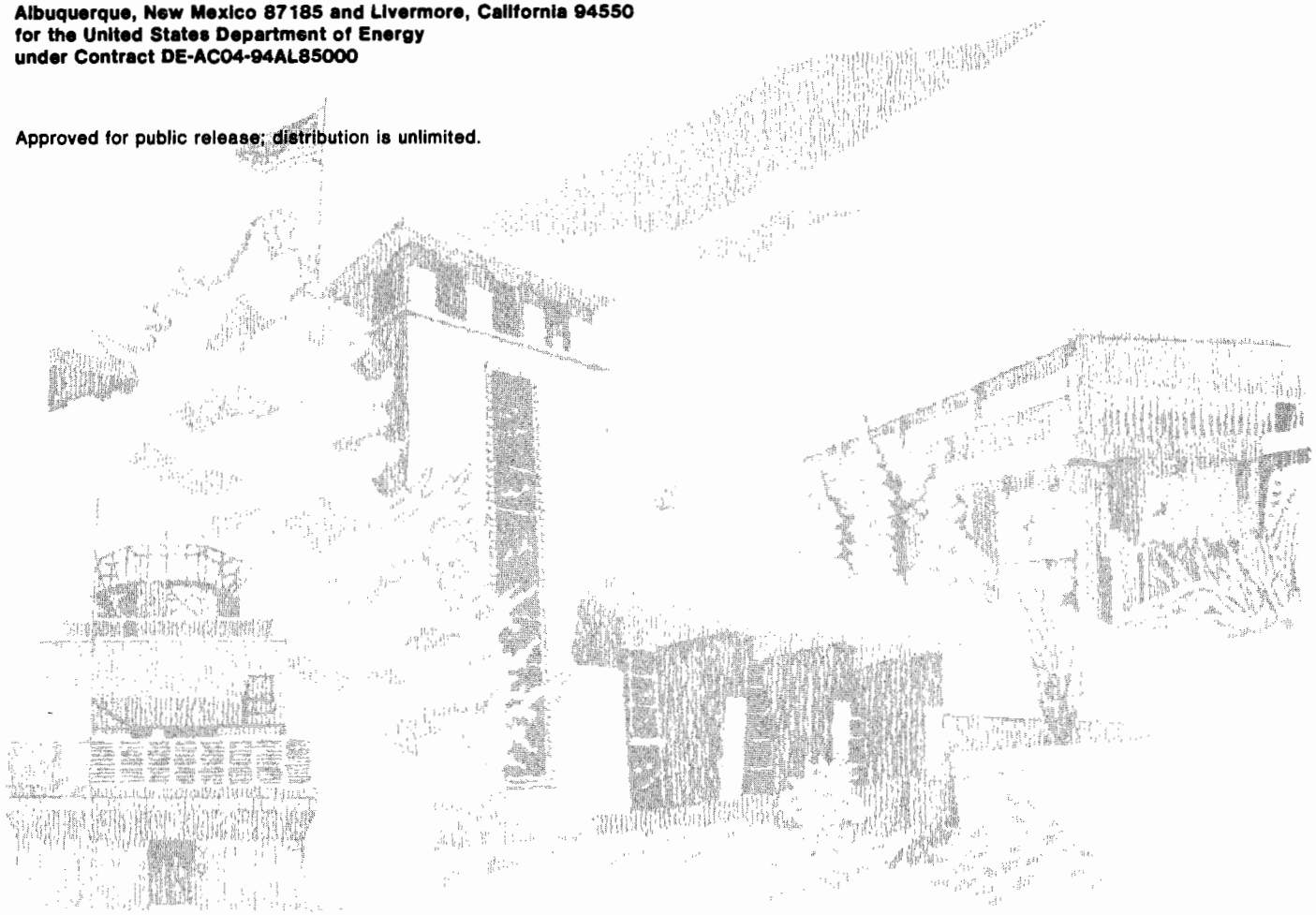

SF2900Q(8-81)

Issued by Sandia National Laboratories, operated for the United States Department of Energy by Sandia Corporation.

Available to DOE and DOE contractors from
Office of Scientific and Technical Information
PO Box 62
Oak Ridge, TN 37831

Prices available from (615) 576-8401, FTS 626-8401

Available to the public from
National Technical Information Service
US Department of Commerce
5285 Port Royal RD
Springfield, VA 22161

NTIS price codes
Printed copy: A06
Microfiche copy: A06

SAND94-0024
Unlimited Release
Printed October 1994

Distribution
Category UC-902

Lidar Technologies for Airborne and Space-Based Applications

Tammy D. Henson
Optics and Exploratory Technologies Department

Randal L. Schmitt
Optoelectronic Applications Department

Tim J. Sobering
Sensors and Electronics Department

Thomas D. Raymond
Laser, Optics and Remote Sensing Department

Sandia National Laboratories
Albuquerque, NM 87185

David A. Stephenson
Exploratory Systems Department
Sandia National Laboratories
Livermore, CA 94550

Abstract

This study identifies technologies required to extend the capabilities of airborne light detection and ranging (lidar) systems and establish the feasibility of autonomous space-based lidars. Work focused on technologies that enable the development of a lightweight, low power, rugged and autonomous Differential Absorption Lidar (DIAL) instruments. Applications for airborne or space-based DIAL include the measurement of water vapor profiles in support of climate research and processing-plant emissions signatures for environmental and nonproliferation monitoring. A computer-based lidar performance model was developed to allow trade studies to be performed on various technologies and system configurations. It combines input from the physics (absorption line strengths and locations) of the problem, the system requirements (weight, power, volume, accuracy), and the critical technologies available (detectors, lasers, filters) to produce the best conceptual design. Conceptual designs for an airborne and space-based water vapor DIAL, and a detailed design of a ground-based water vapor DIAL demonstration system were completed. Future work planned includes the final testing, integration, and operation of the demonstration system to prove the capability of the critical enabling technologies identified.

Acknowledgment

The authors thank M. W. Kimmel of the Laser, Optics and Remote Sensing Department for the considerable effort he contributed in the implementation of the Ti:sapphire ring laser and the overall mechanical design and packaging of the water vapor DIAL demonstration system. The authors also thank S. E. Bisson of the Diagnostic and Reacting Flow Department for his help in designing the injection-seeded Ti:sapphire ring laser for the water vapor DIAL demonstration system.

Contents

Figures

This page intentionally left blank.

Tables

This page intentionally left blank.

Lidar Technologies for Airborne and Space-Based Applications

Introduction

The need for airborne and satellite-based measurement systems which provide broad-area mapping (horizontal and vertical) on local, regional, and global scales is without question in the environmental monitoring, climate change research, and space exploration communities. The resolution, coverage, and the unambiguous nature of the measurements attainable with a light detection and ranging (lidar) system are highly desired by investigators supporting arms control and treaty verification as well as civilian and defense meteorological missions.

Thus far, the restrictions of cost, size, weight, lifetime, operability, reliability, and deployment range have limited the proliferation of lidar systems and hence the availability of their highly-valued measurements. However, advances in many lidar-related technologies are rapidly making the development of such systems attractive. The goal of this laboratory directed research and development (LDRD) project was to develop system design concepts and prove certain critical technologies that will extend the capabilities of current lidar systems for environmental monitoring, climate change research, nonproliferation, and other applications requiring small, rugged, autonomous, low-power, lightweight, flight-worthy instrumentation. For the purposes of this LDRD project, the intended platforms for the lidar system are unmanned aero-vehicles (UAVs) and small satellites.

Boundary Conditions

From the beginning of this LDRD project, we imposed a number of boundary conditions to ensure that the conceptual designs we authored would be applicable to UAV and satellite operating environments. Some of these self-imposed boundary conditions were:

- The size, weight, power consumption and other goals or specifications that we established for this project must be compatible with small UAV or small satellite platforms. Our initial goals were 100 W power consumption, 100 kg mass, and 0.5 m^3 volume.

- Since we anticipate designing and building flight-worthy hardware in the next several years, we only considered using technology mature enough to be implemented in the next year or two. That is, we did not consider speculative technologies (such as new, unproved laser systems) which offer the promise of improved performance unless we were confident that these technologies would be

available by the time we need to freeze the hardware for engineering design of the instrument package. The emphasis of this LDRD was to develop design concepts, and, if possible, demonstrate key technologies (lasers, filters, detectors) that enable a new generation of lidar system using the best technology available today.

- The components chosen for the lidar must be compatible with aircraft (and eventually spacecraft) environments. For example, we did not consider technologies or devices that cannot withstand the vibration environment in a typical UAV or that require special facilities or equipment not available on small UAV or small satellite platforms.

Tasks

The tasks we set out to accomplish for this LDRD project were:

- Determine which lidar technologies are technically feasible for a very small package and those which will provide measurements that are useful to the climate community.

- Find the state-of-the-art in laser, detector, filters, and signal processing technologies that can be used in the design and construction of small lidar instruments.

- Develop a computer model to simulate the performance of strawman lidars based on the available technologies.

- Determine the pacing items on the engineering and construction of the strawman lidar(s)

- Demonstrate viable (hardware) solutions to the pacing items in a non-optimized ground-based Differential Absorption lidar (DIAL) system

Application Search

In order to find the best lidar application in which to focus our LDRD project, we conducted a literature search. We looked for all the applications that lidar has been used for thus far including ground-based, air-based, and space-based lidar systems. Appendix C contains a list of the lidar applications that we found. From this rather long list, we searched for applications that required global coverage or large area coverage and, thus, could take advantage of an air-based or space-based platform. We also looked for an application that would be of interest to the general scientific community and have the potential for a large number of customers.

In addition to the literature search, we informally surveyed several SNL employees (John Vitko, Marshall Lapp, Larry Thorne, John Goldsmith, and Andy Boye) who are active in the Global Climate Change area to get their opinions concerning the best lidar

technology to target for this LDRD project. Our decision to concentrate all of the efforts of this LDRD project on water-vapor DIAL technology was based on the following arguments:

- Water vapor is probably the most important driver of climate through its interaction with radiation and the heat balance of the earth. For example, clouds both trap radiation in the atmosphere and shield the earth from the sun's radiation. Also, water vapor is probably the most variable (and unpredictable) component of the earth's atmosphere - both in space (geographical location) and time. For these reasons, climate scientists are very interested in measuring water vapor profiles. A miniature instrument operating from a UAV or satellite platform could provide both large-area coverage and long-term coverage to provide water vapor data needed for Global Circulation Models or other climate models. *Thus, we think that water vapor measurements have important customers whose instrumentation needs have not yet been met.*

- A number of other laboratories have, over the past twenty years or so, built a wide variety of lidar systems including land-based and airborne instruments. However, we are not aware of any miniature water vapor DIAL systems that are operating now (although we recognize that miniature DIAL systems are being proposed and designed by NASA and others). Most, if not all, of the so-called miniature lidars built to date have been simple backscatter lidars designed to measure cloud top heights or for rangefinding applications. *Thus, we feel that if we were to develop a miniature DIAL system, it would provide a unique capability, not presently available to the scientific community.*

- Recent developments in laser technology (especially diode-laser-pumped solid-state lasers) have made miniaturization of sophisticated laser systems realistic. The size, weight, and power efficiency of modern laser systems is consistent with miniaturization. *Thus, a miniature lidar for measuring water vapor is technically feasible.*

Since the DIAL technique yields species-specific information, it is potentially useful for remote measurements of chemical species other than water. Thus, another reason we have chosen to focus our efforts on miniature DIAL systems is that we anticipate other applications (such as pollution detection and non-proliferation detection/verification) will become important in the future. In fact, partially as a result of this LDRD effort, a multilaboratory program called CALIOPE (chemical analysis by laser interrogation of proliferation effluents) was initiated. CALIOPE uses lidar systems, including DIAL, for non-proliferation detection and verification.

Lidar Definition and Description

The acronym *LIDAR* stands for light detection and ranging. Much the same as its radio-wave counterpart, *RADAR*, a lidar system sends out a pulse of light (usually from a pulsed laser) to probe a remote atmosphere. Usually, a telescope and a high-speed

photodetector are used to measure the backscattered light as a function of time. By temporally resolving the return signal, one can infer spatial information about the scattering properties of the probed atmosphere. Perhaps the simplest application of a lidar system is rangefinding - sending out a probe pulse and measuring the time it takes to get a very strong return signal from a target. Rangefinding lidars are used in such diverse applications as measuring the distance from the earth to the moon, measuring the height of cloud tops, or measuring the distance from a spacecraft to a planetary surface. Often rangefinding lidars are called LADARs (laser detection and ranging) especially when they are used to find the range to a hard target. However, the distinctions between lidar, LADAR, and laser radar are fuzzy at best. Lidars have been built using Rayleigh and aerosol scattering, fluorescence, and Raman scattering to determine various atmospheric properties. In the case of a water vapor DIAL system, we will measure the water vapor concentration as a function of distance from the lidar.

To the reader interested in a thorough treatment of lidar in its many forms and applications, the authors recommend the book by Raymond M. Measures entitled Laser Remote Sensing: Fundamentals and Applications[1]. Also, a good general review article on laser sensing of the atmosphere was written by She[2].

DIAL Technique

With a simple backscatter lidar, there is no species-specific information in the return signal. Also, it is nearly impossible to make absolute concentration measurements with only a single-wavelength return signal since many of the optical properties of the atmosphere are not known with great precision. In order to measure the absolute quantity of water vapor in the air, one must be able to distinguish the return signal due to water from the return signal due to air. There are a number of different lidar techniques that can accomplish this. Raman lidar, for example, measures water vapor density by detecting the Raman-shifted light from water vapor. By taking the ratio of the Raman-scattered water vapor signal to the nitrogen signal, the Raman lidar technique can directly measure the ratio of water vapor density to air density (called the mixing ratio). Unfortunately, the Raman-scattering cross sections are very weak ($\sigma \sim 10^{-30}$ cm^2), and Raman lidar systems require large lasers, photon-counting receivers, and relatively long integration periods to obtain useful data. Due to the weak return signal strength and competition from solar radiation, it is extremely difficult to make Raman lidar measurements in the daytime.

The differential absorption lidar (DIAL) technique measures water vapor concentration by comparing the lidar return signal at two laser wavelengths. One wavelength is tuned to a water vapor absorption line, and, as a result, is attenuated as it travels through the atmosphere. The other wavelength is tuned off the water vapor absorption, but still close enough in wavelength to the on-line wavelength that all other optical properties of the atmosphere are the same for the two pulses. The only difference between the return signals from the two pulses is due to absorption of water

vapor. By comparing the return signals at these two wavelengths, one can determine the concentration of water vapor without detailed knowledge of the optical properties of the atmosphere.

Implementation of DIAL requires transmission of two different laser wavelengths separated sufficiently in time so that the backscattered return signals from the two are not overlapped (since the same detection system is usually used for both signals), yet close enough that the atmosphere has not changed during that interval. In practice, the on-and off-wavelength pulses are spaced from 100 μs to 300 μs apart. For the case of DIAL instrument flying at 15 km altitude, the pulses should be spaced at least 100 μs so that the return signal from the earth's surface due to the first pulse does not overlap with the high-altitude return signal from the second pulse.

In most DIAL systems described to date, the on and off wavelengths are generated by identical but separate laser systems. This allows ease of arbitrary pulse separation in both time and wavelength. However, this approach is somewhat wasteful in terms of size, weight, power consumption, and cost, since it requires two of everything. In this LDRD project, we propose a laser configuration in which a single laser system is capable of producing both the on and off wavelengths with the required temporal separation between them.

Since the on and off wavelengths are only separated by ~0.1 nm or less, standard interference filters (with bandpass of 0.3 nm FWHM) may be used to pass the return signals while rejecting background light. However, the return signals we expect are very weak, and more sophisticated filtering techniques which have narrower bandpass and higher optical throughput could potentially increase the sensitivity of the instrument. In particular, we will be investigating the applicability of anomalous dispersion optical filters (ADOFs) and Fabry-Perot interferometers in a miniature DIAL system.

In an effort to optimize the DIAL signal (and minimize the DIAL measurement error), any DIAL system must be able to operate on more than one absorption line. It is usually possible to find a number of suitable DIAL absorption lines with varying strengths. The optimum line to use will depend on the local humidity, the maximum range that one would like to profile, and whether the lidar is at high altitude looking down (as in the intended applications) or whether it is on the ground looking up (as it must be for proof-of-principle experiments and ground testing). As a result, the DIAL system must be flexible enough to change its operation wavelengths during a measurement period. This implies that the laser must be tunable enough to reach all of the needed absorption lines, and the filter used for the detection system must be wide enough to pass the lines.

The laser used for the on wavelength must have very narrow linewidth. The water vapor lines we are considering have absorption linewidths on the order of 0.2 cm^{-1}

FWHM (6 GHz or about 0.010 nm at 725 nm) at STP. Since the pressure and temperature of the atmosphere vary with altitude, the water vapor absorption line positions (frequencies) and linewidths vary with altitude. At high altitudes, the linewidths narrow considerably. (At an altitude of 10 km, the linewidths of the water vapor transitions will be approximately 0.3 of their sea-level values.) In addition, the transition frequencies vary with pressure (altitude), placing additional demands on the shot-to-shot frequency jitter of the laser. Finally, the laser output must have very high spectral purity or the effective differential absorption cross section will be lowered (and its value uncertain). In practice, the laser energy of the broadband emission (outside of the desired linewidth) due to amplified spontaneous emission (ASE) must be less than 1% of the total output energy[3]. The high spectral purity required for water vapor DIAL is especially hard to meet with dye lasers, but has been achieved using tunable solid-state lasers. Ismail and Browell have written an excellent analysis of the origins and magnitudes of errors in DIAL measurements[3] including those generated by uncertainty and jitter in the laser frequency, and spectral purity.

Technology Trade Studies

The critical enabling technologies identified include tunable solid-state lasers, narrowband optical filters, and high-performance optical detectors. A search was conducted to determine the most likely laser, filter, and detector candidates for a water vapor DIAL system. Trade studies were performed on the available technologies to determine which critical technologies produced the best overall performance.

Laser Search

A candidate laser system must meet several requirements before it can be considered for use in this miniature DIAL project:

- The laser architecture chosen must be flight-worthy now and space-worthy in the future. The laser must be able to withstand take-off and landing shock and vibration, and must be able to operate in the vibration / temperature / pressure environment of a UAV.

- The laser system must be extremely energy efficient. Although UAV platforms typically have much more power available than the 100-W goal that we set in our ground rules, small satellite platforms will not have power to waste. Moreover, in a satellite, getting rid of the heat generated by an inefficient laser can be a bigger problem that obtaining the power in the first place.

- The laser system must be very compact. The volume of the cargo bay for a small UAV and a small satellite are comparable - on the order of 0.5 m^3. In fact, volume constraints are probably more stressing than power consumption or weight for both platforms.

- The laser must be tunable over several different water vapor absorption lines suitable for DIAL measurements. Although broadly tunable lasers such as Ti:sapphire are natural candidates, other laser systems such as Tm:Ho:YAG can be tuned over a few water vapor lines, and must at least be considered for this project.

- The lasers considered for this project must be technologically mature enough that the design of the laser system can be frozen in the next year or so. This requirement ensures that a working lidar can be designed, engineered, built, and tested in a very short time frame.

Since the first lidar systems were designed nearly 30 years ago, solid-state lasers have been the backbone of most working lidars. Q-switched solid-state lasers (such as ruby and Nd:YAG) provide relatively high output energies and short pulse lengths ideal for range-resolved lidars. Today, laser systems for water-vapor-measuring DIAL systems usually consist of frequency-doubled Nd:YAG lasers pumping tunable dye lasers or Ti:sapphire lasers. Some water vapor DIAL systems have also been built with flashlamp-pumped alexandrite lasers. Recent progress in high-power diode laser pump technology enables a new generation of compact, efficient lasers for use in lidar systems. The following section describes some of the candidate laser systems that were considered for this LDRD project.

The ideal laser system for a miniature DIAL system is an all-solid-state tunable laser system. All-solid-state laser systems are inherently more rugged than gas-filled or liquid-based lasers and are generally more compact and more reliable. Candidate laser systems that were seriously considered for our water-vapor DIAL system were:

- Tm:Ho:YAG (directly pumped by diode lasers)

- Cr:LiSAF (directly pumped by diode lasers)

- Ti:sapphire (pumped by a frequency-doubled diode-pumped Nd:YAG laser system)

The overall operating efficiency of a laser system is of prime importance in our application. An efficient laser not only consumes less power, but it generates less heat (which must be removed by systems that usually consume power themselves). Probably the most important recent development in laser technology is the development of high-power laser diodes for pumping of solid-state lasers[4]. The diode lasers themselves are very efficient, with 50 to 60% conversion of electrical power to optical power. Since the output of a laser diode is spectrally narrow, it can be well matched to absorption features in solid-state laser materials, improving the efficiency of the optical-to-optical conversion in the laser, thereby reducing the waste heat generated in the solid-state laser material. For example, the optical-to-optical energy transfer for diode-laser-pumped Nd:YAG is approximately three times that for flashlamp-pumped Nd:YAG.

Tm:Ho:YAG operating at 2.1 μm is an attractive laser material for miniature lidar applications because it can be directly diode pumped (and is therefore very efficient), and its output wavelength is in the so-called eye-safe region of the spectrum[5-8]. To date, Tm:Ho:YAG lasers have been used for water-vapor DIAL systems[9] and coherent lidars for wind-shear detection[10]. We were originally attracted to the Tm:Ho:YAG laser system due to its high wall-plug efficiency of ~6%. That is, for 100 W of electrical power into the laser, it produces 6 W of average optical power at 2.1 μm. This is approximately the same wall-plug efficiency as can be obtained from a diode-laser-pumped Nd:YAG laser operating at 1.06 μm.

Unfortunately, there are no detectors with internal gain for the 2-μm wavelength region, and, for the return signal levels we anticipate, internal gain is required to overcome the noise in the electronic amplifiers. Also, the Tm:Ho:YAG laser is not tunable enough to access DIAL lines suitable for UAV deployment. Demonstration of a Ho-based laser system for water-vapor DIAL has been conducted at sea level using a horizontal path[8,9]. The water-vapor lines that Ho-based lasers can access may be strong enough for these horizontal paths near sea level, but our simulations have shown that they are not strong enough to make accurate DIAL measurements high in the atmosphere.

Another direct diode-laser-pumped laser, Cr:LiSAF, shows great promise for miniature lidar systems due to its efficiency and simplicity. It is a tunable material which can operate in the 940-nm region of the water spectrum[11]. Traditionally, Cr:LiSAF has been pumped by flashlamps, but recently LLNL has proposed and demonstrated direct diode pumping of the material[12]. The pump band of Cr:LiSAF just barely overlaps with the shortest wavelength available from AlGaAs laser diodes (the most efficient of the high-power laser diodes), and, as a result, the material must be very heavily doped with Cr in order to efficiently absorb pump light from the diode laser. Since LLNL is still developing both the Cr:LiSAF laser material and the diode lasers needed to pump it, Cr:LiSAF is not a good choice for our proposed water vapor DIAL system - the laser is not far enough along its development path and it is not generally available for our use. Nevertheless, directly diode-pumped Cr:LiSAF is a material which may play an important role in miniature DIAL systems in the future, and we should continue to keep abreast of new developments on this laser system.

Titanium-doped sapphire (Ti:Al_2O_3) is a broadly tunable solid-state laser material[13]. Its tuning range of 700 nm to 1000 nm overlaps with three important regions of water vapor absorption: the 727-nm, 817-nm, and 940-nm regions of the spectrum contain numerous water vapor absorption lines that are suitable for DIAL measurements. Indeed, NASA researchers have already used Ti:sapphire lasers in their water-vapor DIAL systems, and are planning to use the material in future DIAL projects.

Pulsed Ti:sapphire lasers are usually pumped at 532 nm with frequency-doubled Q-switched Nd:YAG lasers. Since diode-laser-pumped Nd:YAG lasers are beginning

to appear as commercial products, the possibility of an all-solid-state DIAL laser system based on Ti:sapphire is very real.

The primary disadvantage of the Ti:sapphire laser is its relatively low wall-plug efficiency (when compared to the lasers discussed previously). The diode-laser-pumped Nd:YAG laser can produce light at 1.06 μm with between 6% and 8% wall-plug efficiency. The frequency doubling process can convert between 50% and 60% of this infrared light to 532-nm light. The optical-to-optical conversion efficiency in the Ti:sapphire oscillator is between 30% to 40%. This results in a wall-plug efficiency for the entire Ti:sapphire laser system of between 1% and 2%. Thus, if we allow the entire 100 W power budget to be spent on the Ti:sapphire laser system, it would only buy between 1 and 2 W of average optical power for the DIAL measurements. This efficiency figure does not include power which must be expended for the injection seeding laser, the cavity-length stabilization, or any of the other support electronics that may be needed to operate the laser in a DIAL system.

In spite of its relatively poor efficiency, the Ti:sapphire laser remains the best choice for near-term miniature DIAL systems. The material is broadly tunable, allowing access to many water vapor lines (and absorption lines from other molecules as well). Due to its popularity, Ti:sapphire crystals are being produced with excellent optical quality, and many of the commercial laser companies are selling Ti:sapphire lasers as standard products.

Incoherent Detection versus Coherent Detection

There are basically two ways to convert the optical return signal from a backscatter lidar to an electrical signal. (See references 14 and 15 for detailed discussions of light detection.) The simplest method, direct detection, records the intensity of the return light using a photodetector such as a photomultiplier tube (PMT) or avalanche photodiode (APD). This method is also called incoherent detection since all phase information on the return signal is lost in the photodetection process. With heterodyne detection, the optical return signal is summed with a reference optical signal on the photodetector surface, producing an electrical output signal which retains both amplitude and phase information contained in the return beam. Usually, the reference optical signal is offset in frequency $\Delta\nu$ from the signal beam, and, as a result, the signal at the output of the heterodyne detector is an amplitude-modulated sinusoid at the beat frequency $\Delta\nu$. It is also possible to have a frequency offset of $\Delta\nu = 0$, and this is called homodyne detection.

For any detection scheme, the fundamental limit to the detection sensitivity is shot noise in the photon signal itself. The photon-shot-noise limit of detection is difficult to achieve in practice due to noise in the detector circuit and amplifier electronics. In direct detection schemes, the circuit and amplifier noise can often be overcome by careful use of a detector with internal gain (such as a PMT or APD). The optimum level of internal gain is reached when the shot noise due to the signal current, background

current, and leakage currents are multiplied to a level equal to the noise of the external circuit and amplifier[15]. Above this level of gain, the excess noise in the gain process reduces the sensitivity of the measurement.

In the infrared region of the spectrum, detectors with internal gain are not available and coherent detection is often used to provide nearly photon-shot-noise-limited sensitivity. Heterodyne detection can be thought of as a process where the reference laser field provides virtually noiseless "gain" to elevate the signal level above the noise of the circuit and amplifier. The reference laser power is chosen to be high enough so that the shot noise due to the reference laser photocurrent dwarfs all other sources of noise, including thermal noise, dark current noise and amplifier noise. Under these conditions, the signal-to-noise ratio is nearly equal to the quantum limit. That is:

$$\mathrm{SNR} \approx \frac{2\eta P_s t}{h\nu}$$

where η is the detector quantum efficiency, P_s is the optical power of the lidar return signal, h is Planck's constant, ν is the optical frequency of the light and t is the interval over which the measurement is performed.

For a detector with a quantum efficiency of 50%, this corresponds to a detection limit of one photon per measurement time t = 1/2B. (B is the measurement system electrical bandwidth.) In practical backscatter lidar systems, this ultimate detection limit is very difficult to achieve, primarily due to atmospheric index-of-refraction turbulence, slight mismatches between the reference and signal wavefronts at the detector plane, laser speckle, and beam truncation effects. Nevertheless, coherent detection systems will almost always outperform direct detection systems in the infrared where detectors with internal gain are not available.

Following the discussion in reference 14, we compare the SNR for several detection schemes. If $\overline{m}$ is the mean number of photoelectrons counted in resolution interval t = 1/2B then, for heterodyne detection, the signal-to-noise ratio is given by

$$\mathrm{SNR} = 2\overline{m}.$$

For direct detection (measuring the same signal current) using a detector with no internal gain, the SNR is given by:

$$\mathrm{SNR} = \frac{\overline{m}^2}{\overline{m} + \sigma_q^2}$$

where σ^2_q represents the circuit noise variance. Thus, even for noiseless detection electronics, the SNR for coherent detection is a factor-of-2 greater than for direct detection. The advantages of coherent detection become even greater when the system must measure small optical signals or the circuit and amplifier noise is not negligible.

For these (real-world) cases, the SNR is significantly reduced by the circuit and amplifier noise contributions.

The SNR for an avalanche photodiode under these conditions is given by:

$$\mathrm{SNR} = \frac{\overline{m}}{\mathrm{F}}$$

where F is the excess noise factor for the APD. Since F > 1, coherent detection also outperforms direct detection with internal gain.

Although heterodyne detection is fundamentally more sensitive than direct detection, it is much more difficult to apply, especially at wavelengths in the near infrared and in the visible. Both the probe laser frequency and the reference laser frequency must be very narrow-linewidth (long coherence length), frequency-stable sources. In addition, the spatial beam quality of both beams must approach the diffraction limit and must be very precisely aligned on the detector with flat phase fronts in the detector plane. For coherent lidar applications, atmospheric refractive index turbulence limits the useful collecting aperture. Unfortunately, at shorter wavelengths, the maximum useful aperture decreases since the phase shift the optical beam experiences traversing an index-of-refraction inhomogeneity is inversely proportional to wavelength. In spite of these difficulties, in regions of the spectrum where detectors with internal gain are not available (lack of photomultipliers at 10 μm, for example), heterodyne detection is clearly the method of choice, allowing nearly shot-noise-limited measurements of lidar return signals. Moreover, coherent detection is required in systems designed to measure wind velocity.

Coherent lidars have been demonstrated in the 10-μm and the 2-μm regions of the spectrum[10,16-19]. The main difficulties in modeling the performance and optimizing the signal-to-noise ratio of these coherent lidars lie in modeling atmospheric refractive-index turbulence. There are several excellent references that provide detailed models to predict system SNR for a variety of conditions[17-19]. In particular, reference 19 presents results for 2.1-μm coherent lidar similar to the one we are contemplating.

Detector Search

In many lidar applications, the return signals are very weak. This is particularly true in DIAL systems, where the laser is tuned to an absorption line of a molecule. The return signal is even weaker for an aircraft or satellite-based DIAL where the system must operate over very large ranges (return signal is inversely proportional to the range squared). In order to detect these very weak signals, the detector chosen must have high quantum efficiency at the DIAL wavelengths, low noise, low capacitance, and in many instances, internal gain. Low capacitance is necessary to keep the amplifier noise low, and internal gain is necessary to boost the DIAL signal above the amplifier noise.

In addition, the detector must be of a sufficient size to accommodate the field-of-view requirements for the DIAL system.

Once the laser search was completed and the most likely laser candidates identified, a search was conducted to find the best detector candidates for the Tm:Ho:YAG, the Ti:sapphire, and the Cr:LiSAF lasers at the water vapor DIAL wavelengths 2.1 μm, 727 nm, 817 nm, and 940 nm respectively. Several detectors were evaluated for these water vapor lines based on the criteria listed above. The Tm:Ho:YAG laser, which operates at 2.1 μm, was the system we decided to concentrate on first since it was directly diode pumped and was more technologically mature than the Cr:LiSAF laser.

There are currently no detectors available with internal gain at 2.1 μm. Therefore, several detectors were chosen based on their responsivity, noise, and capacitance. The detectors evaluated were liquid-nitrogen-cooled InAs, InSb with cold filter, HgCdTe, doped Ge photodiodes, and room-temperature and thermoelectrically cooled InGaAs pin photodiodes. The noise equivalent power (NEP=noise/responsivity) of the liquid-nitrogen-cooled InAs and InSb with cold filter were comparable to each other and to the room-temperature InGaAs pin photodiode. However, the capacitance of the InGaAs photodiode was somewhat smaller. The NEP's of the liquid-nitrogen-cooled HgCdTe and doped Ge photodiodes were about an order-of-magnitude higher than the above detectors at 2.1 μm. The lowest NEP and the lowest capacitance was obtained from the thermoelectrically cooled InGaAs pin photodiode which was determined to be the best available detector for the 2.1-μm water vapor DIAL.

A meeting was held on March 12, 1992 with several members of the Sandia Detector Research group to determine additional methods to improve the performance of the thermoelectrically cooled InGaAs pin photodiode or to seek out detectors or methods to improve the performance at 2.1 μm. They suggested that in the short term one may be able to improve the performance of the InGaAs detector by cooling it to lower temperatures or by performing surface passivation (a process in which an electrochemically grown sulfur film reduces the leakage current of the detector). In the long term, they suggested that porous silicon (the silicon is etched to change the bandgap structure and increase the efficiency by an order of magnitude) may improve detector performance at 2.1 μm. They also suggested a high electron mobility phototransistor (HEMPT) structure in which one launches the lightwave into a waveguide. High electron mobility transistors (HEMTs) are low-noise heterostructure transistors but have not previously been applied as phototransistors.

Both avalanche photodiodes (APDs) and photomultiplier tubes (PMTs) operate with internal gain at 727 nm. The detectors evaluated for use at 727 nm were a silicon APD, a tri-alkali PMT, and a GaAs:Cs-O PMT. In general PMTs have higher internal gain and lower noise than APDs. Also the internal gain of a PMT is a nearly noiseless process, and, as a result, the signal-to-noise ratio will not be degraded by the excess noise factor as in an APD. On the other hand, silicon APDs have much higher quantum efficiencies at 727 nm than the PMTs, and have a much larger dynamic range making

them less susceptible to saturation. Another possible advantage of an APD over a PMT is that APDs are not sensitive to magnetic fields while PMTs are. This could be a significant problem if a magnetic-field-producing device (such as a Faraday Isolator) is located near the detector.

Since both PMTs and APDs have advantages and disadvantages at 727 nm, it is impossible to make a decision simply looking at their specification sheets. Therefore, these three detectors were evaluated based on how they affected the overall performance of the DIAL system (as predicted by using a computational model). This evaluation showed that the tri-alkali PMT did not perform as well as the silicon APD because of its very low quantum efficiency (3%) at 727 nm. The GaAs:Cs-O PMT performed slightly better than the silicon APD because it has a moderate quantum efficiency (15%) at 727 nm and very low noise, where the APD has high quantum efficiency (80%) at 727 nm but fairly high noise. However, the GaAs:Cs-O PMT does not have a large enough dynamic range for the DIAL system. Therefore, the GaAs:Cs-O PMT will not be reasonable to use for this DIAL application, and the best choice for a water vapor DIAL detector at 727 nm is the silicon APD.

Both PMTs and APDs are available for the 817-nm region as well. However, the quantum efficiencies for the PMTs are down slightly to 1% for the trialkali PMT and 10% for the GaAs:Cs-O PMT, while for the APD the quantum efficiency is up to 85%. Because of its very high quantum efficiency, the silicon APD is the best choice for a water vapor DIAL detector at 817 nm.

Most PMTs do not respond at wavelengths of 940 nm or longer. The ones that do respond in this spectral region have such low quantum efficiencies (< 0.1%) that they can be eliminated from consideration immediately. Because silicon APDs have very high quantum efficiencies (85%) at 940 nm, and they have internal gain to raise the system noise above the amplifier noise, they are the clear (if not the only) choice for a water vapor DIAL detector at 940 nm.

Filter Search

Solar background radiation is often the main noise source in a DIAL system, and it will completely mask the signal in an unfiltered system. Therefore, one must take drastic measures to reduce the solar background radiation enough to be able to detect and measure the DIAL signals.

Fortunately, the DIAL wavelength is known very precisely, allowing the use of a very narrowband filter centered on the DIAL wavelength to reduce the solar background. The filter chosen must have a very narrow bandwidth with high throughput so as not to reduce the weak DIAL signal. The filter must also be able to pass the on-line and the off-line DIAL wavelengths as well as several on-line DIAL wavelengths in order to profile different layers of the atmosphere. If the filter bandwidth is not wide enough to accomplish this, or if the bandwidth can't be tuned to accomplish this, then several

filters must be switched in and out to profile the water vapor in the atmosphere. In addition, the filters must be robust and capable of operating autonomously from an airborne or spaceborne platform.

Three types of filters were evaluated for the water vapor DIAL system: multilayer dielectric interference filters, anomalous dispersion optical filters (ADOFs), and Fabry-Perot etalons. The simplest of these filters are multilayer interference filters, which appear to be the best candidate narrowband filters for an airborne water vapor DIAL system. They consist of multiple layers of thin, nonabsorbing, dielectric films deposited on a glass substrate. The bandwidth at a given wavelength for a given combination of dielectrics is logarithmically related to the number of layers in the filter. The thickness of the layers controls the central or peak wavelength. The narrowest bandpass obtainable interference filters is typically from 0.1% to 1% of the center wavelength. At the 727-nm DIAL wavelength the best commercially available interference filter has a bandwidth of 0.3 nm with a minimum of 36% throughput, and at the 817-nm and 940-nm DIAL wavelengths the best commercially available interference filter has a bandwidth of 1 nm with a minimum of 45% throughput. At night, when there is no solar background, it is better to use an interference filter with a 10-nm bandwidth and a minimum of 60% throughput for the 727-nm, 817-nm, and 940-nm DIAL wavelengths. At the 2.1-μm DIAL wavelength, the best interference filter has a bandwidth of 20 nm and a throughput of only 50%. These bandwidths are large enough to pass both the on-line and the off-line DIAL wavelengths, and may be able to pass several on-line DIAL wavelengths depending on the wavelengths chosen. Since the center wavelength is a function of the thickness of the dielectric film layers, a temperature controller may be necessary to keep the filters centered on the DIAL wavelength under various operating conditions.

The second type of filter we considered for use in the water vapor DIAL instrument was the anomalous dispersion optical filter (ADOF). It is a new type of narrow-bandwidth, high-background-rejection optical filter that was developed for use in free-space communications[20,21]. This filter may play a critical role in the implementation of lightweight, low-power-consumption, autonomous lidar systems. The ADOF relies on dispersion near optical absorptions to create a filter with an equivalent bandpass of 3 - 5 GHz (0.006 to 0.01 nm at 800 nm). Since ADOFs provide more than an order-of-magnitude narrower bandwidth than dielectric interference filter technology, they represent an exciting opportunity for improving the performance of lidar systems, especially satellite-based lidars that receive extremely low signal levels.

The first ADOF described in the literature was based on the Faraday effect and was termed a Faraday anomalous dispersion optical filter (FADOF). The FADOF, shown schematically in Figure 1, consists of a cell of atomic vapor (such as sodium or cesium) in a d.c. axial magnetic field and a pair of crossed polarizers. The device relies on the resonant Faraday[22] effect which causes a rotation of the polarization of light passing through the atomic vapor for optical frequencies near absorption transitions of the atom. The axial magnetic field causes the absorption lines of the atom to split into two

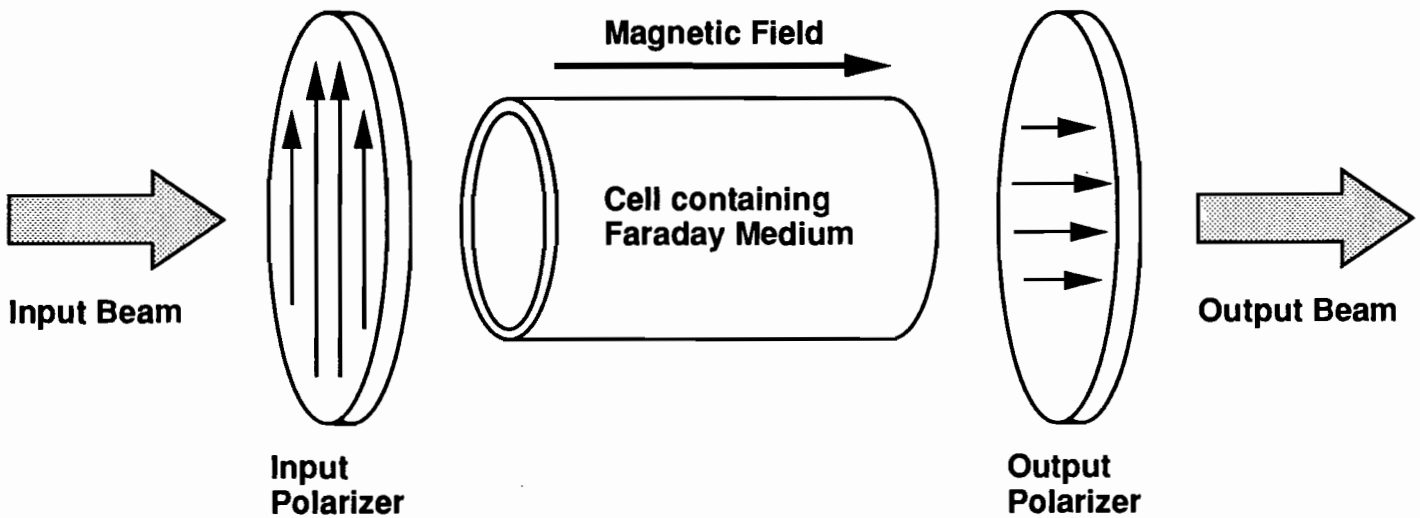

Figure 1. Schematic of a Faraday Anomalous Dispersion Optical Filter (FADOF). The FADOF consists of a cell containing an atomic or molecular gas placed between crossed polarizers. An axial magnetic field causes the so-called anomalous dispersion which rotates the plane of polarization of light for only a narrow frequency band near the absorptions in the gaseous medium, and this light can pass through the crossed polarizers. All other optical frequencies will be unaffected by the Faraday medium and will blocked by the crossed polarizers. [adapted from Yin et al. Opt. Lett. **16**, 1617 (1991)]

components: a right-hand circularly polarized line and a left-hand circularly polarized line. The frequency splitting between the two transitions is proportional to the applied magnetic field. Near the absorption lines, where the dispersion is appreciable, the left-hand-circularly polarized component experiences a different phase shift than the right-hand-circularly polarized component. In essence, the index of refraction for left-hand-circularly polarized light is different than for right-hand-circularly polarized light, and the medium behaves as an optical waveplate. As plane-polarized light passes through the gas, its plane of polarization is rotated. By placing the Faraday-rotating medium between two crossed polarizers, and adjusting the filter parameters (such as magnetic field strength) to rotate the plane of polarization of the selected light 90°, one can create a filter with an effective bandpass ~ 3 GHz (<0.01 nm). The out-of-band rejection of the filter is determined predominantly by the extinction ratio of the crossed polarizers, which for calcite prism polarizers can approach 10^{-6}. Out-of-band rejection ratios of 10^5 have been achieved[22] in FADOF devices.

Although the transmission bandwidth and background rejection ratio of the FADOF seem ideal for differential absorption lidar (DIAL), its practical implementation on a DIAL system is extremely difficult. Since a FADOF relies on optical absorption transitions, the transmission frequencies of the filter are not arbitrarily variable (that is, the FADOF is not widely tunable). For applications in free-space communications or backscatter lidar, the laser frequency can be tuned to coincide with a favorable transmission frequency of the FADOF - in fact, the FADOF is sometimes used inside a laser resonator to force the laser output to the correct frequency. In a DIAL system, however, the laser must be tuned to specific frequencies that coincide with optical absorptions in water vapor. Thus, in order to employ a FADOF in a DIAL system, one must find a coincidence of a molecular absorption in the filter medium and a useful absorption in water vapor. Also, the bandwidth of the FADOF filter (~ 0.01 nm) is not wide enough to pass both the on and off wavelengths required for a DIAL measurement. As a result, the FADOF must be tunable over the on-off wavelength interval of ~0.5 cm^{-1} (~0.03 nm). Finally, a DIAL measurement system must be designed to operate on any one of several water vapor absorption lines, implying that the FADOF must be capable of operating at these same frequencies.

It is extremely unlikely that the energy levels of atomic metals (like cesium or sodium) normally used in the construction of a FADOF coincide with suitable absorption transitions in water vapor. It is natural to consider using the water molecule itself as the medium in the filter. Unfortunately, water has an extremely low magnetic susceptibility, and, as result, does not exhibit the Faraday effect for reasonable magnetic field strengths and pathlengths. An alternative approach is to use the Stark effect to generate the anomalous dispersion needed for the ADOF.

In the Stark effect, a strong electric field is used to split the energy levels in the molecule. When viewed perpendicular to the electric field, the medium appears birefringent (for light near the transition frequencies). Thus, a Stark anomalous dispersion optical filter (SADOF) requires a transverse electric field applied to the

medium instead of an axial magnetic field required for the FADOF.

We studied the use of a SADOF as a narrowband filter for a water vapor DIAL system. Unfortunately, the absorption cross-section and the electric dipole moment for water vapor is quite weak. As a result, extremely long path lengths, requiring a multipass cell, are needed to generate enough polarization rotation for a filter, rendering a water-based SADOF impractical for the DIAL system.

An ADOF is not a good candidate narrowband filter for a water vapor DIAL system, primarily because the most likely media for providing the polarization rotation around the desired absorption spectra is water vapor itself. To date no other molecules with absorption spectra that are coincident with water vapor have been identified. If coincidence can be found with another molecule that has a strong magnetic or electric dipole moment, then the ADOF may be the solution for a narrowband DIAL filter, but this is not very likely. For a space-based backscatter lidar systems, where the wavelength of the laser can be tuned to match the absorption feature of a molecule which has a strong magnetic or electric dipole moment, an ADOF makes an excellent candidate narrowband filter.

The third type of filter evaluated was the Fabry-Perot etalon. It consists of two plane parallel mirrors that are usually separated by a small air gap. In some cases, the reflective coatings are deposited on opposite faces of an optical flat. The etalon uses multiple interference to produce a narrow bandwidth filter centered on a wavelength that is related to the separation between the two plates. For normal incidence on the plane-plane Fabry-Perot interferometer, the peak transmission will be centered at wavelengths that satisfy the equation:

$$m\lambda = 2nd \qquad [\mu m]$$

where m is an integer (the order of the interferometer), n is the index of refraction of the medium between the reflectors, and d is the distance between the reflectors. This equation simply states that the interferometer will pass light of wavelength λ when the optical pathlength between the reflectors is an integral number of half wavelengths. Unfortunately, the interferometer will pass light of many different wavelengths - one λ for each value of the integer m. The optical frequency spacing between adjacent orders of the interferometer is called the free spectral range (FSR) and is given by:

$$FSR = \frac{c}{2nd} \qquad [Hz]$$

where c is the speed of light. As an example, a pair of reflectors separated by 1 cm in air will yield a FSR = 15 GHz (0.5 cm^{-1} or 0.025 nm at 727 nm). An etalon constructed from fused silica with a 1 cm thickness would yield a FSR = 10 GHz (0.33 cm^{-1} or 0.017 nm at 727 nm). One practical implication of using a Fabry-Perot etalon in a DIAL

system is that additional filters would likely need to be used in series with the etalon to eliminate transmission for all but the desired order. These filters could consist of dielectric interference filters of the type discussed above (but with wider bandpass) or a series of Fabry-Perot etalons of differing FSR.

Another practical implication for the Fabry-Perot etalon in a DIAL application is the fact that the frequency of peak transmission is a function of the reflector spacing which is, in turn, a function of temperature. The peak transmission frequency, ν, for the Fabry-Perot etalon can be written as:

$$\nu = \mathrm{m}\frac{\mathrm{c}}{2n\mathrm{d}} \qquad [\mathrm{Hz}]$$

Differentiating this equation with respect to temperature, we obtain:

$$\frac{\partial \nu}{\partial T} = -\nu\left(\frac{1}{\mathrm{d}}\frac{\partial \mathrm{d}}{\partial \mathrm{T}} + \frac{1}{n}\frac{\partial n}{\partial \mathrm{T}}\right) \qquad [\mathrm{Hz\ K^{-1}}]$$

and

$$\frac{1}{\mathrm{d}}\frac{\partial \mathrm{d}}{\partial \mathrm{T}} = \alpha \qquad [\mathrm{cm\ cm^{-1}\ K^{-1}}]$$

where α is the coefficient of thermal expansion. As shown above, the change in resonant frequency is due to the sum of two effects: changes in the mirror spacing, d, due to thermal expansion, and changes in the index of refraction, n. Some glass formulations are designed to balance the two effects and produce a so-called athermal glass. In practice, however, the athermal glass has $\partial \nu/\partial T = 0$ for only one temperature or narrow temperature range. Thus, a Fabry-Perot etalon in a DIAL system would need very precise temperature control, or else the filter would drift in and out of resonance with the DIAL wavelength. If multiple Fabry-Perot etalons are used in series, they must all be independently temperature controlled since they must all be tuned to pass the same wavelength.

Another important parameter for a Fabry-Perot etalon is its finesse, F, which is defined as the ratio of the free spectral range to the resolution (or bandwidth) of the etalon. The finesse of the etalon is determined by the reflectivity of the coatings, the flatness of the mirror substrates, and other optical imperfections which are potential loss mechanisms. The most optimistic value of the finesse is that determined by the reflectivity of the mirror coatings and is given by:

$$F = \pi\frac{\sqrt{\mathrm{r}}}{(1-\mathrm{r})}$$

where r is the power reflectivity of the coatings (assumed to be equal for both reflectors). To produce a finesse of 100, for example, mirror reflectivities of $r \geq 97\%$ are required. Fortunately, laser gyroscope applications have driven significant improvements in both optical polishing technology and mirror coating technology, and high-finesse interferometers can be constructed. For example, Newport Corporation now sells an interferometer with a finesse in excess of 15,000.

As an example for our DIAL application, suppose that we want to build a Fabry-Perot filter with a bandpass of 1.0 cm^{-1} (0.05 nm at 727 nm) so that it will pass both the on and the off wavelength without tuning. If we can build the filter with a finesse of 100, we can design it with a free spectral range of 100 cm^{-1} (5 nm at 727 nm). This would require a 50-μm-thick air-spaced etalon or a 30-μm-thick fused silica etalon. The location of the peak transmission would have to be set by either temperature tuning the etalon (in the case of a solid etalon) or by changing the mirror spacing using a piezoelectric actuator. The etalon, once fabricated, could be calibrated to find its temperature vs. frequency characteristic, or it could be servo locked to the desired wavelength.

The Fabry-Perot etalon can provide bandwidths comparable to that of the ADOF, but with much higher optical throughputs. The peak transmission of a well-constructed Fabry-Perot (by itself) can approach unity. However, any additional blocking filters that may be required to suppress transmission of adjacent interferometer modes will introduce additional loss. Also, the Fabry-Perot will require a well-collimated beam in order to achieve its performance benefits. Despite the complexity of setting and maintaining the required passband frequency, the Fabry-Perot etalon appears to be the best candidate narrowband filter for a satellite-based DIAL system.

Receiver Mirror Material

Aircraft and satellite platforms both limit the weight of the payload. In order to keep launch costs as low as possible, we must minimize the weight of the DIAL system. The single largest contributor to the weight in a DIAL system is often the collecting mirror which must be kept large in order to collect the weak DIAL return signal. Due to its excellent structural properties and low density, beryllium is usually the material of choice when constructing lightweight optical components. Siliconized silicon carbide (SiC), however does offer some attractive features - its low thermal expansion coupled with its thermal conductivity make for a thermal stability four times that of beryllium. This yields a more stable optical component under dynamic thermal conditions. Although SiC's specific stiffness is only 70% of beryllium's, the attainable shapes with SiC can yield higher sectional stiffness, thereby producing a stiffer mirror for a given weight. Additionally, safety complications encountered in the fabrication of beryllium, such as the precautions that must be taken to avoid berylliosis, tend to make beryllium components much more expensive than SiC. For the reasons stated above we chose SiC

for the mirror material in the receiver. Due to its lightweight the size of the mirror will be limited by volume constraints and not weight constraints.

Atmospheric Modeling

An important aspect of this LDRD project is predicting the performance of the DIAL system for a wide variety of input conditions and hardware configurations. Many of the parameters for the hardware (such as detector quantum efficiency, amplifier noise, optical efficiency) can be reliably gathered from manufacturer's data sheets or from laboratory measurements. However, the properties of the atmosphere (such as temperature, pressure, water vapor density) are much less precisely defined and are inherently variable. The following section describes some of the assumptions and data that we have used to model the atmosphere for our simulations and modeling.

Water vapor is probably the most variable gaseous constituent of the earth's atmosphere. This, combined with the fact that water vapor is the most important driver of the earth's heat balance, is our motivation for developing a lidar to accurately measure water vapor profiles. In order to simulate the performance of DIAL systems, we use data that is representative of average conditions for various seasons and various geographical locations. The atmospheric data sets we have used for this project are derived from the work of McClatchey et al.[23] and have been published in a variety of reference sources including The Infrared Handbook[24]. These data sets, which are often called *AFGL standard atmospheres*, describe the pressure, temperature, air density, and water vapor density as a function of altitude for five different seasonal/geographical conditions: tropical, midlatitude summer, subarctic winter, subarctic summer, and midlatitude winter. Appendix D contains more information concerning the AFGL standard atmospheres and plots of the data as a function of altitude.

Light Scattering Models

The operation of any single-ended lidar system depends on molecules and particulates in the atmosphere to scatter light backward into the receiver optical system. The strength of this backscattered return signal is heavily dependent on the number density, size, and composition of the backscattering medium. In the following section, we discuss the most important light scattering mechanisms pertinent to our DIAL system. In particular, we describe the assumptions and models that we used to calculate the predicted signal strength for our system.

Light scattered from particles with dimensions much smaller than the wavelength of light is termed Rayleigh scattering. In pure air, the dominant scattering mechanism is Rayleigh scattering. For the mixture of gases in the atmosphere below 100 km, the backscatter cross section for Rayleigh scattering can be calculated from[1]:

$$\sigma(\lambda) = 5.45\left[\frac{550\,\text{nm}}{\lambda}\right]^4 \text{ x } 10^{-32} \qquad [\text{m}^2\,\text{sr}^{-1}]$$

where λ is the wavelength of light in units of nm. The volumetric backscatter coefficient due to Rayleigh scattering is given by:

$$\beta_{Rayleigh}(\lambda, R) = N(R)\sigma(\lambda) \qquad [\text{m}^{-1}\,\text{sr}^{-1}]$$

where N(R) is the number density of air molecules at the altitude R. Note the $1/\lambda^4$ dependence of the backscatter coefficient. Rayleigh scattering sets a lower limit on the amount of light backscattered into a lidar receiver.

Light scattered from particulates and aerosols in the atmosphere with dimensions comparable to or greater than the wavelength of light is termed aerosol scattering. Dust, ice crystals, fog, haze, and clouds all contribute to aerosol scattering, and the detailed scattering properties depend on the size, shape and index of refraction of the particles. The overall backscatter coefficient β depends on the distribution of the particles and the size of the particles. Unlike the $1/\lambda^4$ dependence of Rayleigh scattering cross sections, aerosol scattering cross sections typically vary as $1/\lambda^2$.

Since the type of scattering particles and number density of scattering particles is highly variable from location to location and from time to time, the aerosol scattering component of the backscatter coefficient is very difficult to model. For example, volcano eruptions produce dust and ash clouds that can greatly increase the backscatter coefficient (in some locations) for months. However, we estimated the volumetric backscatter coefficient due to aerosol scattering using a formula provided in a paper by Kavaya et. al[19]. The formula is given by:

$$\beta_{Aerosol}(\lambda, R) = 10^{[3.521\exp\left(\frac{-R}{4967}\right)-9.455]}\left(\frac{2100}{\lambda}\right)^2 \qquad [\text{m}^{-1}\,\text{sr}^{-1}]$$

where λ is the wavelength of light in units of nm. The total volumetric backscatter coefficient is then given by:

$$\beta(\lambda, R) = \beta_{Rayleigh}(\lambda, R) + \beta_{Aerosol}(\lambda, R) \qquad [\text{m}^{-1}\,\text{sr}^{-1}]$$

Figure 2 shows the relative contributions of Rayleigh and aerosol scattering on the backscatter coefficient at 727 nm wavelength as a function of altitude. Note that at low altitudes (say, from sea level to ~3 km) aerosol scattering is the dominant scattering mechanism contributing to the backscatter coefficient, β. This is basically a result of dust, dirt, ice crystals and other aerosols that tend to lie low in the atmosphere. Above 4 to 5 km in altitude, the air is much cleaner (less dust and aerosols), and the dominant scattering mechanism is Rayleigh scattering. Thus, at high altitudes, the backscatter

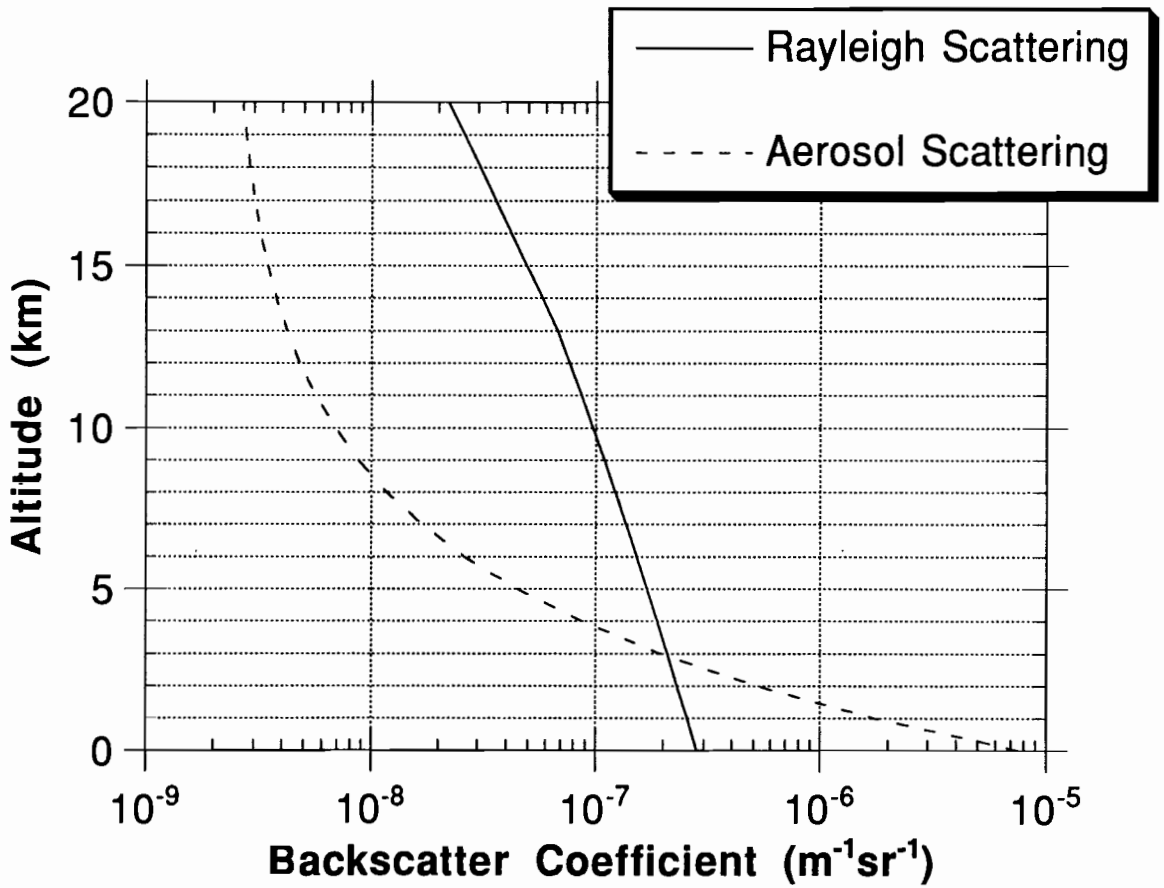

Figure 2. Relative Contributions of Molecular (Rayleigh) and Aerosol Scattering to the Volumetric Backscattering Coefficient at 727 nm Wavelength.

coefficient can be estimated as simply the Rayleigh scattering component.

Choosing a DIAL Wavelength

The selection of wavelengths for the DIAL measurement is a very important part of optimizing the instrument design. In most cases of interest, a variety of DIAL lines are required to allow optimum operation of the lidar as atmospheric conditions change. For example, if conditions in the measurement volume are relatively dry, a strongly absorbing line is required to produce an adequate differential signal. On the other hand, if conditions are relatively humid, a weakly absorbing line is needed so that the transmitted beam and return signal are not completely attenuated.

A number of good references are available that describe the requirements for absorption lines used in a DIAL system. Some of the most important requirements are summarized below:

- The line should be relatively isolated from other water vapor lines and from other atmospheric species such as CO_2.

- Since the temperature of the atmosphere varies with altitude, the line strength of the chosen transition should be relatively temperature insensitive for the temperatures at the altitude(s) of interest. The line strength as a function of temperature is given by[3]:

$$S(T) = S_0\left(\frac{T_0}{T}\right)^{1.5} \exp\left[\frac{E''hc}{k}\left(\frac{1}{T_0}-\frac{1}{T}\right)\right] \qquad [\text{cm molecule}^{-1}]$$

  where S_0 is the linestrength measured at T_0 = 296 K, T is the temperature, E" is the ground-state rotational energy level, h is Planck's constant, c is the speed of light, and k is Boltzmann's constant.

- To find the ground-state energy, E", at which the transition is optimally temperature insensitive, take the derivative of the integrated absorption with respect to temperature[25,26].

- A number of suitable DIAL transitions must be identified, so that the transition with the optimum linestrength for the actual water vapor concentration encountered during the measurements can be used.

Atmospheric Transmission

There are a number of factors that determine the atmospheric transmission at a particular wavelength. This includes molecular absorption and scattering from such molecules as water vapor, CO_2, O_3, N_2O, CO, CH_4, O_2, and aerosol absorption and scattering. The general formula for atmospheric transmission is given by:

$$\tau_{atm}(\lambda, R) = \exp\left\{ - \int_{R_{DIAL}}^{R} \kappa(\lambda, R) dr \right\}$$

where $\kappa(\lambda,R)$ is the atmospheric attenuation coefficient. Since there are a large number of factors needed to accurately determine the atmospheric transmission, we decided to use one of the commercial atmospheric transmission models. Also in the case of DIAL where we are trying to determine the atmospheric transmission for the on and the off wavelengths, which are very close in wavelength yet very different in transmission through the atmosphere due to molecular absorption, we need to use a model that has very high spectral resolution. FASCODE[27] is an atmospheric transmission code that was developed by the Air Force Geophysics Lab. It uses the HITRAN[28] data base, which has very high spectral resolution, and can accurately determine the difference in atmospheric transmission between the on and off DIAL wavelengths.

We assumed the Mid-Latitude Summer model for molecular absorption and scattering. For aerosol absorption and scattering, we assumed a rural 23 km visibility aerosol model for the airborne and space-based concepts, and a rural 60 km visibility aerosol model for the ground-based demonstration system.

Performance Modeling

The initial performance requirements of the water vapor DIAL were the ability to profile water vapor in the atmosphere from 2 to 18 km with 20% accuracy from an airborne and spaceborne platform with a maximum vertical resolution of 1 km and a maximum horizontal resolution of 100 km. Two additional requirements that will affect the performance of the system are that the on-line and the off-line DIAL signals must be detected and measured to an accuracy of 10%, and the DIAL system must be eye safe for direct viewing with binoculars in the daytime and direct viewing with an 8-inch telescope at night. The accuracy of the water vapor concentration measurement is determined by the DIAL measurement error which results from the differentiation between the on-line and the off-line DIAL signals. The signal-to-noise ratio (SNR) determines the accuracy with which one can measure the individual DIAL signals. Using Gaussian statistics, a SNR $\geq$ 17.5 will provide 90% confidence that one can measure the received signal to 10% accuracy. These three requirements are used to measure the performance of the DIAL system.

Because of the complex interrelationship between laser wavelengths, water vapor lines, detectors, etc., a computer model was developed to calculate the SNR of the on-line and off-line DIAL signals and the DIAL measurement error for various operating parameters such as laser wavelength, laser energy, telescope diameter, operating range, and other operational parameters. The model includes the volumetric backscatter coefficient obtained from aerosol models and Rayleigh scattering, and the two-way atmospheric transmission of the on-line and off-line DIAL signals obtained from

standard profiles of water vapor concentration as a function of altitude, and HITRAN data bases as discussed in the previous section. The model also calculates the energy density of the laser at the earth's surface and compares that density with the maximum permissible exposure (MPE) level for direct viewing of the laser beam with 2-inch binoculars for the daytime and an 8-inch telescope at night using the standards set by the American National Standards Institute standard for the safe use of lasers.

The lidar return signal as a function of altitude for a downward-looking DIAL system is given by:

$$S(\lambda, R) = \frac{E\,\eta(\lambda) G A_0\,\tau_0(\lambda)\beta(\lambda, R)\Delta R(\tau_{atm}(\lambda, R))^2}{h\,\nu(R_{DIAL} - R)^2} \qquad \text{[photoelectrons]}$$

where E is the laser pulse energy, $\eta(\lambda)$ is the quantum efficiency of the detector at the wavelength λ, G is the gain of the detector, A_o is the area of the receiver telescope, $\tau_o(\lambda)$ is the transmission of the collecting optics at the wavelength λ, $\beta(\lambda, R)$ is the volumetric backscatter coefficient, ΔR is the vertical resolution of the DIAL system, $\tau_{atm}(\lambda,R)$ is the atmospheric transmission, R_{DIAL} is the altitude of the DIAL system, and R is the altitude being measured. The return signal is directly proportional to the laser energy and the area of the collecting optics, and it is inversely proportional to the distance between the DIAL system and the altitude being measured ($(R_{DIAL}-R)$ is commonly called the range). These three parameters play off against one another and must be adjusted to find the optimal DIAL system. The return signal is also directly proportional to the volumetric backscatter coefficient and the two-way atmospheric transmission. Therefore, it is very important to choose the best water vapor line to maximize the return laser signal for detection and provide enough differentiation between the on-line and off-line signals to provide an accurate water vapor measurement.

There are four sources of noise present in the DIAL system. They are photon noise in the received laser signal, photon noise due to the background radiation, detector noise, and amplifier noise. Photon noise, which obeys Poisson statistics, is due to the uncertainty in the arrival rate of the photons on the detector system. The signal-to-noise ratio of the detector is limited by the shot-noise generated by the dark current.

The signal due to the solar background radiation is given by:

$$B(\lambda) = \frac{L_\lambda \eta(\lambda) G A_0 \tau_0(\lambda)\Delta\lambda\,\pi\,FOV^2\,\rho_e\,\Delta R}{2\,h\,\nu c} \qquad \text{[photoelectrons]}$$

where L_λ is the solar spectral radiance at wavelength λ at the top of the atmosphere, $\Delta\lambda$ is the bandwidth of the background rejection filter, FOV is the field of view of the collecting optics, and ρ_e is the earth's albedo. The background signal is strongly

dependent on the diameter of the collecting optics and the field-of-view of the optics. The field-of-view will be set as small as possible to minimize the solar background, but it must be large enough that it overlaps the laser spot on the ground. The background is also directly proportional to the wavelength bandwidth of the background rejection filter. This bandwidth must be made as small as possible in order to minimize the effects of solar background on the DIAL system. At night the background is assumed to be $1x10^{-5}$ times that of the solar background.

The signal due to detector noise power is given by:

$$D(\lambda) = \left(\frac{NEP(\lambda)\,\eta(\lambda)\,G}{h\,\nu} \right)^2 \frac{\Delta R}{c} \qquad \text{[photoelectrons]}$$

where NEP(λ) is the noise equivalent power of the detector. It is important to find a detector with low dark current to keep the NEP of the detector as small as possible.

The signal due to amplifier noise power is given by:

$$A = I_{na}^2\, B_{amp} \left(\frac{2\Delta R}{c\,q} \right)^2 \qquad \text{[photoelectrons]}$$

where I_{na} is the amplifier noise current and B_{amp} is the amplifier bandwidth given by:

$$B_{amp} = \frac{c}{1.25\,\Delta R} \qquad \text{[Hz]}$$

This bandwidth is based upon using a reset integrator configuration in which 25% of the integration time is devoted to the reset process. The bandwidth of the amplifier must be slightly larger than the bandwidth of the return signal in order to preserve the integrity of the return signal. (The bandwidth of the return signal is inversely proportional to the range resolution ΔR.)

In order to improve the SNR, one can average many individual measurements. Because the noise is random and uncorrelated, the SNR will be improved by the square root of the number of shots. The SNR is then given by:

$$SNR(\lambda, R) = \frac{S(\lambda, R)\,N^{1/2}}{\left[(S(\lambda, R) + B(\lambda))\,G\,F + D(\lambda) + A \right]^{1/2}}$$

where F is the excess noise factor of the detector and N is the number of measurements averaged. In order to determine the strength of the backscattered return signal to an accuracy of 10% with a 90% confidence in the measurement, at a given altitude the SNR

must be ≥17.5, according to Gaussian statistics, for the on-line and the off-line DIAL signals. The SNR often sets the lower limit on the altitudes that one can profile with an airborne or spaceborne DIAL system.

The water vapor concentration is given by:

$$n = \frac{1}{2\Delta\sigma\Delta R}\ln\left(\frac{S(\lambda_{on},R_1)\,S(\lambda_{off},R_2)}{S(\lambda_{on},R_2)\,S(\lambda_{off},R_1)}\right) \qquad [\text{molecules m}^{-3}]$$

where $\Delta\sigma$ is the differential absorption cross section of the water vapor line used to make the measurement and $\Delta R = R_2 - R_1$.

The DIAL measurement error is given by:

$$\frac{1}{2n\Delta\sigma\Delta R}\left[\sum_{i=1}^{2}\sum_{j=on}^{j=off}\frac{(S(\lambda_j,R_i)+B)GF+D+A}{S^2(\lambda_j,R_i)}\right]^{1/2} N^{1/2}$$

In order to profile a given altitude, the measurement error must be ≤ 20% (this is the largest error we have chosen to be acceptable). This error in the water vapor concentration sets the upper limit on the altitudes that one can profile with an airborne or spaceborne DIAL system, and in a spaceborne system it sometimes sets the lower limit as well. The DIAL measurement error is strongly dependent on the altitude and the water vapor line chosen. Often a very strong line is required at higher altitudes, where the amount of water vapor in the atmosphere is very low. However, at lower altitudes the atmospheric attenuation will be too great to detect the DIAL return signals with a strong water vapor line, and therefore, a weaker line is required. For this reason, it is very important that the laser and the filter have the capability to function at several water vapor lines.

The third requirement that affects the performance of the DIAL system is that of eye safety. The amount of laser exposure that a viewer on earth will receive is a function of the laser energy, the laser divergence, the laser repetition rate, the laser wavelength, DIAL platform ground velocity, and the distance from the laser to the viewer. The laser energy, divergence and repetition rate must be adjusted so that the DIAL system is eye safe for direct viewing with binoculars in the daytime and direct viewing with an 8-inch telescope at night. The eye safety requirement will ultimately result in decreased system performance due to the restrictions it places on the system parameters as shown in Figure 3.

The energy density of the laser on the earth's surface is given by:

$$LED = \frac{4E}{\pi(R_{DIAL}\,\theta_{FWHM})^2} \qquad [\text{J m}^{-2}]$$

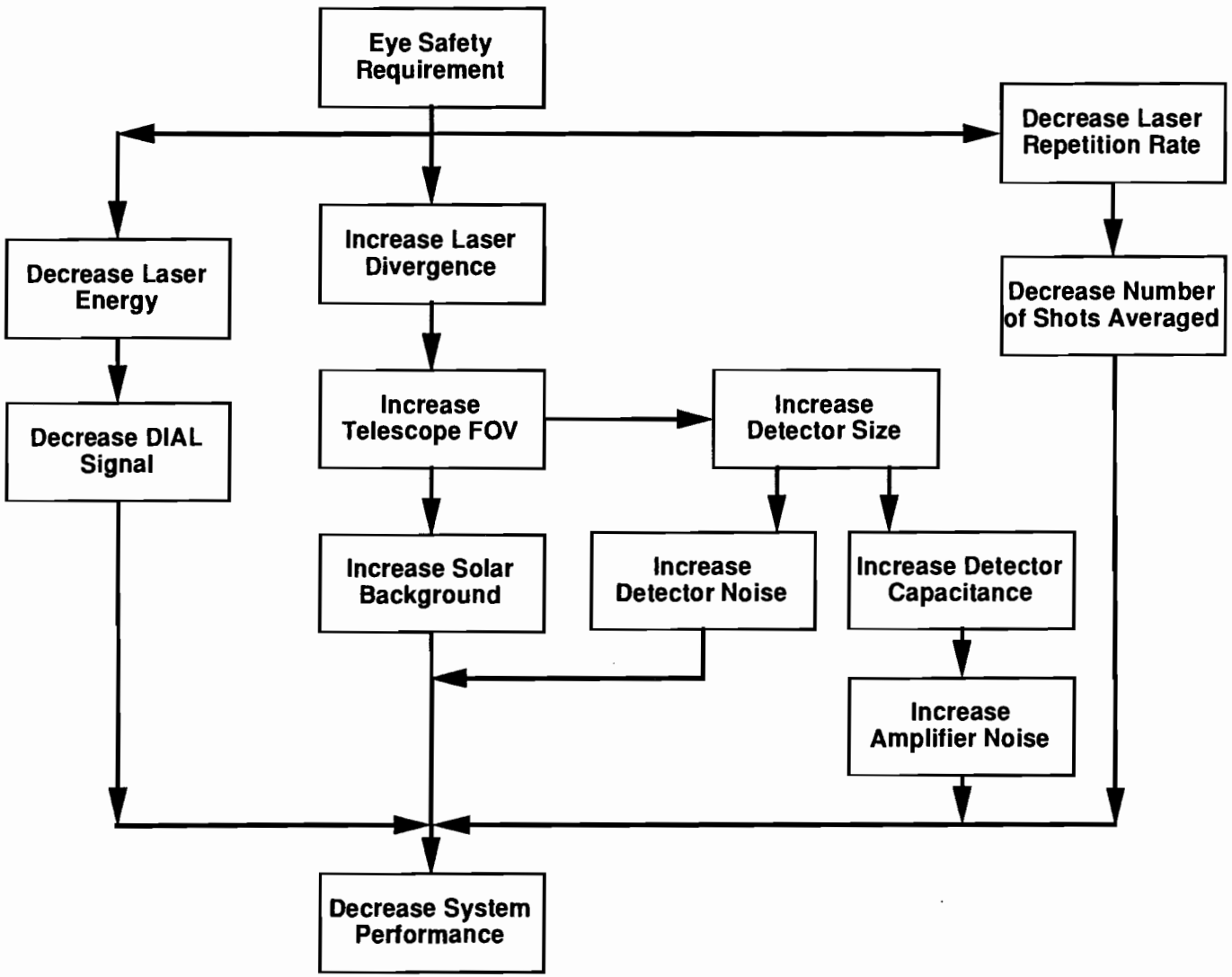

Figure 3. Effects of Eye Safety Requirements on System Parameters.

where LED stands for the laser energy density and θ_{FWHM} is the laser beam divergence measured at full width half maximum. This value was then compared with the MPE levels obtained from the ANSI standard for the safe use of lasers for the given wavelength and operating conditions. The MPE values for the four DIAL wavelength regions are listed in Table 1. The exposure times used in calculating the MPE values were determined by knowing the size of the laser beam on the ground and the ground velocity of the DIAL platform. The laser energy, laser beam divergence, or the laser repetition rate was adjusted so that LED was less than the MPE for direct viewing with a 2-inch binoculars in the daytime and an 8-inch telescope at night. The MPE values differ for a Ti:sapphire laser system and a Cr:LiSAF laser system because the Cr:LiSAF laser system has a higher conversion efficiency and therefore a larger energy output. The divergence of the Cr:LiSAF laser must be made larger to make it eye safe and therefore, the exposure time is increased thus increasing the MPE value. When the divergence of the laser is increased significantly the LED and the MPE values must be iterated to ensure that the LED is below the MPE value. For small changes in the laser divergence, the exposure time, and therefore the MPE values, are essentially unchanged.

Water vapor DIAL performance estimates generated by our computer model were compared against the performance estimates listed in the report by Browell et al.[29]. Inputting the parameters from the LASA DIAL system, we were able to reproduce the performance estimates listed in the paper. From this test we verified that our computer model accurately predicts the performance of a water vapor DIAL system (or is at least consistent with the model developed by Browell et al.).

Results of Trade Studies and Performance Modeling

A computer-based lidar performance model was developed to perform trade studies on various technologies and system configurations to develop lidar concepts that are lightweight, low power, rugged and autonomous. As a result of the performance modeling we were able to select appropriate water vapor lines and produce conceptual designs for airborne and space-based water vapor DIAL systems. One interesting result of the performance modeling was the relationship found between aperture size and laser power consumed, and the ability to profile water vapor at high altitudes.

Water Vapor Line Selection

Four water vapor absorption regions were chosen based on the laser trade studies, atmospheric modeling, and existence of suitable absorption transitions for DIAL. The spectral regions chosen for study are near 2.1 μm, 727 nm, 817 nm, and 940 nm. Additional trade studies were done for detectors and filters at these wavelengths. The performance of water vapor DIAL systems in these wavelength regions were then compared using the performance model and the results from the trade studies and the

Table 1: ANSI MPE Values for the Water Vapor DIAL Wavelengths

Platform	Wavelength (nm)	Binoculars MPE (J/m^2)	Direct Viewing 8-inch Telescope MPE (J/m^2)
Aircraft[1]	727	5.7×10^{-5}	2.6×10^{-6}
	817	8.7×10^{-5}	3.9×10^{-6}
	940[2]	1.7×10^{-4}	7.6×10^{-6}
	940[3]	1.3×10^{-4}	5.4×10^{-6}
	2100[4]	1.9	0.119
Satellite[5]	727	1.07×10^{-4}	6.66×10^{-6}
	817	1.67×10^{-4}	1.02×10^{-5}
	940	2.89×10^{-4}	1.80×10^{-5}
	2100	1.9	0.119

1 Includes multiple pulse exposure to a 80-Hz laser.
2. For a Ti:sapphire laser.
3. For a Cr:LiSAF laser.
4. Divergence of laser can be made small enough so that a viewer is only exposed to a single pulse as the aircraft passes over.
5. Only single pulse exposure occurs as satellite passes over.

atmospheric modeling. For the aircraft-based DIAL system, we initially assumed an aircraft altitude of 20 km, a 30-cm receiver aperture, a 10-km horizontal resolution, and a 500-m vertical resolution. For the satellite-based DIAL system, we assumed a satellite altitude of 500 km, a 1-meter receiver aperture, a 100-km horizontal resolution, and a 1-km vertical resolution. The results took into account all of the performance and system requirements stated earlier.

In the 2.1-μm region, the initial results from the performance modeling showed that we could profile water vapor in the atmosphere for a small range of altitudes from an aircraft platform, but not from a satellite-based platform within the constraints set on the DIAL system. This is because the strength of the water vapor absorption lines near 2.1 μm are low, creating a high DIAL measurement error at medium to high altitudes where the water vapor concentration is small. In addition, the noise levels of the detectors are high, making it difficult, if not impossible, to detect the DIAL signals from an aircraft or satellite-based platform.

In the 727-nm region, the initial results from the performance modeling showed that we could profile water vapor in the atmosphere over a large range of altitudes from an aircraft platform with a Ti:sapphire laser and an interference filter. From a satellite

platform we could profile water vapor at low and medium altitudes, but not at high altitudes using a Ti:sapphire laser and a Fabry-Perot Etalon filter. The Fabry-Perot etalon filter is necessary in the case of a satellite-based DIAL because the return signals are so small the noise from the solar background will make detection difficult.

In the 817-nm region, the initial results were similar to the 727-nm region. From an aircraft platform, we could profile water vapor in the atmosphere over a large range of altitudes using a Ti:sapphire laser and an interference filter. From a satellite platform, we could profile water vapor at low altitudes only using a Ti:sapphire laser and a Fabry-Perot etalon filter. The performance of the 817-nm region is slightly better than the 727-nm case for the aircraft platform, and slightly worse than the 727-nm case for the satellite platform. This is because the 817-nm region has some stronger absorption lines in it to allow higher altitude profiling from the aircraft platform. However, from a satellite platform the stronger lines are too strong. The line strengths used in the 727-nm region and the 817-nm region for the satellite platform are similar. However, since the volumetric backscatter coefficient is larger for the 727-nm region we get slightly better results.

In the 940-nm region, the initial results from the performance modeling showed that we could also profile water vapor in the atmosphere over a fairly large range of altitudes using a Ti:sapphire laser and an interference filter from an aircraft platform. Slightly better results could be obtained with the use of a Cr:LiSAF laser and an interference filter. However, the performance in the 817-nm region was still slightly better. From a satellite platform, our initial results showed we could profile water vapor in the atmosphere at low and medium altitudes, but not high altitudes using a Cr:LiSAF laser and a Fabry-Perot etalon filter.

From these performance results we concluded that the 2.1-μm region is not the best wavelength region for an aircraft-based or space-based water vapor DIAL. The 727-nm, 817-nm, and the 940-nm regions all look promising for an aircraft-based water vapor DIAL. However, we can profile slightly higher altitudes in the 817-nm region at the expense of very low altitude profiling. The satellite platform can only profile a small range of altitudes in the lower and middle atmosphere. The performance in the 727-nm region and the 940-nm region for a satellite platform were comparable. However, there is a higher degree of uncertainty in the ability of the Cr:LiSAF laser to operate at 940 nm than there is that the Ti:sapphire laser can operate at 727 nm. Therefore, the decision was made to choose the 817-nm region for an aircraft-based water vapor DIAL system concept, and the 727-nm region for a space-based water vapor DIAL system concept.

Maximum Height Profiled for an Airborne Water Vapor DIAL as a function of Laser Power and Receiver Mirror Diameter

We realized, as a result of the performance modeling, that we could not meet the performance requirement to profile water vapor in the atmosphere up to 18 km with a

20% DIAL measurement error, a SNR of 17.5, and a 100-kg, 100-W DIAL system in any of the wavelength regions. So we decided to vary the receiver mirror diameter and laser power to determine the maximum height one could profile using an airborne water vapor DIAL. We assumed that the DIAL system will be at an aircraft altitude of 20 km, will use a Ti:sapphire laser with a 1.5% electrical-to-optical conversion efficiency, and will use narrowband multilayer interference filters.

Figure 4 shows a plot of the maximum height profiled for 10% and 20% DIAL error at 727 nm and 942 nm as a function of receiver mirror diameter using a laser which consumes 200 W of electrical power. We found that as the maximum height profiled goes up linearly the receiver mirror diameter goes up exponentially. Even for a very large 1-meter receiving mirror diameter, one could only profile water vapor up to about 12.5 km.

Figure 5 shows a plot of the maximum height profiled for 10% and 20% DIAL error at 727 nm and 942 nm as a function of laser power using a 30-cm-diameter receiving mirror. We found again that as the maximum height profiled goes up linearly the laser power goes up exponentially. Even for a laser which consumes 1600 W of electrical power, one could only profile water vapor up to about 12.4 km.

Although we did not perform this exercise for the 817-nm region, the fundamental relationship between the maximum height profiled and the power consumed is expected to parallel the previous examples. The relationship between profiling capability and laser power and telescope aperture is a function of the physics of the atmosphere not a function of the wavelength region chosen. Therefore, we decided to lower the aircraft altitude to increase the signal and profile water vapor in the atmosphere at altitudes in which the system mission and performance requirements could be met.

Aircraft-Based Conceptual Design

A conceptual design for an airborne water vapor DIAL was formulated based on a 100-W 100-kg system that would fit in a Perseus Unmanned Aerospace Vehicle (UAV) pod. A UAV can fly at altitudes of 15 km or greater for 24 to 48-hour periods of time, allowing relatively large area coverage. The base system was designed around a Ti:sapphire laser with 2% wall plug efficiency in the 817-nm region, a silicon APD cooled to -20° C, and a narrow bandwidth interference filter for background rejection. The interference filter would be temperature controlled using a heater to ensure that the bandpass was centered on the DIAL wavelengths of interest. Table 2 lists the aircraft-based water vapor DIAL system parameters.

Table 3 lists the estimated performance of the aircraft-based water vapor DIAL design. We found that lowering the aircraft altitude to 15 km allowed us to profile water vapor much higher in the atmosphere. We can profile from 1 to 11 km with a

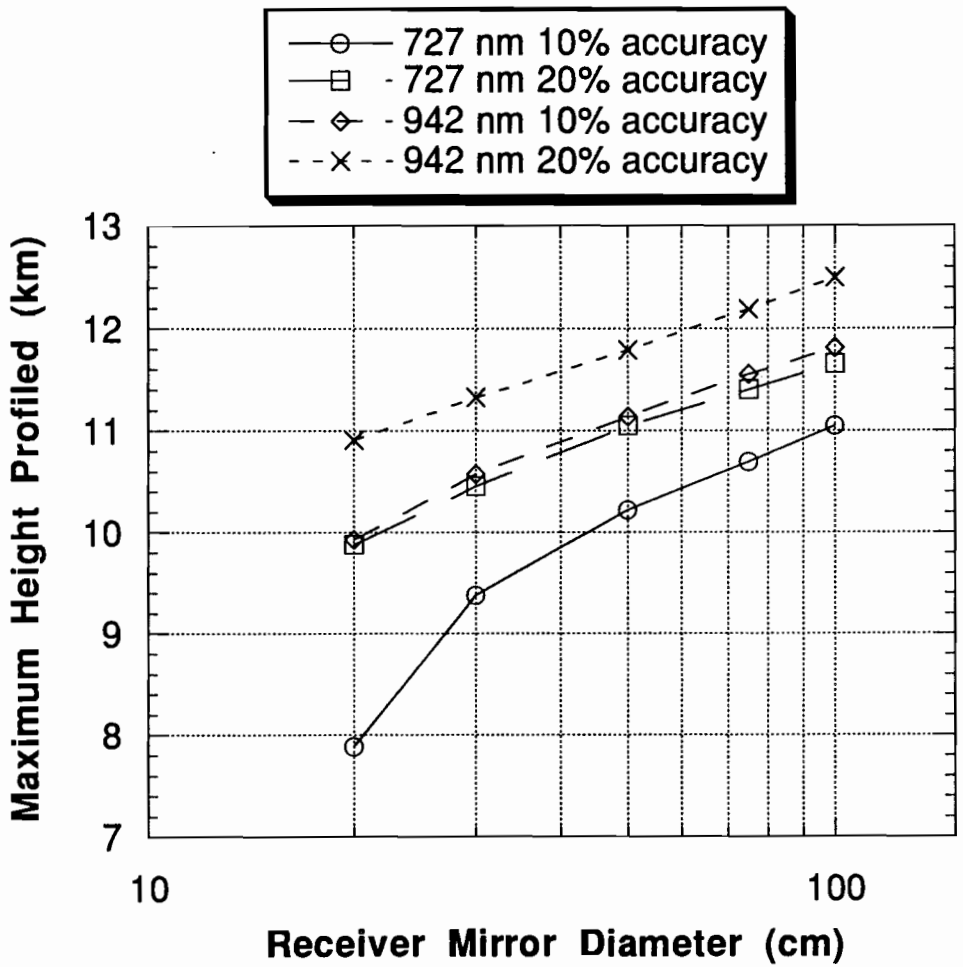

Figure 4. Maximum Height Profiled versus Receiver Mirror Diameter for 10% and 20% DIAL Measurement Accuracies. Assumes a 20 km airplane altitude, 37.5 mJ, 40 Hz, 1.5% conversion efficiency Ti:sapphire laser, 10 km horizontal resolution, 500 m vertical resolution, and a mid-latitude summer daytime earth background (albedo 30%).

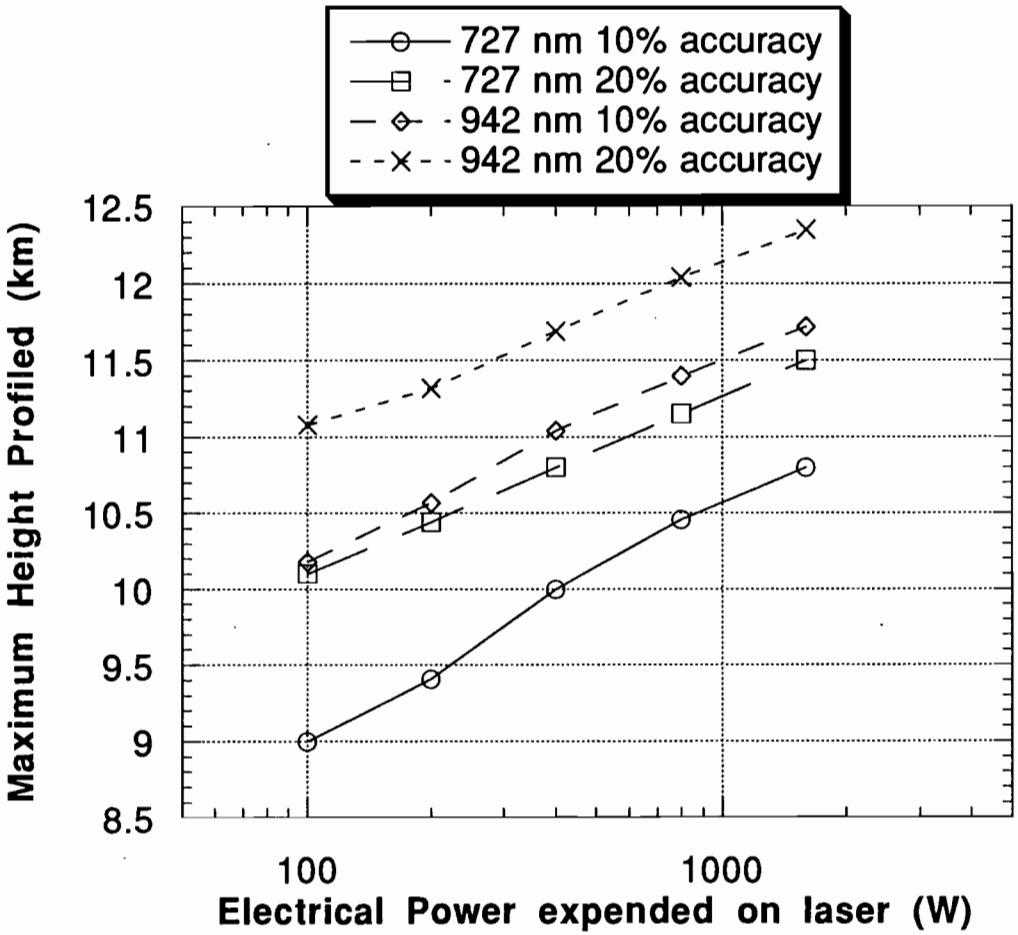

Figure 5. Maximum Height Profiled versus Laser Power Expended for 10% and 20% DIAL Measurement Accuracies. Assumes a 20 km airplane altitude, 30 cm receiver aperture, 1.5% conversion efficiency Ti:sapphire laser, 10 km horizontal resolution, 500 m vertical resolution, and a mid-latitude summer daytime earth background (albedo 30%).

Table 2: Aircraft-Based Water Vapor DIAL System Parameters

Parameters	Value	
Transmitter:		
Ti:sapphire Laser		
Laser Wavelength	~ 817 nm	
Laser Energy	25 mJ per pulse	
Laser Wall Plug Efficiency	2%	
Laser Divergence (FWHM)	1.3 mrad (Day)	6.05 mrad (Night)
DIAL Measurements Per Second	40	
Receiver:		
Diameter of Collecting Optics	30 cm	
Full Field of View	1.35 mrad (Day)	6.1 mrad (Night)
Filter Bandwidth (FWHM)	1.0 nm	
Optical Transmittance (Total)	29.3%	
Detector Si APD at -20 °C (C30956E)		
Quantum Efficiency	85%	
Gain	75	
Noise Equivalent Power	6.55×10^{-15} W/Hz$^{1/2}$	
Excess Noise Factor	3.475	
Amplifier Noise Current	1×10^{-13} A/Hz$^{1/2}$	
Other:		
Solar Spectral Radiance	250 W/(m^2 μm sr)	
Nighttime Background Radiance	.0025 W/(m^2 μm sr)	
Earth Albedo	30%	
Aircraft Altitude	15 km	
Relative Ground Velocity	100 m/s	
Vertical Resolution	500 m	
Horizontal Resolution	10 km	

Table 3: Estimated Performance for an Aircraft-Based Water Vapor DIAL Conceptual Design; Mid-latitude Summer Model; Albedo = 0.3

Wavelength	Peak Absorption Cross section	Background	Range Profiled DIAL Error ≤ 10%	Range Profiled DIAL Error ≤ 20%
816.9384 nm	2.58E-27 m^2	Day/Earth	1 - 7.5 km	1 - 9.5 km
816.9989 nm	1.33E-26 m^2	Day/Earth	4.5 - 11 km	4.5 - 12 km
816.9384 nm	2.58E-27 m^2	Night/Earth	0 - 10.5 km	0 - 11 km
816.9989 nm	1.33E-26 m^2	Night/Earth	3 - 12 km	3 - 14 km

DIAL measurement error of ≤ 10% and from 1 to 12 km with a DIAL measurement error of ≤ 20% with a daytime earth background using two water vapor lines in the 817-nm region. Just using a single on-line we can profile water vapor over a fairly large range of altitudes (~8.5 km). At night, we could profile water vapor from 0 to 12 km with a DIAL measurement error of ≤ 10% and from 0 to 14 km with a DIAL measurement error of ≤ 20% also using two water vapor lines in the 817-nm region. Again just using a single on-line we can profile water vapor at night over a large range of altitudes (~ 11 km). These results are based on a Mid-latitude Summer model for molecular scattering and absorption and a rural 23-km visibility aerosol model.

The optical layout for the Ti:sapphire laser system is shown in Figure 6. The laser system can be made small enough to fit easily into the Perseus pod and has a high enough efficiency to meet the power requirements for the DIAL system. Figure 7 shows a diagram of the receiver optical system. The mirrors are made of SiC and are extremely lightweight. The receiver background rejection filter system is shown in Figure 8. The lenses are necessary to collimate the light as it passes through the filter and then focus it on the detector. Table 4 shows a breakdown of the estimated power, weight, and volume for the various components of the UAV water vapor DIAL system. Figure 9 shows how the water vapor DIAL system might fit in a Perseus pod. The UAV lidar electronics conceptual block diagram is shown in Figure 10. These are the building blocks for a UAV water vapor DIAL system.

We feel that this UAV water vapor DIAL system could be built with technologies that are available today. It could weigh less than 50 kg and consume around 135 W of power. It can easily fit inside the pod of a UAV, and will provide much needed water vapor profiling measurements over a large range of altitudes.

Space-Based Conceptual Design

As a result of our performance modeling, it soon became evident that a space-based water vapor DIAL system would have very limited profiling capabilities within the system constraints of a 100-W 100-kg system, and the performance constraints of DIAL measurement error of ≤ 20% and a SNR ≥ 17.5. Therefore, we decided to relax those requirements somewhat for a space-based conceptual design to be able to profile a large enough range of altitudes to be of use to the scientific community. We allowed the system to use 200 watts of electric power for the laser system, and we relaxed the SNR requirement to be ≥ 10, and the DIAL measurement error requirement to ≤ 23%. The base system was designed around using a Ti:sapphire laser with 2% electrical-to-optical conversion efficiency in the 727-nm region, a silicon APD cooled to -40° C, a Fabry-Perot etalon filter for background rejection in the daytime, and a narrow bandwidth interference filter for background rejection at night. Table 5 lists the space-based water vapor DIAL system parameters.

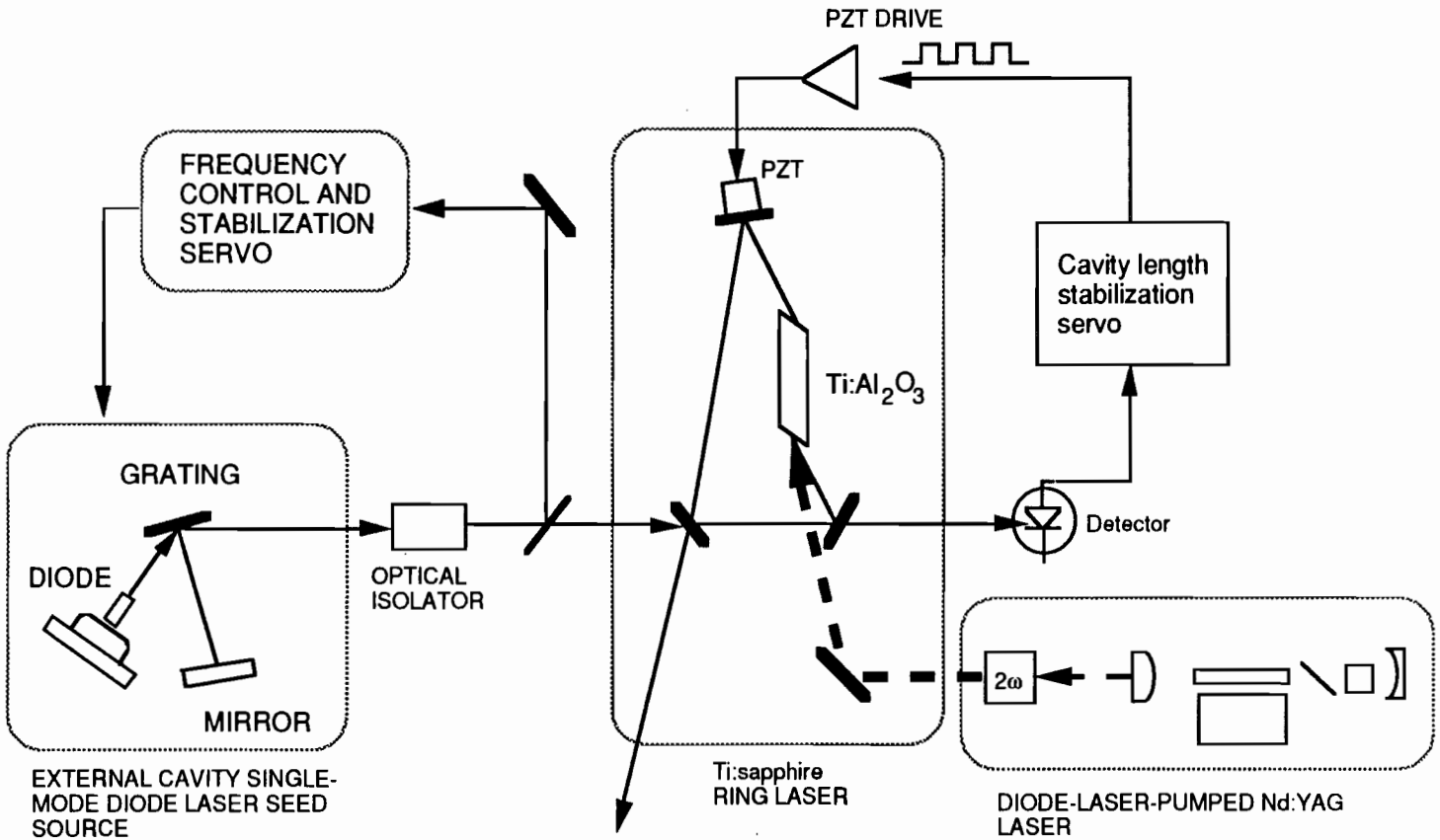

Figure 6. Injection-Seeded Ti:sapphire Ring Laser System Pumped by a Frequency-Doubled Diode-Laser-Pumped Nd:YAG Laser.

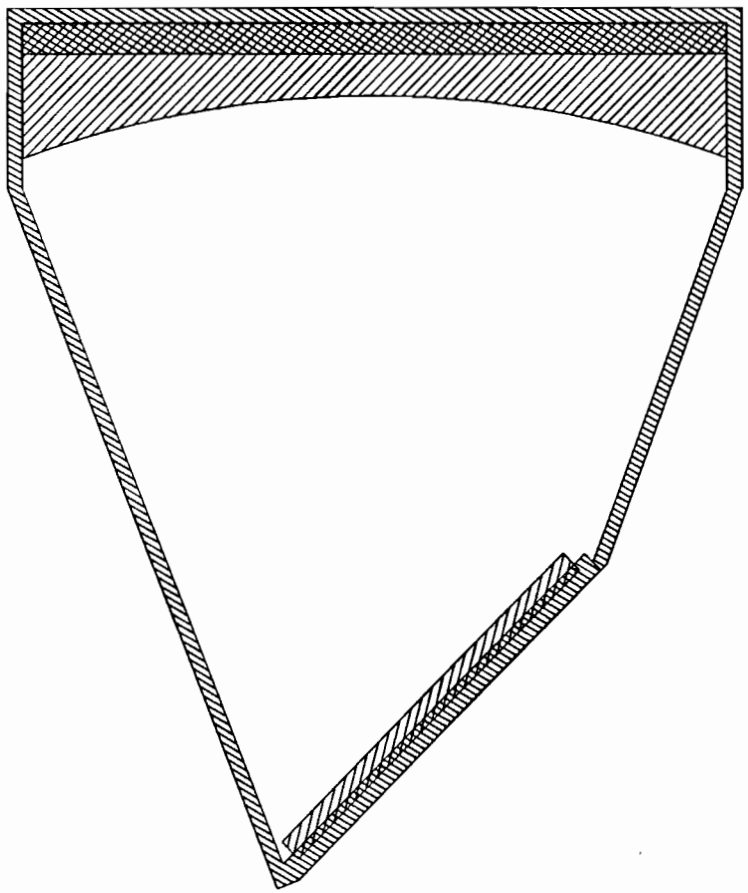

Specifications

SiC
Surface Figure λ/2 rms at 633 nm
Receiver Mirror : 30 cm f/1.5 parabolic mirror
Turning Mirror: 17 cm flat mirror

Figure 7. UAV Water Vapor DIAL Receiver Optical System.

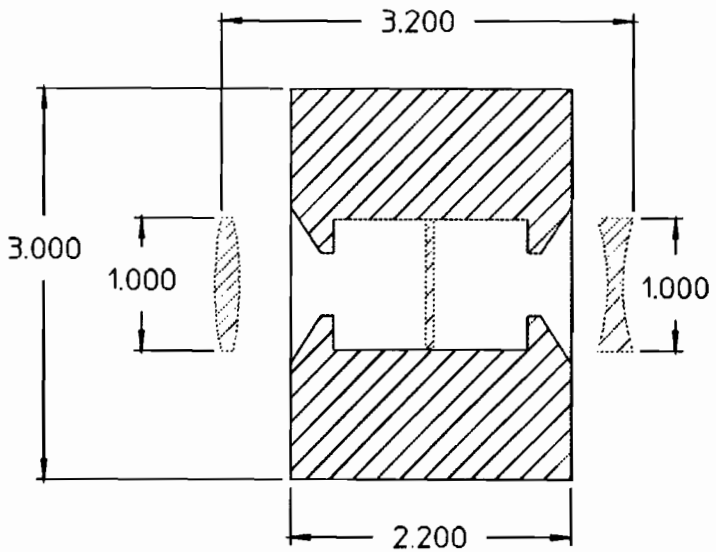

Custom Interference Filter

Center wavelength - 816.94 nm
FWHM - 1 nm
Minimum Peak Transmittance - 45 %
Andover Corp 010FC37-25

Temperature Controller

Regulation Accuracy - +/- 0.5 C
Ambient Temperature Range - 0 - 35 C
Min Regulated Temperature - 30 C
Max Regulated Temperature - 60 C
Power Requirements - 110VAC, 60Hz, .3A

Lenses

f/1.5 Negative Lens
f/1.5 Positive Lens
Surface Figure $\lambda/4$ rms at 633 nm

Figure 8. UAV Water Vapor DIAL Receiver Background Rejection Filter System. Dimensions are in inches.

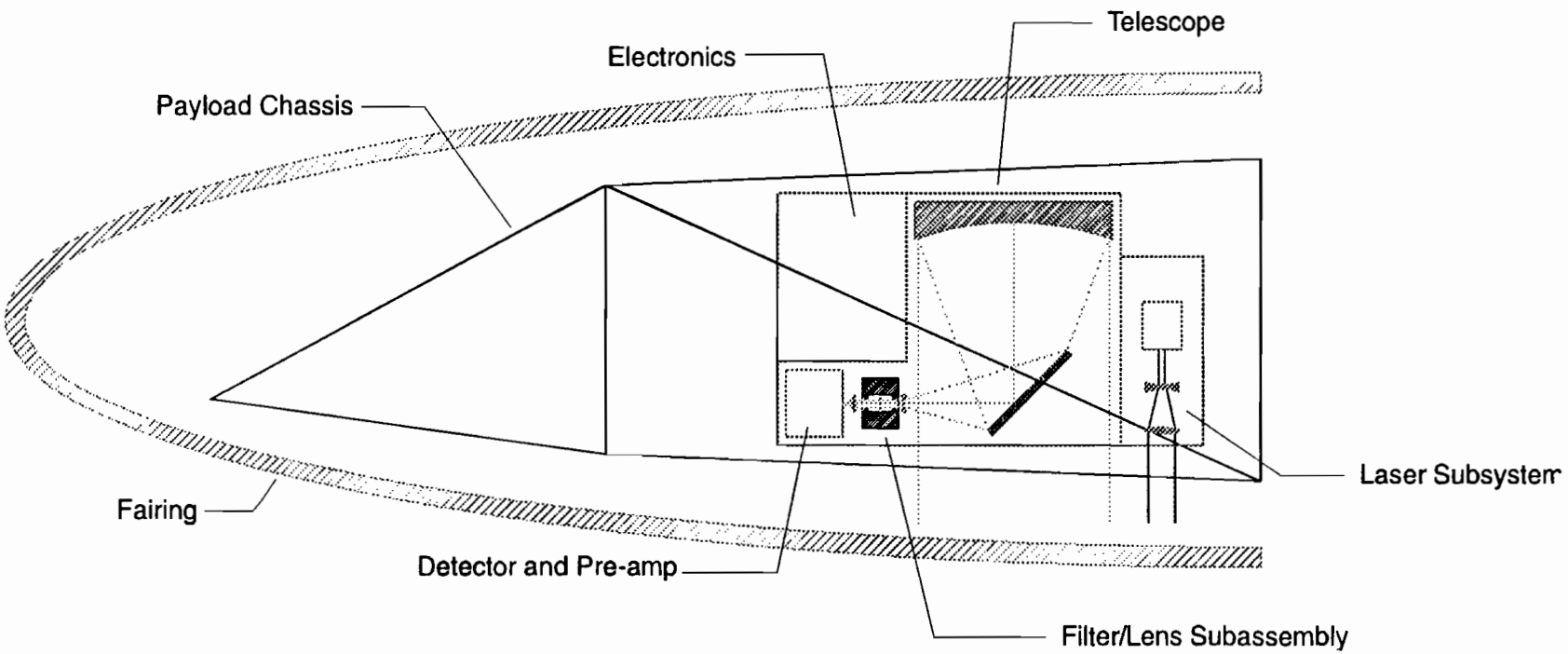

Figure 9. UAV Water Vapor DIAL System in a Perseus Pod.

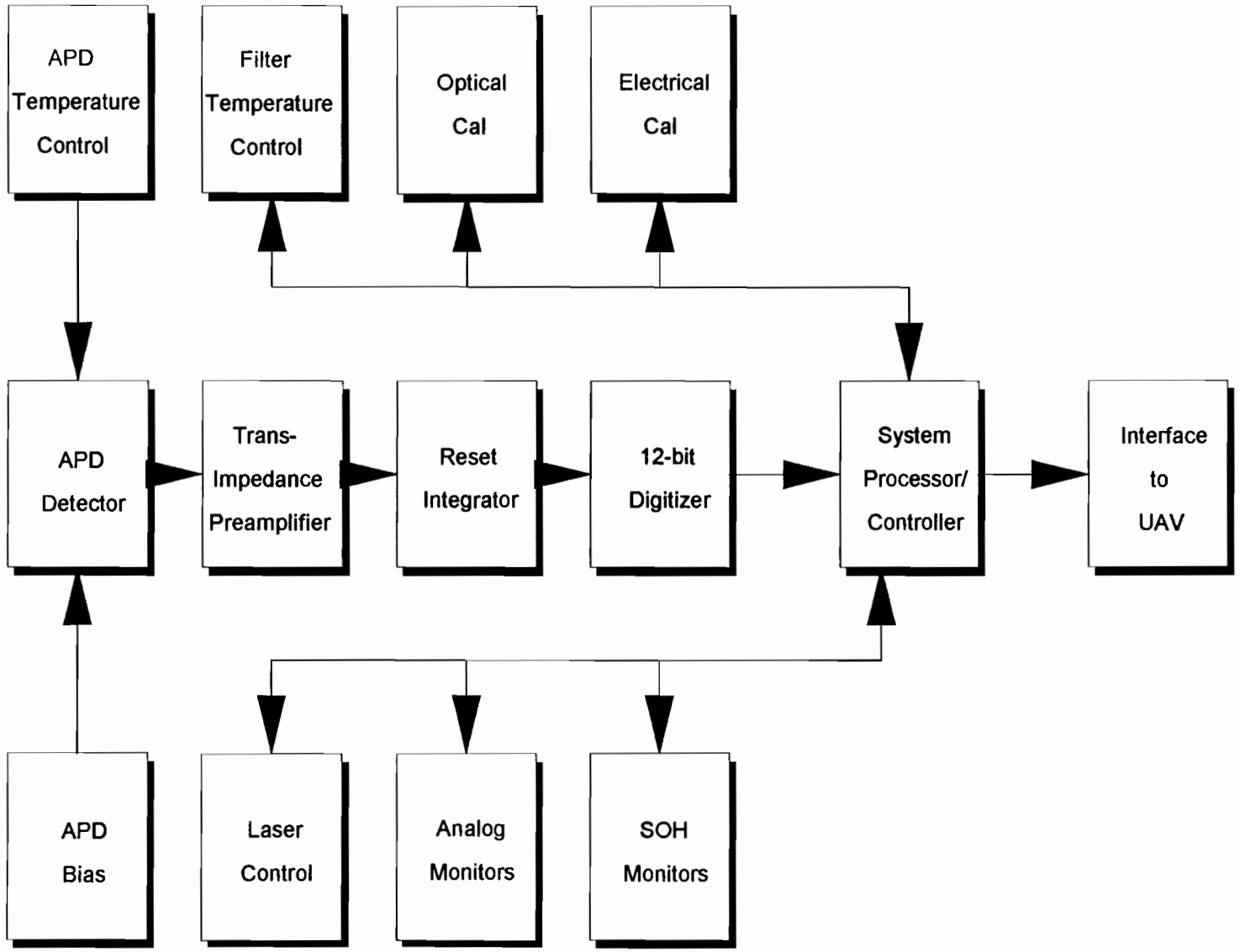

Figure 10. UAV Water Vapor DIAL Electronics Conceptual Block Diagram.

Table 4: UAV Water Vapor DIAL System Weight, Power, and Volume Estimates

Subsystem	Component Breakdown	Power	Weight	Volume
Electronics				
	Detector Bias & Temp. Control	5.10 W	----------	----------
	Signal Conditioning & Digitizer	4.80 W	----------	----------
	SOH Monitors & Calibration	1.22 W	----------	----------
	CPU, Controller, & Buffer	5.00 W	----------	----------
	Power Conditioning	4.93 W	----------	----------
	Mother Board	----------	----------	----------
	Mechanical Packaging	0.00 W	3.00 kg	----------
	Total - Electronics	21.05 W	10.00 kg	0.25 cu.ft.
Transmitter				
	Diode-pumped Nd:YAG Laser	100.00 W	4.00 kg	0.06 cu.ft.
	Ti:sapphire Ring Laser	0.00 W	4.00 kg	0.01 cu.ft.
	Injection Seed Lasers	4.00 W	4.00 kg	0.07 cu.ft.
	Faraday Isolator	0.00 W	1.00 kg	0.04 cu.ft.
	Frequency Stabilization Servo	10.00 W	5.00 kg	0.20 cu.ft.
	Mechanical Packaging	0.00 W	3.00 kg	----------
	Total - Transmitter	114.00 W	21.00 kg	0.38 cu.ft.
Receiver				
	Telescope	0.00 W	3.00 kg	1.73 cu.ft.
	Filter/Lens subassembly	----------	1.00 kg	0.07 cu.ft.
	Detector	----------	----------	----------
	Preamplifier	0.30 W	----------	0.06 cu.ft.
	Detector/Filter Packaging	0.00 W	2.00 kg	----------
	Total - Receiver	0.30 W	6.00 kg	1.86 cu.ft.
Chassis		0.00 W	10.00 kg	0.28 cu.ft.
System Totals		135.35 W	47.00 kg	2.77 cu.ft.

Table 5: Space-Based Water Vapor DIAL System Parameters

Parameters	Value	
Transmitter:		
Ti:sapphire Laser		
Laser Wavelength	~ 727 nm	
Laser Energy	200 mJ per pulse	
Laser Wall Plug Efficiency	2%	
Laser Divergence (FWHM)	0.1 mrad (Day)	0.395 mrad (Night)
DIAL Measurements Per Second	10	
Receiver:		
Diameter of Collecting Optics	1 m	
Full Field of View	0.1 mrad (Day)	0.395 mrad (Night)
Filter Bandwidth (FWHM)	0.03 nm (Day)	10 nm (Night)
Optical Transmittance (Total)	27.9% (Day)	41.8% (Night)
Detector Si APD at - 40 °C (C30902S)		
Quantum Efficiency	74%	
Gain	250	
Noise Equivalent Power	1.27×10^{-16} W/Hz$^{1/2}$	
Excess Noise Factor	3.484	
Amplifier Noise Current	1×10^{-13} A/Hz$^{1/2}$	
Other:		
Solar Spectral Radiance	414 W/(m^2 μm sr)	
Nighttime Background Radiance	.0041 W/(m^2 μm sr)	
Earth Albedo	30%	
Satellite Altitude	500 km	
Relative Ground Velocity	7 km/s	
Vertical Resolution	1 km	
Horizontal Resolution	100 km	

Table 6 lists the estimated performance of the space-based water vapor DIAL design. We can profile from 0 to 2 km with a DIAL measurement error of ≤ 10% and from 0 to 7 km with a DIAL measurement error of ≤ 23% with a daytime earth background using three water vapor lines in the 727-nm region. At night, we could profile water vapor from 0 to 6 km with a DIAL measurement error of ≤ 10% and from 0 to 8 km with a DIAL measurement error of ≤ 21% using three water vapor lines in the 727-nm region. Also at night, we could profile water vapor from 0 to 3 km with a DIAL measurement error of ≤ 10% and from 0 to 8 km with a DIAL measurement error of ≤ 21% just using two water vapor lines in the 727-nm region. These results are based on a Mid-latitude Summer model for molecular absorption and scattering and a rural 23-km visibility aerosol model.

Table 6: Estimated Performance for a Space-Based Water Vapor DIAL Conceptual Design; Mid-latitude Summer Model; Albedo = 0.3

Wavelength	Peak Absorption Cross section	Background	Range Profiled DIAL Error ≤ 10%	Range Profiled DIAL Error ≤ 23%
727.6848 nm	1.22E-27 m^2	Day/Earth	0 - 2 km	0 - 4 km
728.7379 nm	4.31E-27 m^2	Day/Earth	--------	4 - 6 km
727.7388 nm	7.01E-27 m^2	Day/Earth	--------	5 - 7 km
727.6848 nm	1.22E-27 m^2	Night/Earth	0 - 3 km	0 - 5 km
728.7379 nm	4.31E-27 m^2	Night/Earth	3 - 5 km	3 - 7 km
727.7388 nm	7.01E-27 m^2	Night/Earth	4 - 6 km	4 - 8 km

If we lowered the satellite altitude to 400 km, we could profile water vapor up to an altitude of 9 km in the daytime using three lines in the 940 nm region. However, the lifetime of a 400-km orbit is very short (1 month to 2 years), severely limiting the mission duration. If propellant is used to keep the satellite in the 400-km orbit, the mission duration could be extended. However, for our baseline system we will stick with a 500-km orbit because this orbit will meet the mission duration requirement without using propellant, thus simplifying the system and reducing its cost.

The technologies needed for a space-based water vapor DIAL need to be investigated further to ensure the feasibility of such a system. Specifically, we would need to look into the manufacturability, stability, and ruggedness issues for the Fabry-Perot etalon filter for a space-based application. We would also need to look further into the weight and power requirements for such a filter. Another technology driver for a space-based DIAL, which was not discussed earlier, is the transimpedence amplifier, the dominant noise source in the system. This amplifier must be carefully designed, and its input noise level rigorously modeled to ensure its noise is low enough to make a space-based DIAL system feasible.

Ground-Based Water Vapor DIAL Demonstration System

In an effort to understand system design requirements for rugged autonomous airborne and space-based systems, we decided to build a ground-based water vapor DIAL demonstration system to prove certain critical enabling technologies. They include an injection-seeded Ti:sapphire ring laser system, a microwave frequency stabilization servo, a narrowband multilayer interference filter, a thermoelectrically cooled silicon avalanche photodiode, and a low-noise-amplifier receiver subsystem. These will be integrated with a 14-inch telescope to collect the backscattered laser signals for both the on-line and off-line wavelengths. Once the signals have been acquired, they will be stored and processed on a computer. The DIAL system will be operated in a biaxial configuration, with the laser beam axis displaced from the telescope axis by

approximately 8.5 inches.

When completed, the Miniature Water Vapor DIAL Demonstration System will permit the acquisition of real data for use in validating our systems models, demonstrate the effectiveness of the component technologies, and will provide a better understanding the effects of error sources and how to compensate for them. The primary benefit of this work is in determining requirements for future lidar designs for airborne or space-based lidar systems. These platforms place demanding restrictions in such areas as power, weight, volume, and performance. Over-design reduces lifetime and capability while under-design compromises data integrity and mission success. A more complete understanding of the return signal characteristics and processing requirements, along with the capability to accurately model systems and predict performance, will provide necessary input for trade studies and permit the design of an optimum system for a particular application.

Transmitter System

The transmitter system consists of four main components. They are a Ti:sapphire ring laser, a miniature frequency-doubled Nd:YAG laser, single frequency diode lasers, and a dual-frequency-modulation stabilization circuit. The Nd:YAG laser is used to pump the Ti:sapphire ring laser. The dual-frequency-modulation stabilization circuit is used to precisely lock the diode laser to the water vapor line wavelength. Once the diode lasers are locked to the correct frequency, they are used to injection seed the Ti:sapphire ring laser, thus locking the Ti:sapphire ring laser to the correct frequency and improving the beam quality. The injection-seeded Ti:sapphire ring laser system and the dual-frequency-modulation stabilization circuit are discussed below.

Injection-Seeded Ti:sapphire Ring Laser System

The performance requirements for the DIAL laser system that were discussed earlier are summarized in Table 7. The laser must be tunable over the spectral region from ~813 nm to ~818 nm in order to access the DIAL absorption lines that have been selected in that region. The linewidth and pulse-to-pulse frequency jitter requirements are determined by sensitivity analysis of DIAL error with these parameters[3]. The pulse energy and repetition rate are determined by the performance modeling described earlier in this report.

The linewidth of the laser must be significantly narrower than the linewidth of the water vapor transition or significant measurement error in water vapor concentration will be made[3]. Typical linewidths for water vapor absorption are 0.2 cm^{-1} FWHM at STP, leading to laser linewith requirements of ~ 0.02 cm^{-1} (0.001 nm). Since the water vapor measurement depends on precise knowledge of the differential absorption cross section (that is, the difference between the cross section for the on and the off wavelengths), frequency jitter of the laser output can cause significant errors in water vapor concentration measurement. Hence, the requirement that the laser's frequency

Table 7: Laser Performance Requirements for a Miniature Water Vapor DIAL system

Parameter	Value
Wavelength Coverage	813 nm to 818 nm
Linewidth	0.02 cm^{-1} (0.001 nm)
frequency jitter	$\leq$ 0.01 cm^{-1} (0.0005 nm)
on-line / off-line frequency difference	0.5 to 1.0 cm^{-1} (0.025 to 0.05 nm)
pulse energy	15 mJ to 30 mJ
pulse repetition rate	25 to 40 measurements / sec

jitter be less than one-half the laser linewidth. Also, the laser system must be able to produce two different output wavelengths - the on and off wavelength - in rapid succession. Usually, the temporal separation between the on-line and off-line pulses is ~100 μs to 300 μs.

Based on the performance modeling effort described earlier, laser pulse energies of between 15 mJ and 30 mJ are sufficient to make water vapor measurements from an airborne platform. Also, measurement repetition rates of between 25 Hz to 40 Hz are required to provide adequate signal averaging while providing good spatial resolution from an airborne platform.

The laser system we have designed for the miniature water vapor DIAL system is an injection-seeded Ti:sapphire ring laser similar to the design of other[30,31] Ti:sapphire ring lasers. The injection-seeded Ti:sapphire laser, shown schematically in Figure 6, consists of a discrete-element Ti:sapphire ring laser, a single-frequency seed laser, a permanent-magnet Faraday isolator to isolate the seed laser from the high-power ring laser, and a Q-switched frequency-doubled Nd:YAG laser to pump the ring laser. In addition, a frequency stabilization system (described below) is used to ensure that the seed laser is tuned to the molecular absorption.

The ring laser architecture we have chosen has several advantages over conventional approaches, and makes rugged, compact, lidar systems possible. Since the modes in a ring laser are traveling waves, not standing waves, the ring laser does not suffer from spatial hole burning. As a result, it is much easier to build and operate a single-frequency ring laser than a corresponding standing-wave laser. Also, the geometry of the ring permits coupling of injection seeding light without a back reflection, thus providing natural optical isolation between the seed source and the ring laser.

In our design, the ring laser contains no intracavity frequency-selective components - the operating frequency of the ring laser is determined by the frequency of the injection seeding laser. Injection seeding provides a relatively simple and reliable frequency

control mechanism, and, when combined with the frequency control servo described in the next section, eliminates the need for bulky and heavy wavemeters for the DIAL measurement system. In addition to eliminating lossy frequency-selective components in the laser cavity, injection seeding provides a mechanism for forcing unidirection operation of the ring laser.

The injection seeding source we are pursuing is a single-frequency AlGaAs laser diode operating in an external cavity. Although laser diodes are inherently efficient and rugged, they are very susceptible to optical feedback and have relatively poor frequency jitter performance. When placed in an appropriately designed external cavity, however, the diode laser has exceptional frequency stability and immunity from optical feedback[32-34]. The operating frequency can be controlled by varying the diode current and/or temperature, by tilting the angle of the diffraction grating, or by changing the length of the cavity. Several commercial vendors are now selling diode lasers operated in external cavity configurations[35].

In order to demonstrate the feasibility of our laser design, we built and characterized the injection-seeded Ti:sapphire laser. The Ti:Al_2O_3 ring laser consists of a 2-cm-long by 8-mm-diameter Ti:Al_2O_3 crystal and three flat mirrors which form a 45-45-90 triangular lasing path. The round-trip path length inside the ring is ~190 mm, yielding an axial mode spacing of ~1.6 GHz. One of the mirrors is coated for 70% reflectivity at 817 nm and serves as the output coupler for the laser (as well as the input port for the injection seeding beam). The other mirrors are coated for maximum reflectivity at 817 nm. The Ti:sapphire crystal is end pumped by a Q-switched, frequency-doubled Nd:YAG laser which is transmitted through one of the high-reflectivity mirrors. The third mirror of the cavity is attached to a piezoelectric transducer to allow cavity length adjustment required to keep the ring cavity resonant with the seed laser frequency.

The Ti:sapphire ring laser reached threshold with approximately 25 mJ of 532-nm pump light in a 2-mm-diameter pump spot. The top-hat-shaped pump beam produced a pump fluence of ~ 0.4 J/cm^2, a factor of 25 less than the damage threshold of Ti:Al_2O_3. Above threshold, the laser output was bidirectional in the absence of an injection seeding beam. In the presence of an injection seeding beam the ring was forced to lase in one direction and produced single frequency output. In addition, the pulse build up time shortened from ~15 ns to ~5 ns. A minimum of 200 μW was needed to successfully injection seed the ring laser, although at this minimum level, the ring laser was quite sensitive to small alignment errors and vibration in the system. With an injection laser power of 500 μW, injection seeding was very reliable.

Figure 11 shows the output energy as a function of input pump energy for the injection seeded Ti:sapphire ring laser. The slope efficiency of the laser is 35%, comparable to results reported in the literature. The minimum required energy for the DIAL system, 15 mJ/pulse, is achieved with a pump energy of 65 mJ. The maximum output pulse energy, limited by the optical damage threshold of Ti:sapphire, was 35 mJ/pulse with

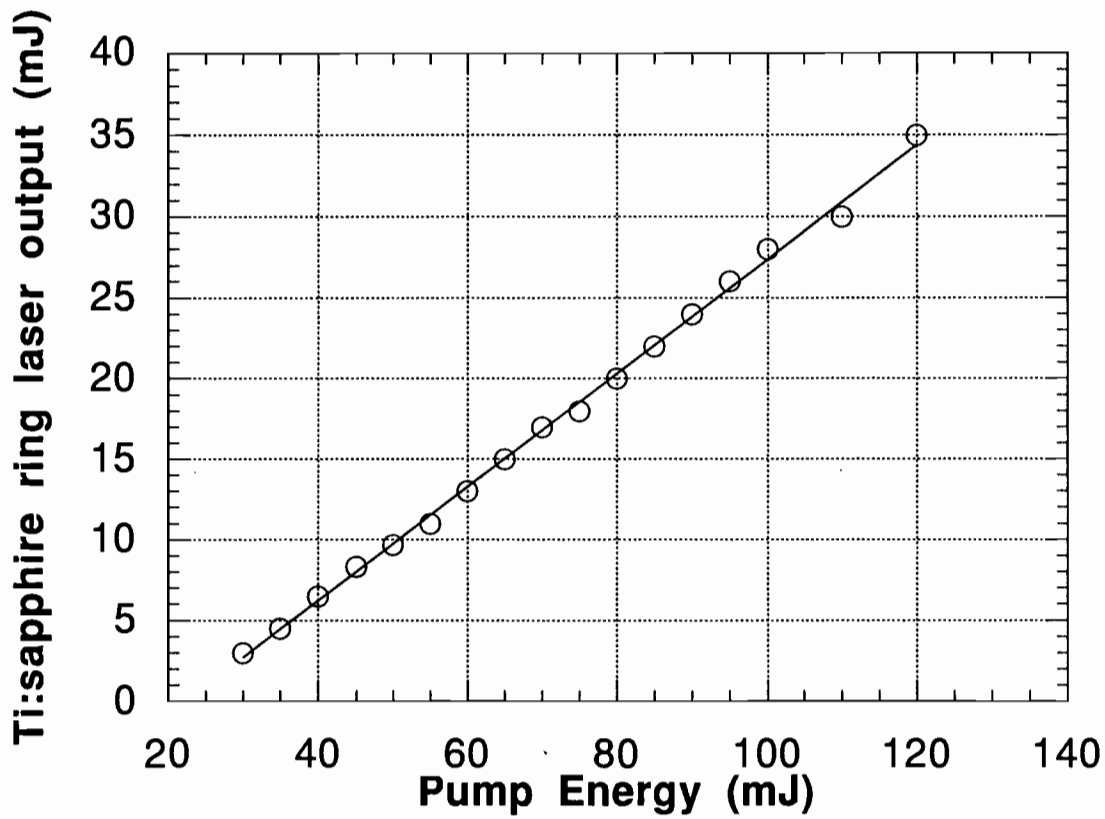

Figure 11. Injection-seeded Ti:sapphire ring laser output (near 817 nm) as a function of the 532-nm pump energy. The threshold of the laser is 25 mJ and the slope efficiency is 35%.

an input energy of 120 mJ/pulse. For normal operation of the Ti:sapphire ring laser, we recommend a maximum pump energy of 100 mJ, which yields an output energy of 28 mJ/pulse and provides a reasonable safety margin to the optical damage threshold of the material. (A pump energy of 100 mJ in a 2-mm diameter spot yields a fluence of ~1.75 J/cm^2, a factor of 6 below the damage threshold of 10 J/cm^2.)

The output beam of the ring laser was slightly elliptical in shape with measured $1/e^2$ diameters of 1.9 mm and 2.2 mm measured 1.2 meters from the output coupler. The measured beam divergence's were 0.82 mrad and 1.1 mrad respectively, indicating that the output beam is approximately 1.5 times diffraction limited.

Proposed Method of Switching between the On and Off DIAL Wavelengths

In order to alternate the output of the Ti:sapphire ring laser to the on and off wavelengths as required by the DIAL technique, the injection seeding input must be switched between these wavelengths. Since the temporal separation between the on and off pulses is on the order of 200 μs, it is unlikely that a single seed laser (using technologies available today) can be tuned and stabilized in that short an interval. Thus, two injection seeding lasers must be used for the DIAL system, with one tuned to the on wavelength and the other tuned to the off wavelength. These seed laser beams must be alternately introduced into the ring laser cavity since introduction of both seed beams into the slave cavity simultaneously may result in laser output on both of the seed frequencies. Our proposed method of switching between the wavelengths, shown schematically in Figure 12, consists of a polarizing beam splitter to combine the outputs from the two orthogonally polarized seed lasers into a single beam, and a Pockels cell to alternately flip the polarization of the beams when the $\lambda/2$ voltage is applied. After beam combination in the polarizer, the seed beam consists of two laser frequencies with orthogonal polarization. Only the p-polarized input beam will seed the ring laser due to the Brewster faces of the Ti:sapphire rod and the factor-of-two difference in the stimulated emission cross section for σ and π transitions in Ti:Al_2O_3. To alternate between on and off wavelengths, the voltage on the Pockels cell is switched between zero and the half-wave voltage, thereby rotating the polarization of the seed beams 90°.

Dual-Frequency-Modulation Stabilization

Many types of laser remote sensing, and particularly DIAL, benefit from a laser which is both broadly and precisely tunable . Modern diode lasers are easily tunable, but in general, lack a method of precisely determining their frequency. Fabry-Perot cavities are often used to stabilize lasers. When a laser is frequency locked to a cavity, its frequency will be stable, but not necessarily known or desirable. To determine the laser frequency, the cavity length must be precisely known. Also the number of laser wavelengths contained in the cavity must be known. De Voe and Brewer[36] have demonstrated a method of precisely referencing the cavity length to a radio frequency source, thereby achieving absolute frequency control to within the precision of the RF

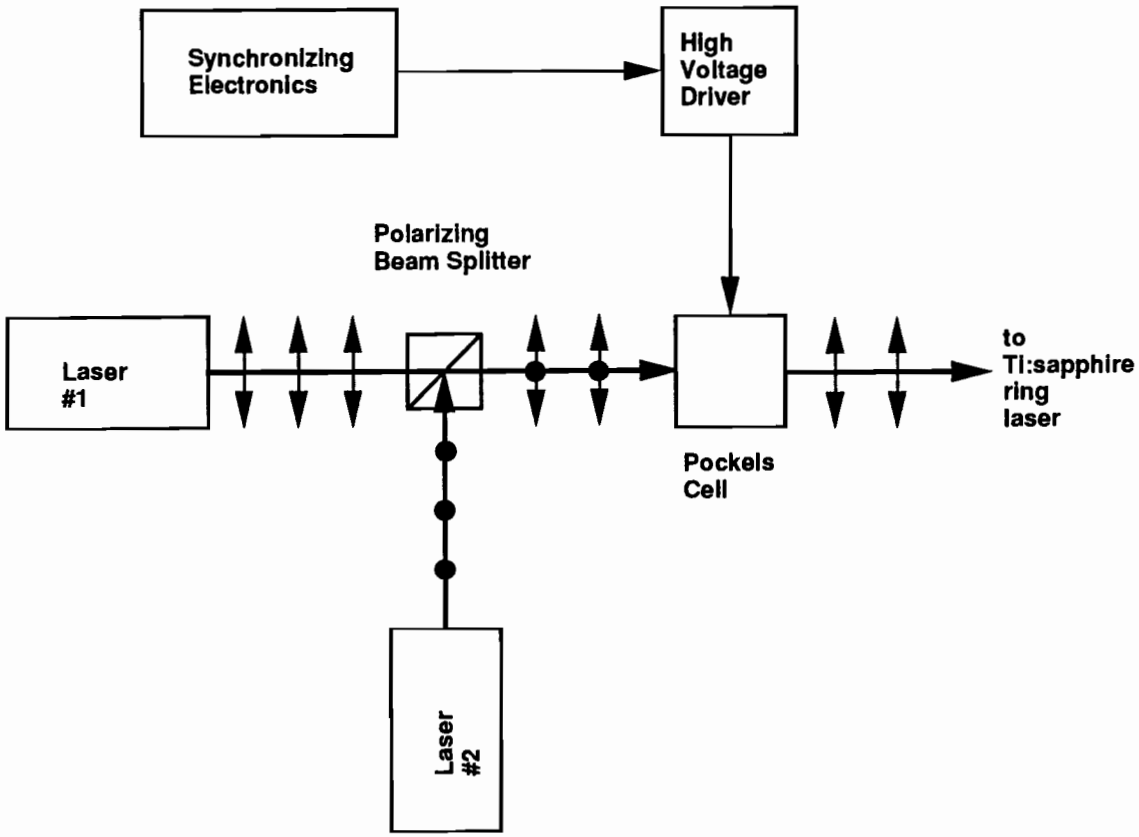

Figure 12. Proposed Method for Switching between the On and the Off DIAL Wavelengths. A polarizing beam splitter is used to combine the output beams from two injection seeding lasers so they can both be introduced into the Ti:sapphire ring laser cavity. The Pockels cell is used as a programmable $\lambda/2$ plate, rotating the plane of polarization of the seed beams 90° when the half-wave voltage is applied. Since only light of p polarization can seed the ring laser, the seed frequency can be alternated been the on and off frequency by alternating the polarization state of the beams.

source.

Our work involves extending the frequency of the radio frequency reference into the microwave range. This has two important advantages. First, it reduces the size of the optical cavity to a few centimeters. Second, and more important in our case, it reduces the number of laser wavelengths in the cavity to a few thousand. Thus, if the laser frequency can be estimated to an accuracy of one part in several thousand, say by measuring the laser current or with a simple grating, then its frequency can be known and controlled to better than one part per million.

The dual-frequency-modulation stabilization technique may be understood by reference to Figure 13. First consider the case of locking the laser frequency to the optical cavity. An r.f. oscillator at frequency ω_2 drives a phase modulator which induces sidebands at $\nu \pm \omega_2$. These sidebands mix with the reflected ν laser signal to produce an error signal at $\pm \omega_2$. When this signal is synchronously demodulated by the ω_2 signal, a d.c. signal is produced which can be used to control the laser frequency. For a more detailed description of this technique, refer to the paper by R. W. P. Drever[37].

Now consider a second phase modulator driven at microwave frequency $\omega_1 \approx c/2l$, where l is the optical length of the cavity. This will generate sidebands at $\nu \pm \omega_1$, but also (when combined with the first phase modulator) at $\nu \pm \omega_1 \pm \omega_2$. If the laser is locked to the cavity by the error signal at ω_2 described above, then the side band at $\nu \pm \omega_1$ will be nearly resonant with the adjacent cavity modes and will generate an error signal at $\omega_1 \pm \omega_2$. When this signal is synchronously demodulated by a local oscillator at $\omega_1 \pm \omega_2$, another d.c. signal is generated which can be used to drive the piezoelectric modulator controlling the cavity length. Thus, the cavity is locked to the microwave oscillator, and the laser is locked to the cavity.

We are currently constructing a dual-frequency-modulation stabilization circuit with ω_1 = 10 GHz. This is a significant departure from the 300 MHz demonstrated by De Voe and Brewer. There is no fundamental reason why the frequency cannot be increased much further, but some of the components are not yet commercially available. The high frequency of 10 GHz for ω_1 also requires that ω_2 be fairly high also - 512 MHz in our case. Both of these frequencies are sufficiently high that resonant, rather than broadband, phase modulators must be used.

We have assembled most of the optical components and have done some experiments injecting a frequency-stabilized HeNe laser into the interferometer. Because previous researchers had reported excellent results with very high finesse interferometers, we initially ordered mirrors with reflectivities specified at > 99.5%. However, these mirrors were delivered with very high reflectivity (or at least, very low transmission) and we were unable to get enough light through the first mirror to align the interferometer. When the first mirror was replaced with one with 1% transmission, the

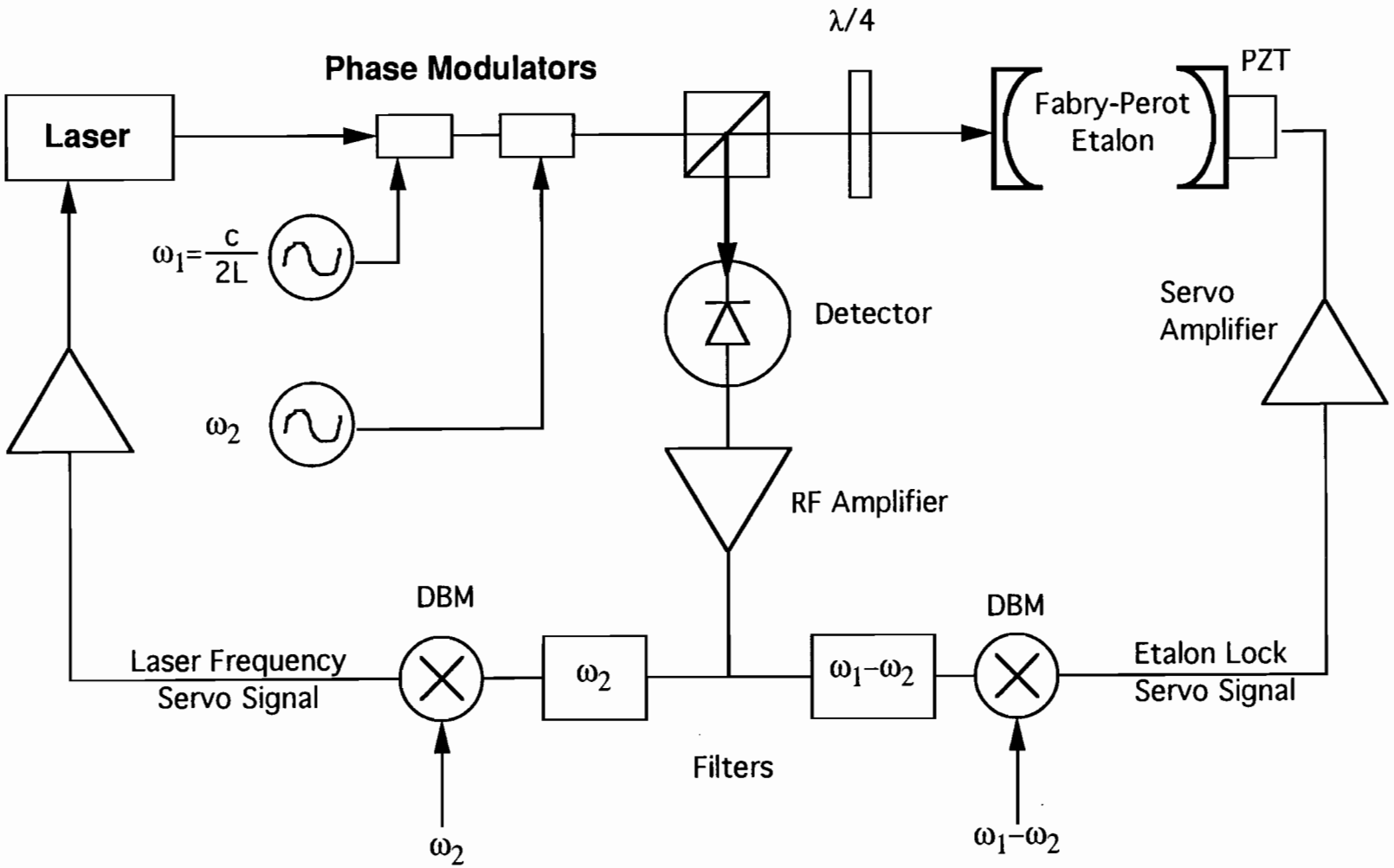

Figure 13. Schematic Diagram of Dual-Frequency-Modulation Stabilization Technique.

visual alignment was trivial, accomplished in a few seconds. We did discover that the PZT driver we were using to adjust the cavity length was defective, tilting quite noticeably when the cavity was scanned over a few modes.

This circuit will be used to control the Ti:sapphire laser in our water vapor mini DIAL experiment. Because the r.f. source can be quickly and easily changed, we will be able to explore the effects of tuning over the water line as well as changing to other lines and perhaps even other species, as long as they are within the tuning range of our laser.

Receiver System

The receiver system consists of an optical sensor system, supporting electronics, and a data acquisition system. The optical sensor system includes a light collecting telescope and a lens/filter/detector assembly. The backscattered laser light will be collected by the telescope, filtered, then focused onto a detector. The electrical signal out of the detector will be processed by the supporting electronics and then sent to the data acquisition system. The data acquisition system will allow us to store and process the DIAL backscattered signals to determine the water vapor concentration as a function of altitude. The optical sensor system, electronics, and data acquisition system are discussed below.

Optical Sensor System

In order to save time and money, we decided to use an existing 14-inch (f/11) Celestron telescope for the optical receiver system. Although this telescope is not optimized for an airborne or space-based platform due to its weight, its aperture size will permit accurate water vapor measurements over a large range for the ground-based demonstration system. The weight of the telescope system can be reduced significantly for an airborne or space-based application by modern lightweighting techniques and is not considered a critical enabling technology. The Celestron telescope is a Schmidt-Cassegrain catadioptic design consisting of a primary and secondary mirror, and a Schmidt corrector. The telescope brings the light to focus a few inches behind the primary mirror at the back of the telescope.

A lens/filter/detector assembly will be placed at the back of the telescope 3 inches before the telescope focus to collimate the light as its going through a narrow band optical filter and then to focus the light onto a thermoelectrically cooled Si:APD. The lenses are one-inch-diameter planconcave and planoconvex lenses from Newport Corporation (f/3). The narrowband optical filter is from Andover Corporation and has a bandwidth of 1 nm and a peak transmission of 70% at 816.9 nm. The filter will be housed in a heater to accurately control the temperature of the filter. This is necessary to ensure that the bandwidth is centered on the DIAL lines and will not drift off of the lines as the ambient temperature changes. The detector is an RCA C30902S Silicon APD that is thermoelectrically cooled with a single stage cooler to -5 °C. The detector has a quantum efficiency of 74% at 817 nm. It is connected to a low-noise amplifier receiver

subsystem which is discussed in the next section.

Receiver Electronics

Receiver systems for deployable autonomous lidars require signal conditioning, digitization, and signal processing techniques that are optimized to the specific lidar application and deployment scenario. This optimization process requires that performance goals be contrasted against the constraints of weight, power, volume, schedule, and budget. For this process to be successful, it is necessary to fully understand the impact of the design trades made, particularly with respect to the choice of detector, system bandwidth, digitizer resolution, and sampling rate. This portion of the ground-based water vapor DIAL demonstration system activity focused on establishing the current state of practice in lidar receiver technology and, using that information, developing the knowledge base necessary to perform the system level trade studies for future deployable lidar systems.

The typical research lidar system consists of a commercial "light bucket" telescope mated to an appropriate filter and detector combination. Off-the-shelf amplifiers and digitizing instruments are used for signal acquisition, and a small computer system is used for data processing, display, and system control. Because they are research systems, the electronics are typically not optimized for a specific application and are frequently chosen with a single characteristic in mind, such as high speed or even availability of components. In an effort to establish the critical parameters for the receiver electronics, literature searches, along with conversations with researchers in the lidar area, were performed. It was discovered that, while a great deal of effort is being put into the phenomenology and solid-state laser development areas, the receiver electronics for most of the research systems are developed with minimal attention to detail. This is largely due to the fact that these systems are van based and, due to essentially unlimited space and power availability, it is easy to choose components that are "over-designed" for the application. However, it was noted that only minimal attention was being given to the impact of the receiver electronics on the integrity of the detected signals. Specifically, the only filtering being performed was that inherent in the amplifiers and digitizer, and few efforts were made to characterize the response of the front-end electronics beyond what was available in the manufacturers' electronics data. In addition, attention was not being paid to whether or not aliasing is occurring in the data acquisition process. As a result, the surveys made it impossible to define the minimum set of requirements for the receiver electronics from current practices because validated data does not appear to be available.

Because this information was unavailable from other sources, it was decided that the most profitable approach would be to design a receiver system that could be used to obtain validated lidar data which could subsequently be used to understand the effects of the various electronics error sources (noise, linearity, etc.). This was accomplished by first developing a conceptual understanding of the signal, defining representative performance levels, determining a conceptual approach for the electronics, and

modeling the performance of the system. Then the receiver electronics and computer control and analysis system were designed and fabricated.

Receiver Signal Theory

It is possible to infer several receiver requirements by examining the propagation and collection of the optical signal. The first signal characteristic that can be inferred is the dynamic range. It is important to distinguish between measurement dynamic range, and instrument dynamic range. Measurement dynamic range refers to the maximum range of signals the receiver can see from a single set of atmospheric and background conditions. Instrument dynamic range deals with the range of signals received over the various operational scenarios for the instrument. The distinction here is that, for a research system, it is easy to adjust gains or offsets to permit the acquisition of signals over widely varying conditions. For this case, only measurement dynamic range is important. However, an autonomous system will have to operate over the wide variety of conditions, so instrument dynamic range is important. When the electronics has insufficient dynamic range for the signal received, one of two situations arises. For low amplitude signals, system noise and quantization error will result in large uncertainties in the data. For high amplitude signals, clipping and saturation of the front-end electronics will occur. This not only introduces large errors, but there is a significant recovery time from saturation, resulting in the system being blind for all or part of the acquisition period.

Lidar systems typically require a high measurement dynamic range because the solid-angle subtended by the receiver optics is a function of inverse range squared. This results in the return signal which exhibits a rapid decay with increasing range. The actual return signal close to the receiver may be reduced by lack of overlap between the transmitter beam and the receiver FOV and image blurring due to the telescope focus position being optimized for imaging objects very far away (infinity). In situations where it is not necessary or desirable to make measurements close to the receiver, the optics can be intentionally misaligned so that the laser pulse and the optics field-of-view do not overlap until some distance from the receiver. This reduces the measurement dynamic range and can prevent saturation of the receiver electronics from near returns. Instrument dynamic range will be equal to or greater than the measurement dynamic range, depending on the range of background signals in the deployment scenario. This specification depends mainly on the bandwidth of the optical filter used, the wavelength of operation, and whether the system is to be used under day and/or night conditions. Variations in any of these parameters results in an increase or decrease in the DC component of the signal.

The requirement for high dynamic range impacts the receiver electronics design in two ways. First, if the instrument dynamic range is significantly larger than the measurement dynamic range, then provisions must be made for removing the resulting DC offset in the electronics. While this can be implemented as a programmable offset summed with the detector output, the most straightforward method is to use feedback

compensation as shown in Figure 14. Using this technique, the signal (after several stages of amplification) is integrated and fed back to the preamplifier summing junction as a current which is equal in magnitude but opposite in sign to the background current being produced by the detector. The integrator has a long time constant in order to prevent it from trying to compensate out the signal current. The disadvantage of this and other background compensation techniques is that they significantly increase the noise gain of the preamplifier, so they should be avoided if possible. This effect is discussed below in the section on performance modeling.

High measurement dynamic range also impacts the linearity requirements of the receiver electronics. For the case where the system is operated in elastic backscatter mode, linearity errors in the electronics will propagate directly to the computed backscatter coefficient due to the range squared correction built into the equation. With a DIAL system, the concentration of a particular molecule is proportional to the natural log of the ratio of the signal returns for two adjacent range bins. Again linearity errors can be propagated to introduce errors in the computed concentration. However, errors introduced by the electronics nonlinearity are usually small compared to the errors present in the estimates of atmospheric coefficients, so they should not dominate in the system.

The second signal characteristic that can be inferred is the bandwidth required for a given range bin size (vertical resolution). The frequency content of the return signal is given by the convolution of the spatial variation of the scattering medium (molecular or aerosol) and the spatial pulse width of the laser. The translation from the spatial domain to the temporal domain is accomplished by multiplying by 1/c (speed of light) and taking into account the round trip propagation distance or time. The spatial frequency content of the scattering medium, which is in most cases the atmosphere, can possibly be inferred from turbulence-induced-variations in the medium. While the spatial characteristics of turbulence are not directly related to the distribution of the aerosols or molecules which perform the scattering, turbulence acts to redistribute the aerosols or molecules and thus establishes the limits over which homogeneity can exist. This places an upper limit on the spatial frequencies present in the scattering function. According to turbulence theory[38], the 2/3 structure function law is valid over a range defined by the inner scale l_o and the outer scale L_o. The inner scale sets the limit on the spatial variations due to turbulence because viscosity effects dominate the fluid flow below this point. Thus, l_o establishes the minimum spatial extent (or maximum spatial frequency) over which turbulence can occur. The outer scale sets the maximum spatial limit over which homogeneity can be reasonably expected, thus setting the lower limit for the start of the rolloff of the frequencies present in the turbulence transfer function. The inner scale ranges from a few millimeters at ground level to centimeters or more in the stratosphere. The outer scale ranges from tens to hundreds of meters over the same altitude increment. Both are a strong function of altitude.

To relate turbulence to scattering, one can view the act of performing a measurement with a lidar system as, in effect, taking a "snapshot" of the spatial turbulence. Thus, the

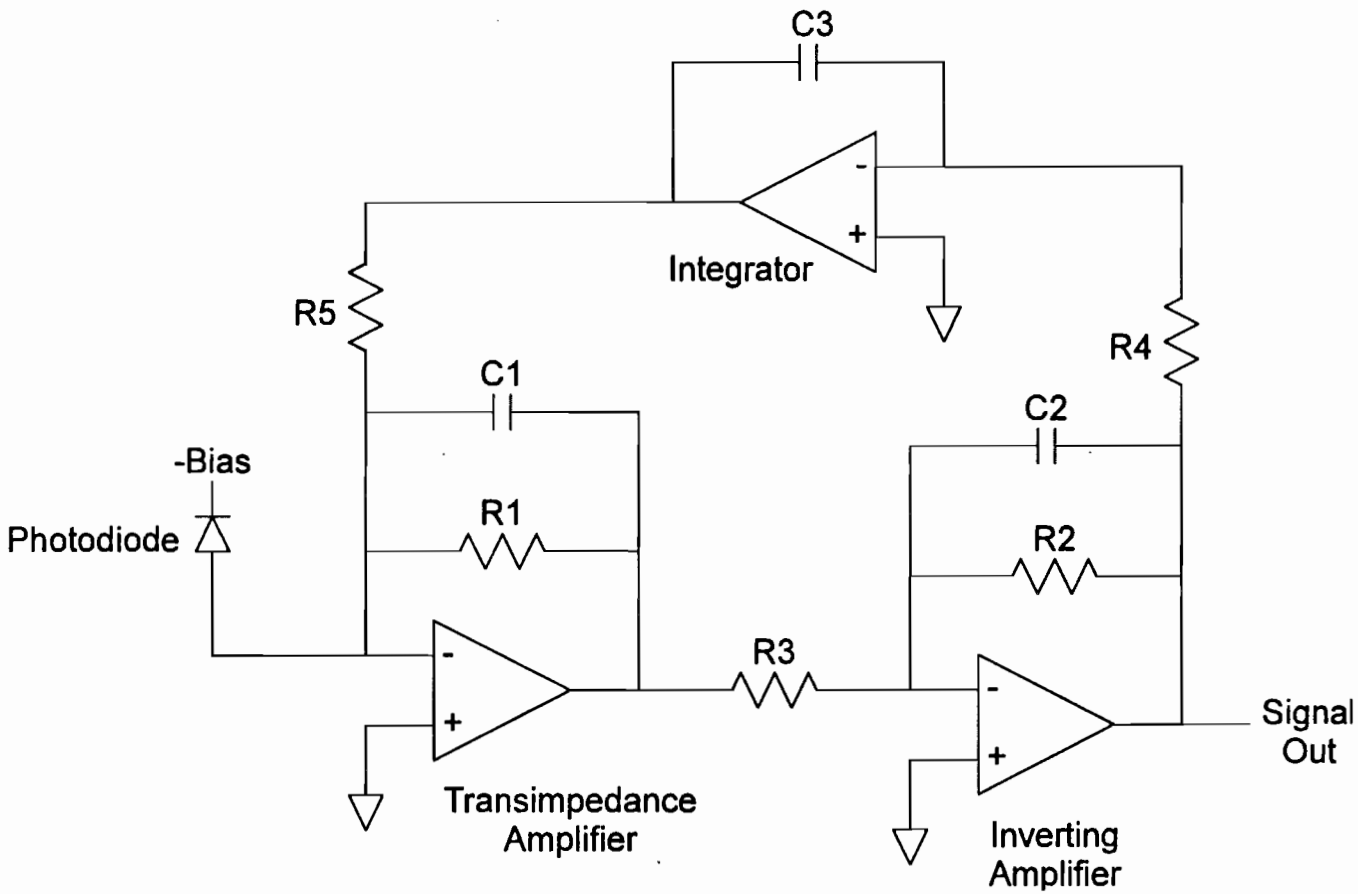

Figure 14. Background Feedback Compensation.

outer and inner scales can be translated into the spatial frequency domain and implied effects on the scattering function can be examined. Using this view, it can be inferred that the outer scale and inner scale will correspond to poles in the scattering function, resulting in rolloff at high frequencies. The outer scale implies that frequencies above 15 MHz (spatial variations over 10 m) have to be present in the return signal, and the inner scale implies that frequencies out to 100 GHz could be present. Which situation dominates will depend on a variety of factors, including altitude, horizontal vs. vertical propagation, type of distribution (atmospheric vs. plume), etc. For the case of an effluent plume released by a manufacturing facility, the transition from "clear air" to plume can occur over a distance of 1 m or less, particularly close to the stack. In the case of profiling atmospheric constituents, well defined (spatially short) transitions can also occur. This can be observed simply by flying on an aircraft passing through clouds.

The above argument relates to the design of lidar receiver system in the following way. While conditions can exist where large regions of homogeneity exist in the scattering medium, it is reasonable to expect worst case conditions in which changes occur over short spatial dimensions. It is this worst case, in which the return signal contains extremely high frequencies, that needs to be considered in the design of the receiver so as to preserve the integrity of the data. If one assumes a spatial variance over a length of < 30 cm, the medium will exhibit spatial frequencies out to at least 500 MHz. Fortunately, because of the convolution of the laser pulse with the scattering medium, the apparent spatial extent of the laser pulse will limit the temporal frequency spectrum of the return signal. Laser pulse widths for lidar systems typically range from 5 ns (1.5 m) to 30 ns (9 m). Due to the round trip travel time of the laser pulse, the light arriving at the receiver for every instant in time represents the integration of the scattering phenomena over a range bin which is half the spatial extent of the laser pulse. The following example illustrates this effect. If we transmit a pulse of temporal full-width half-maximum (FWHM) width τ and look at the instantaneous return signal observed at time $t = t_1$, the leading edge of the pulse has traveled an apparent distance (relative to the receiver) of:

$$d_l = \frac{ct_1}{2} \qquad [m]$$

where d_l is the apparent distance to the leading edge of the laser pulse and c is the speed of light. Because the trailing edge of the pulse left the laser at a time $t = \tau$ later than the leading edge, the trailing edge travels an apparent distance of:

$$d_t = \frac{c(t_1 - \tau)}{2} \qquad [m]$$

where d_t is the apparent distance to the trailing edge of the laser pulse, and τ is the laser FWHM pulse width. Solving for the spatial range bin width $\Delta R = d_l - d_t$ yields:

$$\Delta R_{min} = \frac{ct_1}{2} - \left(\frac{c(t_1 - \tau)}{2} \right) \qquad [m]$$

Which reduces to:

$$\Delta R_{min} = \frac{c\tau}{2} \qquad [m]$$

This has several implications. First, ΔR_{min} represents the theoretical minimum vertical range resolution possible for a given lidar system. The actual range resolution will depend on the amount of smearing caused by the tails of the laser pulse, and on whether the bandwidth of the receiver electronics is high enough to preserve ΔR_{min}. Second, the signal received is equivalent to the convolution of the spatial variation of the scattering medium and a spatial pulse represented by half the FWHM pulse width of the laser. Assuming that the laser pulse has a Gaussian distribution, this convolution is equivalent to a spatial low pass filter with a 3 dB frequency approximated by:

$$f_{laser} \approx \frac{1}{2\pi\frac{\tau}{4}} = \frac{2}{\pi\tau} \qquad [Hz]$$

Because the spatial filter created by the propagation of the laser pulse is a true integrator with a Gaussian impulse response, the rolloff of the filter response is very sharp. At $5 \times f_{laser}$ the response is down over 100 dB.

For the case where it is desired to approach ΔR_{min}, the design of the receiver electronics is very straight forward. The electronics transfer function must have a 3 dB frequency $f_{3dB} > f_{laser}$ and the data must be sampled at a frequency in the range $5 \times f_{laser} < f_s < 10 \times f_{laser}$, depending on digitizer resolution, in order to prevent aliasing. In the case of a lidar system using a 20 ns laser pulse, frequencies out to 32 MHz will be unattenuated in the return signal, and a sampling rate of 160 MHz to 300 MHz is required to prevent corruption of the data. However, for the case where $\Delta R > \Delta R_{min}$, the design decisions are more complex. By solving the equation $\Delta R_{min} = c\tau/2$ for τ and substituting the result into the f_{laser} equation above, we can infer that:

$$f_{3dB} \approx \frac{c}{\pi \Delta R} \qquad [Hz]$$

where f_{3dB} is the required receiver integrator bandwidth and ΔR is the desired vertical range resolution. Note that this equation only holds when the receiver is implemented as a true integrator. For non-integrating receivers, it establishes the lowest acceptable 3 dB frequency which will still permit extraction of the desired mission data. While the high frequency information may not be required for this case, its presence in the form of aliased signals could corrupt system measurements. Thus, it is necessary for the

receiver electronics design to take this into account to prevent signal aliasing.

Design Philosophy and Requirements

The design concept for the ground-based water vapor DIAL demonstration system receiver is predicated on two sets of requirements. First, the system concept establishes the requirements for range resolution, signal levels, dynamic range, and desired receiver electronics noise performance. Second, the desire to develop the information base necessary to specify the optimum receiver requirements for a given lidar application governs the choice of design approach.

The system requirements, based on the atmospheric and detector modeling, are shown in Table 8.

Table 8: Ground-Based Water Vapor DIAL Receiver Electronics System Requirements

Parameter	Value
Range Resolution (ΔR)	330 m
Expected Minimum Signal	>1.3 nA
Expected Maximum Signal	<2.5 μA
Measurement Dynamic Range	<2000
Instrument Dynamic Range	unspecified
Electronics Noise (input referred)	100 $fA/Hz^{1/2}$

Keeping in mind that the above requirements are derived from modeling activities and the fact that this is a research activity, it was desired to build as much flexibility as possible in the receiver system. First, the preamplifier board was designed to accommodate a variety of avalanche photodiode (APD) detectors. Second, the dynamic range requirements were adjusted in anticipation of varying operating conditions. Finally, the data acquisition electronics were designed for maximum flexibility and to preserve signal integrity. Variable bandwidths, sample rates, profiling ranges and detector biases are all provided.

With respect to the topology used for the receiver electronics, two approaches were examined. The first was to use a dual reset integrator configuration. This approach implements, as near as possible, the ideal integrator discussed above, and is shown in Figure 15. In this approach, a nearly ideal integration is performed over the interval corresponding to a range bin. Dual integrators are used in alternating fashion to mitigate the non-ideal response introduced by the finite reset period. There are two primary drawbacks to this approach. First, while a dual reset integrator configuration comes very close to the ideal integrator desired, its application is limited to cases where coarse spatial resolution is required. This is because it is difficult to reset the

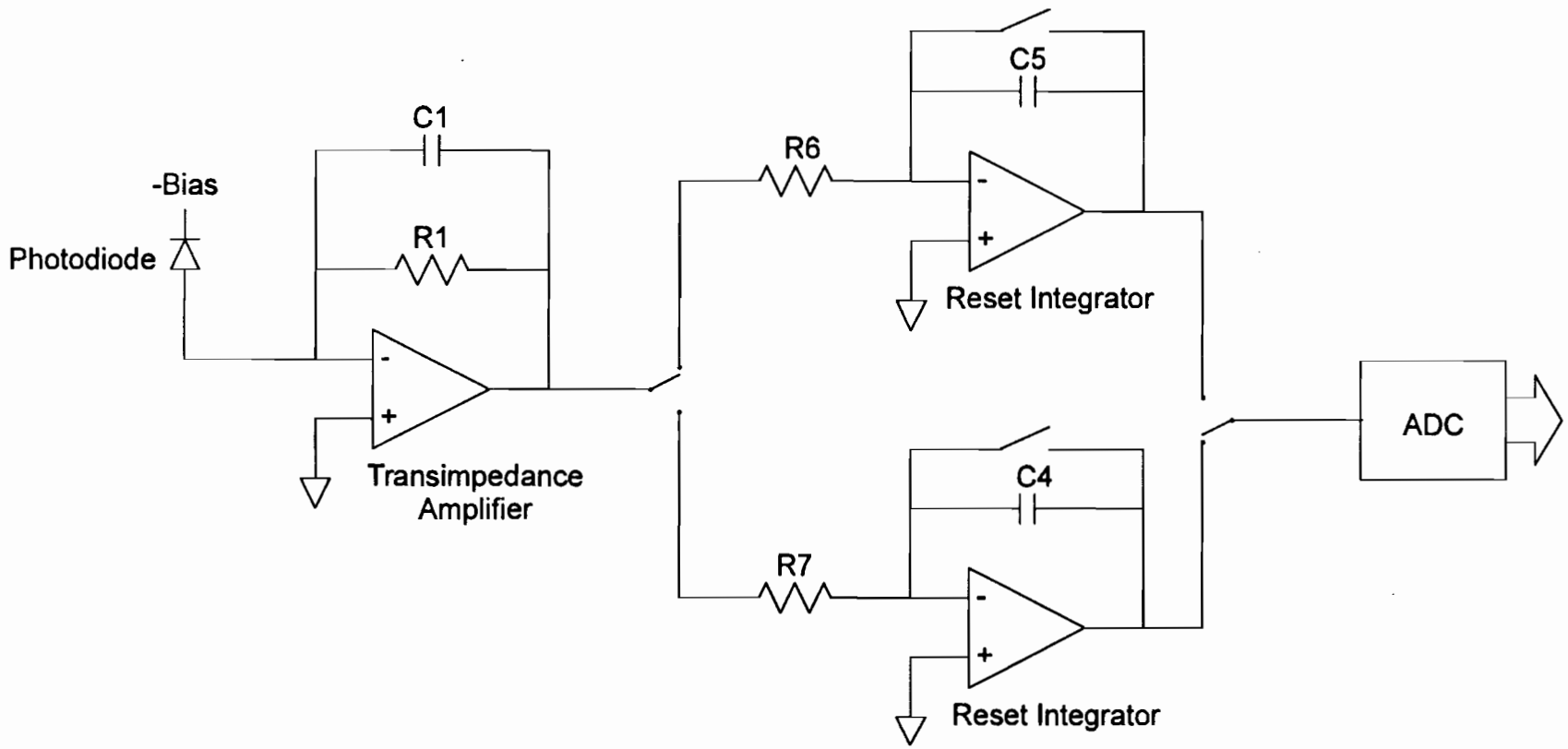

Figure 15. Dual Reset Integrator Circuit Topology.

integration capacitor faster than about 500 ns without introducing significant noise into the signal. While this would be good enough for the ground-based water vapor DIAL demonstration system, higher spatial resolution lidar systems would not be able to use this configuration. Second, the integration process is, in effect, an infinite bandwidth operation which results in an inability to reconstruct the original signal. One of the primary motivations for developing this system is to establish the optimum requirements for a lidar receiver. To do this, it is necessary to be able to evaluate models of alternate electronics configurations using validated data. For these reasons, this approach was not taken.

The approach chosen was to design a "well-behaved" front-end. In this case, it is necessary to have sufficient bandwidth to pass signals of interest without distortion and also well-understood amplitude and phase characteristics to permit signal reconstruction (no temporal or spatial aliasing) and deconvolution of the electronics transfer function. This will be the design approach presented.

Design Topology

From the above information it is possible to develop the specific requirements for the receiver electronics. From the equation listed above it can be seen that a 330 m range bin, which corresponds to a temporal sampling interval of 2.2 μs, requires that the receiver electronics have a minimum 3 dB cutoff frequency on the order of 290 kHz. This was implemented using a transimpedance amplifier (TIA) as the preamplifier for the APD, which was followed by a fourth order Bessel low-pass anti-aliasing filter. Because linearity errors and distortion must be minimized, the filter was limited to a 4^{th} order configuration. A Bessel filter configuration was chosen due to its flat amplitude response and linear phase, or constant time delay, characteristics. The time delay of the front-end is important because variations translate directly into frequency dependent spatial errors. Traditional anti-aliasing filters exhibit up to a factor of 2.5 increase in delay as they approach the transition band, while a Bessel filter is flat over the entire passband. The disadvantage of this choice is that a Bessel filter has a very wide transition width which, when applied as an anti-aliasing filter, results in a higher sampling rate. As a result, temporal samples are averaged to get back down to the effective sampling rate which corresponds to the range bin size. The signal from the filter is applied to an offset pair of 12-bit analog-to-digital converters (ADC's) which provide for an instrument dynamic range of 64000:1. While a single 12-bit device should be sufficient for the required dynamic range, it was desired to accommodate widely varying operating modes, so additional dynamic range was included. A block diagram of the receiver front-end is shown in Figure 16. The design requirements are summarized in Table 9.

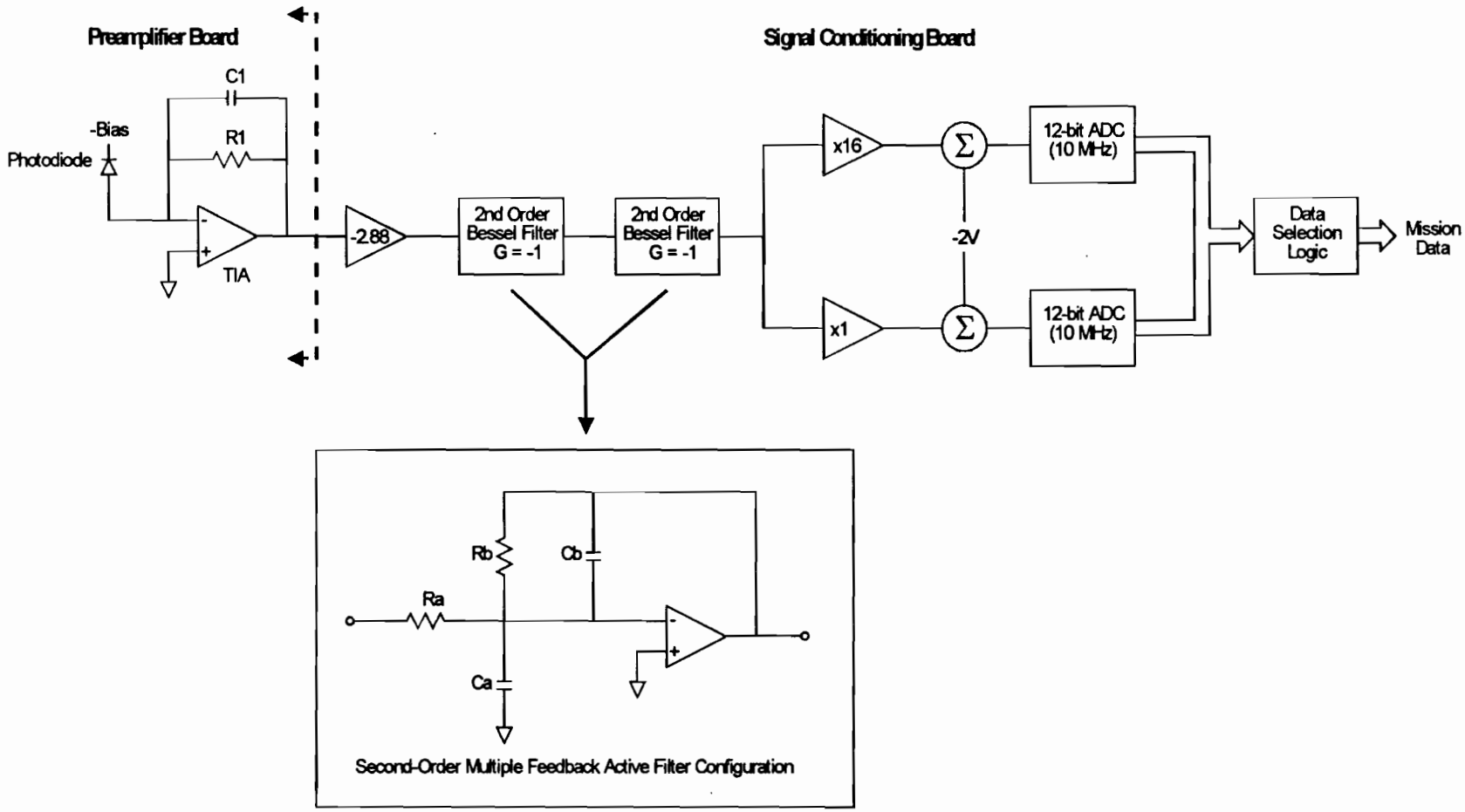

Figure 16. Receiver Front-end Electronics Concept.

Table 9: Ground-Based Water Vapor DIAL Receiver Electronics Design Requirements

Parameter	Value
Range Resolution (ΔR)	330 m
System Bandwidth	290 kHz
Sampling Rate	10 MSPS
Attenuation at Nyquist	100 dB
Saturation Level	7.2 μA
LSB Signal	110 pA
Instrument Dynamic Range	65536 (two 4096 ranges with x16 offset)
Temporal Averaging	22 samples/range bin
Electronics Noise (input referred)	100 $fA/Hz^{1/2}$

Hardware Description

Based on the above requirements, the front-end hardware was designed. The preamplifier chosen is a Burr-Brown OPA637 operational amplifier configured as a TIA. This device was used because it combined high bandwidth, low-noise, and low input bias current. In order to assist with the optimization of the preamplifier design and to quantify the performance of the system, an electronics model for the TIA was developed for the front-end utilizing Mathcad© software. The model converged on a design with a bandwidth of 412 kHz and a gain of -0.193 V/μA. The bandwidth was chosen to provide sufficient headroom to maintain the 290 kHz bandwidth requirement, and the gain was maximized within the constraints for noise and stability described below.

The model shows that at low frequencies, the voltage noise of the amplifier dominates. At midband and high frequencies, the noise contributions of the preamplifier feedback resistor dominates the performance of the system. This illustrates one of the major drawbacks to transimpedance amplifiers. The transimpedance (current-to-voltage) transfer function is given by:

$$\frac{V_o}{I_i} = \frac{-R_1}{(1+sR_1C_1)\left(1+\frac{1}{A_v}\right)} \qquad \text{[Ohms]}$$

where V_o is the amplifier output voltage, I_i is the amplifier input current, A_v is the amplifier open loop gain, R_1 is the feedback resistor (see Figure 16), C_1 is the feedback capacitance, and s is the Laplace variable. For an ideal operational amplifier, this reduces to:

$$\frac{V_o}{I_i} = \frac{-R_1}{(1+sR_1C_1)} \qquad [\text{Ohms}]$$

This response is flat in the passband and exhibits a single pole rolloff at $1/R_1C_1$. However, the noise gain for the amplifier is given by the reciprocal of the feedback factor as:

$$\text{Noise Gain} = 1+\frac{R_1(1+sR_dC_d)}{R_d(1+sR_1C_1)} \qquad [\text{V V}^{-1}]$$

where R_d is the detector resistance, and C_d is the detector capacitance. At low frequencies this reduces to unity because typically $R_d >> R_1$. However, note that for the case where background compensation is implemented as described in Figure 14, the compensation resistor R_5 is now in paralleled with R_d. This causes high noise gain since typically $R_5 << R_1$. At high frequencies, the noise gain reduces to:

$$\text{Noise Gain} = 1+\frac{C_d}{C_1} \qquad [\text{V V}^{-1}]$$

The ideal situation is to operate at the transition point between being feedback resistor noise limited and amplifier voltage noise limited. Below this point, increasing R_1 results in an improvement in the signal-to-noise ratio (SNR) of the amplifier because signal gain is directly proportional to R_1 and noise is proportional to $R_1^{1/2}$. Above this point, stability problems due to the large detector and amplifier input capacitances cause the SNR to degrade. The problem, however, is that in order to increase R_1, C_1 needs to decrease to preserve the amplifier bandwidth, which subsequently increases the high frequency peaking in the noise gain, as illustrated by the equation above, and decreases the stability of the amplifier. A detailed discussion of this phenomena appears in two application notes from Burr-Brown[39,40].

The detector chosen for this design is the EG&G C30902S-TC APD, which has a C_d = 2 pF. However, the common mode input capacitance of the OPA637 preamplifier is 7 pF, which dominates the detector capacitance in the noise gain of the system. The model shows that a preamplifier bandwidth of 412 kHz and an input referred noise level of 518 fA/Hz$^{1/2}$ can be obtained using R_1 = 193 kΩ and C_1 = 2 pF. This results in the preamplifier having 14.8 dB of excess noise at high frequencies. Averaging 22 temporal samples (described below) will provide an SNR improvement of 4.7, yielding an overall noise density of 111 fA/Hz$^{1/2}$, close to the desired 100 fA/Hz$^{1/2}$. While the preamplifier is optimized for the EG&G C30902S-TC APD, the Preamplifier board will physically accommodate other photodiodes (C30956, C30956-TC, C30954, C30902S) if modifications are made to the gain and compensation of the amplifier. In addition, the Preamplifier board is designed to accommodate conventional amplifiers as well as most Comlinear current feedback amplifiers. Thus, the same board design can be used for

higher bandwidth systems in the future. Background compensation is provided for, but is not implemented on the first design due to the low background estimates. An additional model was developed to assist in the design of a 4th order Bessel anti-aliasing filter using standard filter design techniques.

The signal from the preamplifier is routed to the Signal Conditioning board and applied to an inverting amplifier which scales the maximum signal to the full scale range of the analog-to-digital converter (ADC). This amplifier has a signal gain of ~-2.88 V/V and a bandwidth of 1 MHz. This is followed by a fourth order Bessel low-pass anti-aliasing filter with a gain of 1 V/V and a critical frequency of 350 kHz, realized using two 2nd order stages implemented in as infinite gain multiple feedback configuration with individual stage gains of -1 V/V. The output of the filter is applied to two summing amplifiers, one unity gain and the other with a gain of 16V/V, both with bandwidths of 1 MHz. Both amplifiers contribute an offset of -2V to the signal to bring them into the range of the ADC, and are clamped to prevent saturation. These amplifiers drive two SPT7920 12-bit, 10 MHz ADC's operating synchronously to yield 12-bit precision and 16-bit dynamic range in the system. The overall bandwidth of the front-end (including the preamplifier) is 320 kHz, and the signal is attenuated 100 dB at the 5 MHz Nyquist frequency. It will be necessary to sum 22 temporal samples in software to produce the desired 330 m range bins.

Also included on the Signal Conditioning board is the circuitry associated with synchronizing the laser and receiver electronics and integrating the laser output pulse to determine the pulse energy. A photodiode located in the Laser Subsystem will be used to monitor a portion of the laser pulse. The same PC board used for the receiver APD preamplifier is used for the monitor photodiode. The rising edge of the photodiode signal is used to trigger the data acquisition process. An integrator will be used to measure the pulse energy and a separate 8-bit ADC is used to convert the information for use in the processing algorithms.

In addition to the Preamplifier and Signal Conditioning boards, an Interface/Control board, State-of-Health (SOH) board, and Motherboard were developed. Figure 17 shows an overall system block diagram including the division of functions between the various cards in the system. The Interface/Control board provides the control signals necessary to control the data acquisition process, read out the SOH data, buffer the receiver data, and transfer the data to the computer for processing and display. The SOH board contains the thermoelectric cooler (TEC) control circuitry, filters for the APD bias, and the ADC for the analog SOH monitors. One analog monitor voltage will be read out each measurement cycle, permitting all monitors to be read nearly twice a second. The Motherboard provides for power distribution and interconnection between the Interface/Control, SOH, and Signal Conditioning boards. The system is powered by commercial power supplies which provide +5V digital, $\pm$15V analog, variable APD bias (~400V), and 120 VAC heater power

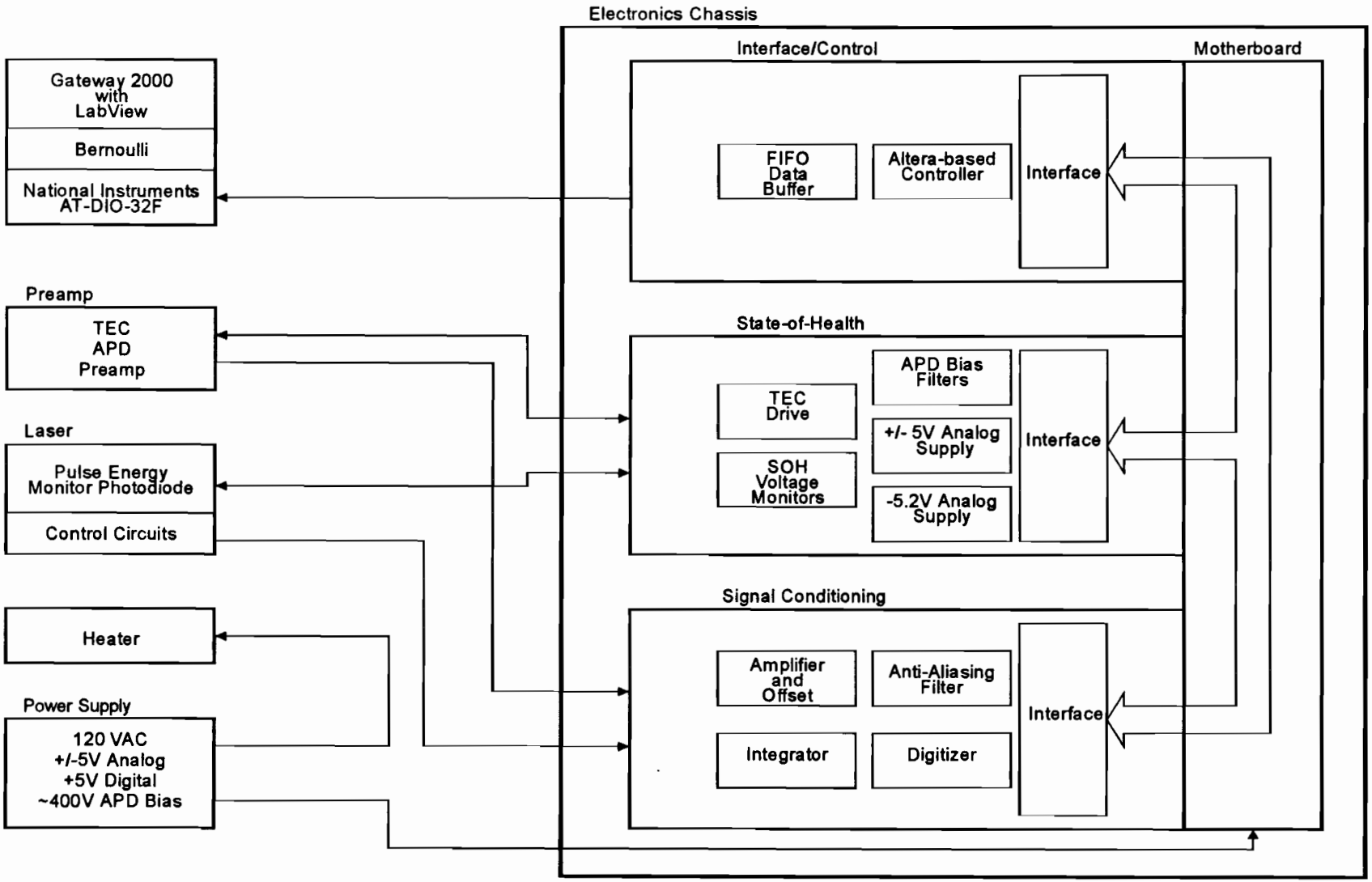

Figure 17. Ground-Based Water Vapor DIAL Demonstration System Electronics Configuration.

Physically, the Preamplifier board mounts to the rear of the telescope, along with the filter heater. The Signal Conditioning board, Interface/Control board, and State-of-Health board are packaged in the Electronics Chassis. The Electronics Chassis sits near the telescope with a compartment for the power supplies under the chassis. The cabling from the Preamplifier to the Signal Conditioning board is less than 12 inches. The computer is located within 1 m of the Electronics Chassis.

Data Acquisition System

An important part of this effort is the computer system and data acquisition, processing, and display software which is being developed under National Instruments LabView© environment for a 486/33 PC-compatible platform. The Electronics Chassis interfaces to the computer system via a parallel digital I/O card. The LabView© software is responsible for acquiring the mission and SOH data, performing the computations necessary to implement a Backscatter or DIAL configuration, displaying the results, and logging the raw and processed data to nonvolatile storage for post-processing and analysis. SOH monitors include supply voltages, reference voltages, avalanche photodiode (APD) bias, and thermoelectric cooler (TEC) temperature. One SOH value is read each measurement cycle (every 40 ms).

A measurement cycle consists of profiling one λ_{on} and one λ_{off}. Based on the modeling, 16 range bins per wavelength will be measured, starting 2.2 μs (330 m) after the laser fires. The first data point in each profile will be a measure of the laser output pulse energy. Because of the oversampling described above, there will be 22 samples per range bin (100 ns per sample), thus yielding 352 samples per wavelength ending 37.4 μs after the laser fires. It is assumed that the λ_{off} pulse will follow within 200 μs of λ_{on}. Thus, a measurement will produce 706 samples in approximately 275 μs, leaving 39.725 ms between acquisitions for the remainder of the data processing functions.

Once the data is transferred from the lidar electronics to the computer, there are a number of functions that need to be implemented to obtain water vapor measurements. First, given that the transfer function of the front-end analog electronics will be well characterized, the option of deconvolving the transfer function of the front-end electronics will be provided. Next, blocks of 22 temporal samples will be averaged to produce a single range bin value. Actually, the number of temporal samples averaged is variable to permit other applications to use varying range bin sizes (i.e. elastic backscatter). At this point we have a signal measurement cycle consisting of 16 range bins for each of λ_{on} and λ_{off}. This measurement is then averaged with data from other measurement cycles in order to reduce the DIAL error. The current baseline is to average for 100 seconds, or 2500 measurement cycles.

The final calculation is to determine the concentration of water vapor in each range bin. This is computed using the DIAL equation:

$$n = \frac{1}{2\Delta\sigma\Delta R} \ln\left(\frac{S(\lambda_{on}, R_1)\, S(\lambda_{off}, R_2)}{S(\lambda_{on}, R_2)\, S(\lambda_{off}, R_1)}\right) \qquad \text{[molecules m}^{-3}\text{]}$$

where n is the water vapor concentration, $S(\lambda_{on}, R_x)$ is the return signal from λ_{on} at altitude R_x, $S(\lambda_{off}, R_x)$ is the return signal from λ_{off} at altitude R_x, ΔR is the range bin size ($\Delta R = R_2 - R_1$), and $\Delta\sigma$ is the differential absorption cross section. In this case, $S(\lambda_{on}, R_x)$ and $S(\lambda_{off}, R_x)$ are the averaged range profiles described above. If the system is operated in elastic backscatter mode, the calculation becomes:

$$\beta(\lambda, R) = \frac{S(\lambda, R) h\, \nu (R_{LIDAR} - R)^2}{E\, \eta(\lambda) G A_0\, \tau_0(\lambda)\, \Delta R (\tau_{atm}(\lambda, R))^2} \qquad \text{[photoelectrons]}$$

where $\beta(\lambda, R)$ is the volumetric backscatter coefficient at wavelength λ and altitude R, $S(\lambda,R)$ is the backscattered return signal at wavelength λ and altitude R, h is Planck's constant, ν is the laser frequency, R_{LIDAR} is the altitude of the DIAL system, R is the altitude being measured, E is the laser pulse energy, $\eta(\lambda)$ is the quantum efficiency of the detector at the wavelength λ, G is the gain of the detector, A_0 is the area of the receiver telescope, $\tau_0(\lambda)$ is the transmission of the collecting optics at the wavelength λ, ΔR is the range bin size (vertical resolution of the DIAL system), and $\tau_{atm}(\lambda,R)$ is the atmospheric transmission at wavelength λ and altitude R.

The software is being designed to accommodate a variety of outputs. In an operational mode, it will be capable of displaying the computed concentrations (or backscatter coefficients) in a 2D (signal shot), 3D (concentration profile vs. time), or pseudo-3D (e.g. false color concentration vs. time) and log the concentrations to disk along with the oversampled, preprocessed (raw) data. Given the low data rate from the system, (35.3 KBPS) this should not be a problem. SOH data will also be incorporated into the display, with alarm limits to signal error conditions.

Estimated Performance

The parameters assumed for the ground-based water vapor DIAL demonstration system are shown in Table 10. Originally we had planned to use water vapor lines in the 727-nm region because they were well characterized by NASA researchers for the LASE program. However, we were having difficulty finding laser diodes to injection seed the Ti:sapphire ring laser at this wavelength. We learned that NASA was also having this same problem and had done some further research into characterizing lines in the 817-nm region. It was for these reasons that we decided to switch to lines in the 817-nm region for our water vapor DIAL demonstration system. This was easily accomplished by purchasing diodes to injection seed in this wavelength region, laser mirrors optimized for this wavelength region, and a narrow band optical filter for this region. The Ti:sapphire laser actually operates better in the 817-nm region which is close to its peak gain, and we will be able to obtain a very efficient system.

Table 10: Ground-Based Water Vapor DIAL Demonstration System Parameters

Parameters	Value
Transmitter:	
Ti:sapphire Laser	
Laser Wavelength	~ 817 nm
Laser Energy	25 mJ per pulse
Laser Beam Quality	2 X Diffraction Limited
Laser Divergence (FWHM)	0.05 mrad
DIAL Measurements Per Second	20
Receiver:	
Collecting Aperture Diameter	0.35 m
Full Field of View	0.128 mrad
Filter Bandwidth (FWHM)	1.0 nm
Optical Transmittance (Total)	37.8%
Detector Si APD at - 5 °C (C30902S)	
Quantum Efficiency	74%
Gain	100
Noise Equivalent Power	8.06×10^{-15} W/Hz$^{1/2}$
Excess Noise Factor	3.95
Amplifier Noise Current	1×10^{-13} A/Hz$^{1/2}$
Other:	
Solar Spectral Radiance	250 W/(m^2 μm sr)
Nighttime Background Radiance	.0025 W/(m^2 μm sr)
Ground Altitude	1.64 km
Vertical Resolution	330 m
Shots Averaged for both on-line and off-line signals	2000 (100 second averaging)

The demonstration system is planned to be operated in Albuquerque, NM which has a fairly dry desert climate. The rainy season is in the summer, and originally the DIAL was planned to be operated during this time. The estimated performance of the ground-based water vapor DIAL demonstration system is listed in Table 11. Our performance model predicts that we can profile water vapor in the atmosphere from 2.3 to 6 km with a DIAL measurement error of ≤ 10% and from 2.3 to 6.6 km with a DIAL measurement error of ≤ 20% in the daytime. At night, we can profile water vapor from 2.3 to 6.3 km with a DIAL measurement error of ≤ 10% and from 2.3 to 7 km with a DIAL measurement error of ≤ 20%. These results are based on a Mid-Latitude Summer model for the molecular absorption and scattering, and a rural 60-km visibility aerosol

Table 11: Estimated Performance for the Ground-Based Water Vapor DIAL Demonstration System; Mid-latitude Summer Model; Albedo = 0.3

Wavelength	Peak Absorption Cross section	Background	Range Profiled DIAL Error ≤ 10%	Range Profiled DIAL Error ≤ 20%
816.9384 nm	2.58E-27 m^2	Day/Earth	2.3 - 6.0 km	2.3 - 6.6 km
816.9384 nm	2.58e-27 m^2	Night/Earth	2.3 - 6.3 km	2.3 - 7.0 km

model which is an appropriate model for the typical Albuquerque climate. The system can easily be tuned to operate at a slightly stronger on-line wavelength if the water vapor content is less than we have predicted.

OPO Development for Lidar

We have an on-going program at SNL aimed at making available efficient, high-peak-power, narrow-bandwidth, broadly tunable near-infrared, visible and ultraviolet sources based on optical parametric oscillators (OPO's) for remote sensing applications. Although OPO's have existed since 1965, the availability of crystals with high optical nonlinearity, damage threshold, and optical quality as well as the advent of well-behaved pump sources has only recently made possible practical operation of these devices. Our program has concentrated on the development of pulsed, narrow-bandwidth OPO's. Applications which probe sharp atomic or molecular resonances or where the OPO output is to be converted to yet a new wavelength require OPO's with narrow bandwidth (<0.1 cm^{-1}) and tunability. We are concentrating on pulsed OPO's because they are relatively easy to operate with available high-reliability pulsed sources (e.g., flashlamp or diode-pumped Q-switched Nd:YAG lasers) and because they produce the high peak power necessary for lidar on non-cooperative targets or where ranging is required. Our program covers both the fundamental research aspects of these nonlinear optical devices and the preliminary engineering of rugged fieldable sources.

An OPO is an efficient (up to 60%), broadly tunable (e.g., 0.4 to 2 μm), solid-state laser-like device pumped by coherent light. The heart of the OPO is an optical crystal which generates gain at two new frequencies ν_i ("idler" wave) and ν_s ("signal" wave) when pumped by an intense beam of light at one frequency, ν_p. This process is known as optical parametric amplification (OPA). Efficient operation requires that energy and momentum be conserved as shown graphically in Figure 18. Momentum conservation, referred to as phase matching in this context, determines the specific values of ν_i and ν_s. In practice, phase matching is achieved by taking advantage of the birefringence of these crystals. The idler and signal frequencies can be tuned by either varying the angle of propagation through the crystal or by varying the temperature of

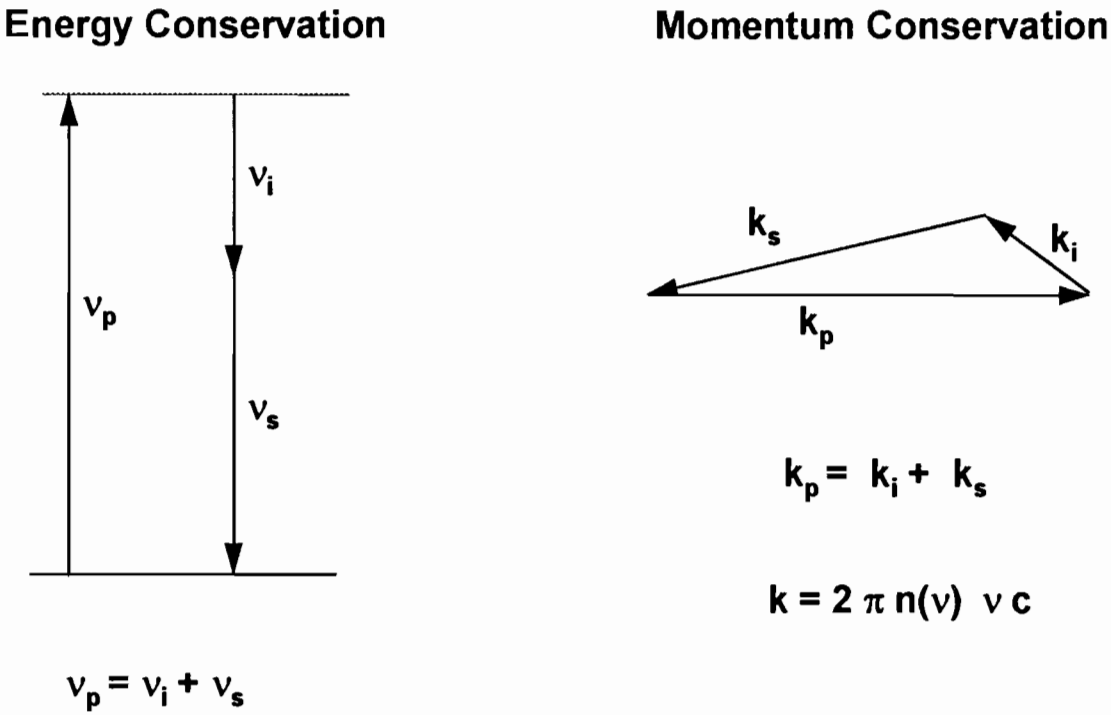

Figure 18. Graphical representation of Conservation of Energy and Momentum in the Operation of an OPO. Energy conservation requires that the sum of the idler and signal frequencies equal that of the pump, and conservation of momentum requires that the pump momentum equal the sum of the idler and signal momenta.

the crystal. Because the generation of these new frequencies is a bulk electronic phenomena not resonant with the real energy levels in the crystal, gain can be achieved over a wide range of frequencies provided that phase matching is possible. Figure 19 shows a typical example of the broad tunability possible in an OPO. This figure shows the generated wavelengths for angle-tuned phase matching in a potassium titanyl phosphate (KTP) crystal pumped by the second harmonic of the Nd:YAG laser.

Wavelengths of particular interest to the water vapor DIAL application are 727, 817, and 940 nm and are readily attainable as the signal wave from an OPO pumped by 532-nm radiation from a frequency-doubled Nd:YAG laser. Although a number of crystals will phase match in this wavelength region with 532-nm pumping (e.g. Lithium Triborate (LBO), β-Barium Borate (BBO), Lithium Niobate, Potassium Niobate, and KTP) KTP is the best choice because of its high nonlinearity, high damage threshold and modest temperature sensitivity. As with the Ti: sapphire laser, injection seeding is the preferred method of obtaining the narrow linewidth required. Experiments conducted with an injection-seeded KTP OPO showed that efficiencies on the order of 25% could be obtained with good beam quality and narrow linewidth for modest output energies of about 3-6 mJ. Scaling to higher output energies while retaining the beam quality will require novel OPO cavity designs. While we may expect advances in this performance area in the near future, current designs for a DIAL system will probably require an optical parametric amplifier (OPA) stage to obtain the desired 15-30 mJ of output. Our computer codes indicate that we can expect about 30 mJ of output for a OPA with 3 mJ of input and 100 mJ of pump.

We are investigating a KTP OPO pumped by the second harmonic of the Nd:YAG laser that could be used for DIAL on water vapor (727, 817, and 940 nm) or on hydrocarbons (in the 2-4 μm range). The signal wave is resonated in the simple three-mirror OPO ring cavity shown in Figure 20. This cavity is very similar to that used in the Ti:sapphire laser previously described. In addition to the near infrared light achievable with Ti:sapphire, this OPO also produces light in the mid-infrared. Wavelength selectivity is achieved by injection seeding the OPO with a single-frequency diode laser. Figure 21 shows typical performance from this laser. Note that efficient amplification of both waves can be achieved in a second KTP crystal with little additional complexity.

Conclusions

We have accomplished the majority of the goals for this LDRD project. We identified the critical enabling technologies (solid-state lasers, narrowband optical filters, high-performance optical detectors) for airborne or space-based lidar applications. The requirements for the lidar system were developed, and an application was chosen. Computer-based performance models were developed which permitted us to perform trade studies on various technologies and system configurations. We produced conceptual designs for airborne and space-based water vapor DIAL systems. A

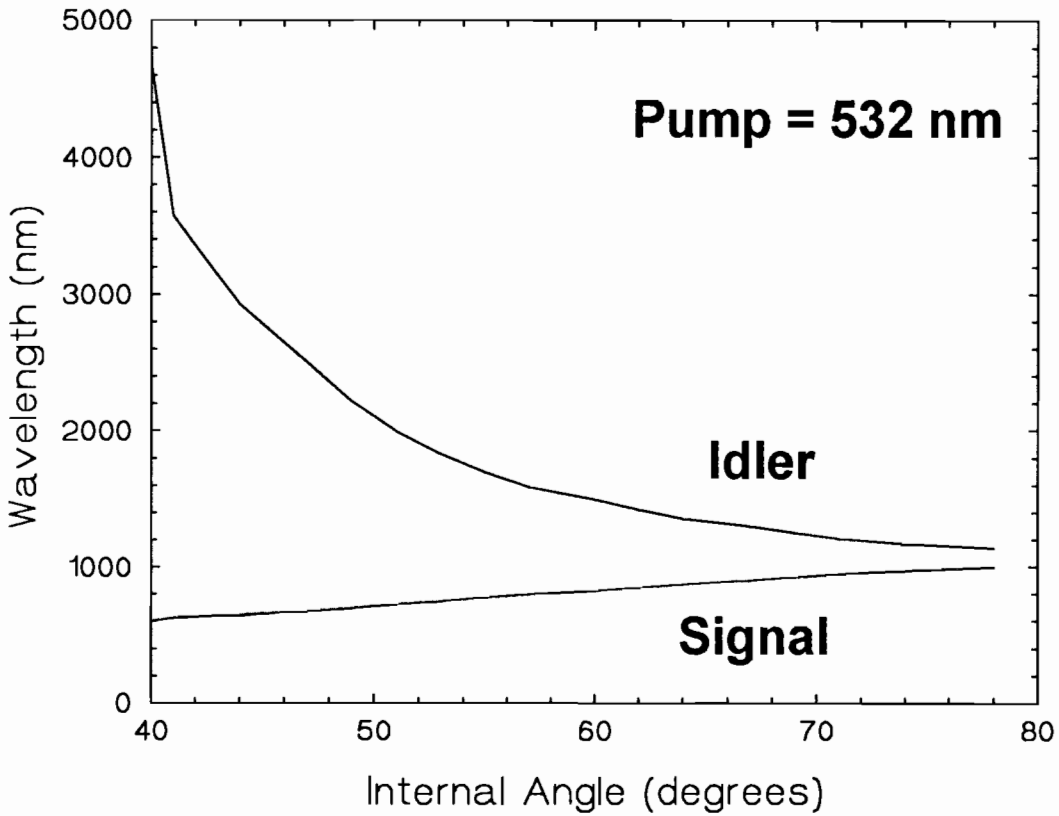

Figure 19. Generated wavelengths for angle-tuned phase matching in a potassium titanyl phosphate (KTP) crystal pumped by the second harmonic of the Nd:YAG laser. Type II angle phase matching allows idler and signal frequencies to range from about 650 nm to 4000 nm by varying the propagation angle from 40 degrees to 78 degrees.

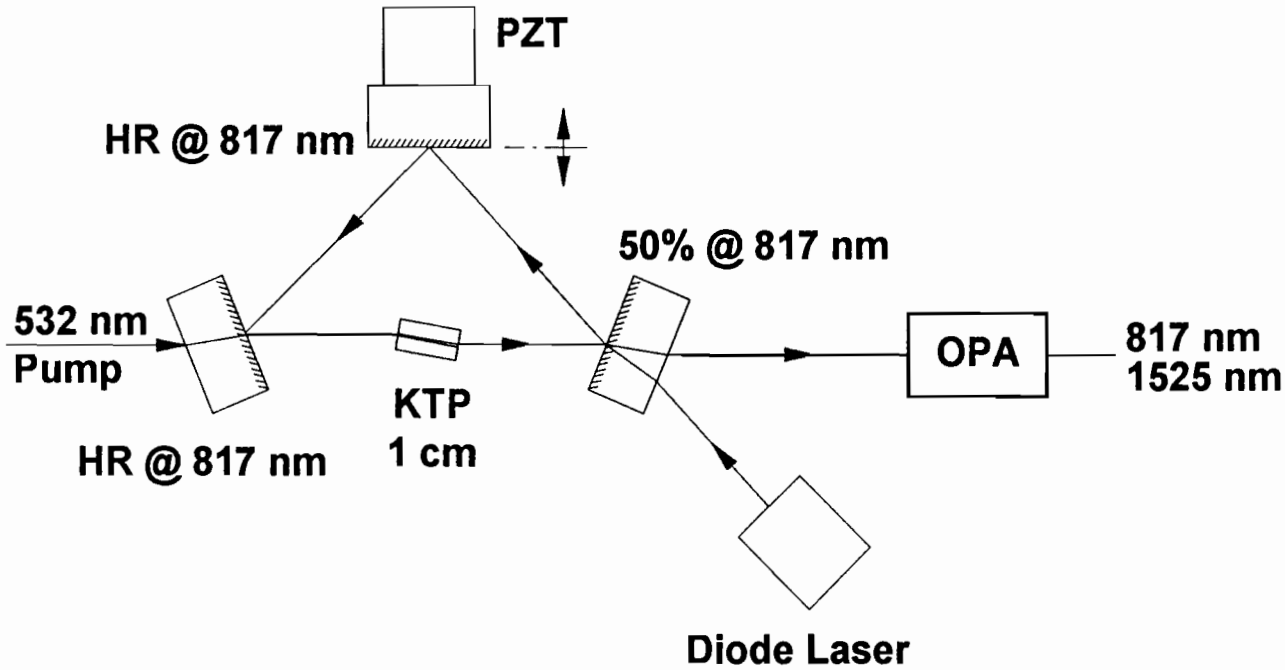

Figure 20. Schematic of a Three-Mirror OPO Ring Cavity. This three mirror ring OPO uses a KTP crystal pumped by 532 nm light from a frequency doubled Nd:YAG laser. The signal wave at 770 nm is controlled by injection seeding with a diode laser. The output signal wave is near diffraction-limited and has a near-transform-limited bandwidth. When the pump laser is injection seeded, the idler wave also has a near-transform-limited bandwidth.

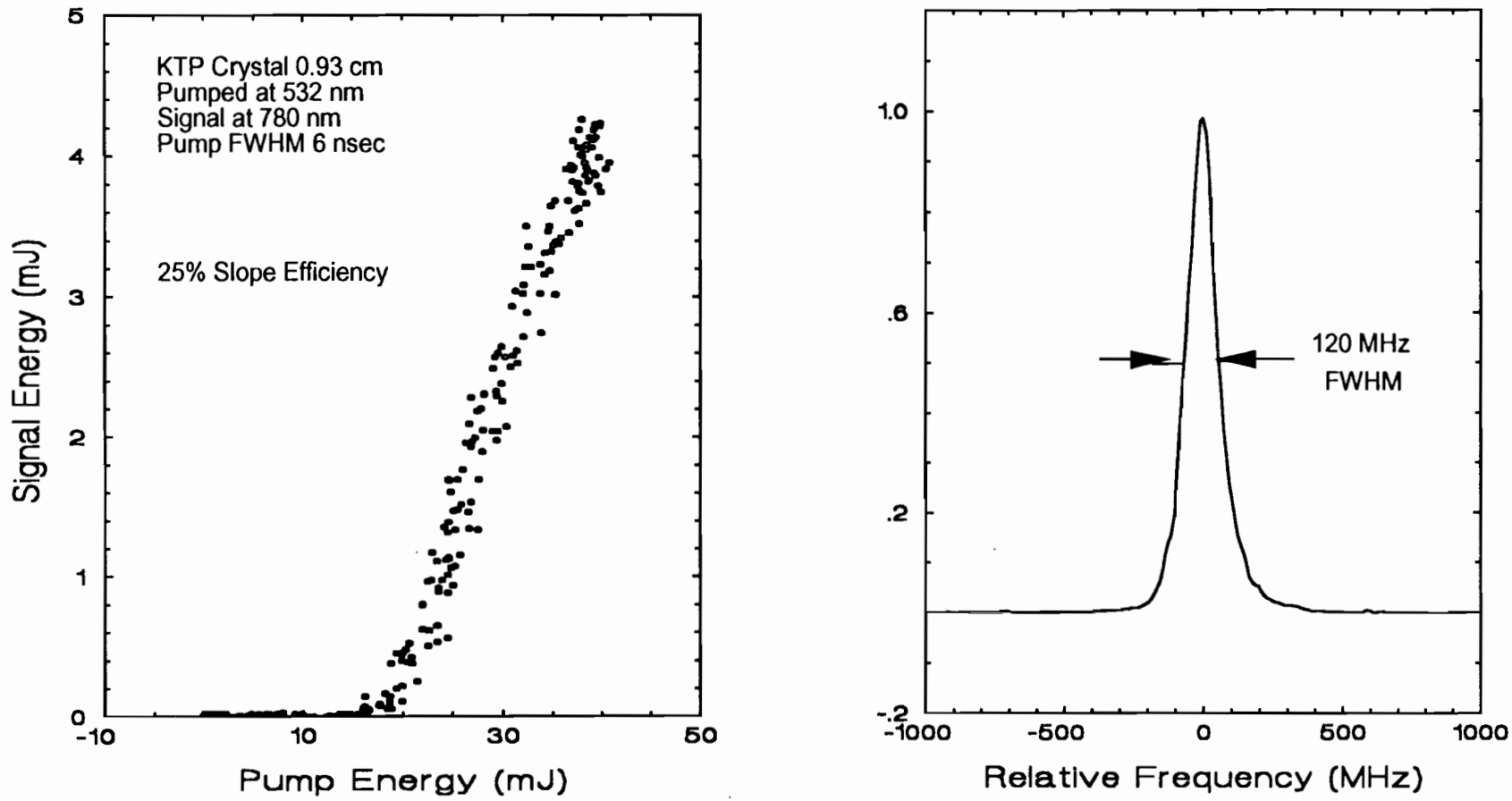

Figure 21. Typical Performance of the Three-Mirror OPO Ring Laser. The graph on the left shows the output signal energy versus pump energy and the graph on the right shows the near-transform-limited bandwidth of the signal wave.

detailed design of a ground-based water vapor DIAL demonstration system has been performed. Future work planned includes the final testing, integration, and operation of the demonstration system to prove the capability of the critical enabling technologies identified.

We have identified and advanced critical technologies for lightweight, low-power, rugged, and autonomous lidar systems. An all-solid-state Ti:sapphire ring laser has been designed which enables reliable and efficient airborne and space-based lidars. The laser will be locked to a DIAL line using a microwave frequency stabilization technique which is a novel approach to the DIAL frequency control problem. Because it relies on a synthesized r.f. frequency, this technique is very versatile and can be used for many DIAL applications. The best narrowband filter performance is obtained with interference filters for an airborne DIAL system and Fabry-Perot etalons for a space-based DIAL system. Silicon avalanche photodiodes offer the best performance for a Ti:sapphire based DIAL system. In addition, because of the care taken in the design of the electronics and data acquisition systems, it is believed that the ground-based water vapor DIAL demonstration system will yield data with a level of accuracy unmatched by current research lidar systems.

Lidar is an important tool in the future of remote sensing. Water vapor profiling is a key unfulfilled measurement requirement in determining cloud genesis. Clouds and their effects on the earth's radiation balance is the top priority of the US Global Change Research Program. Current measurement techniques that provide broad-area coverage, such as microwave and infrared sounding, do not meet the vertical resolution and measurement accuracy requirements of the climate community whereas lidar can.

Work is now underway to complete the assembly and testing of the ground-based water vapor DIAL demonstration system. This demonstration system will use the miniature Ti:sapphire laser, the R. F. frequency control system, and the receiver electronics developed under this LDRD. DIAL measurements taken with this system will prove the viability of the technologies we developed, and enable the use of miniature lidar systems for environmental monitoring, atmospheric profiling and cloud top measurements, detection of the proliferation of weapons of mass destruction, drug interdiction, and agricultural/land use.

This page intentionally left blank.

References

1. R. M. Measures, Laser Remote Sensing Fundamentals and Applications, Reprint Edition (Krieger Publishing Company, 1992)

2. C. Y. She, "Remote measurement of atmospheric parameters: new applications of physics with lasers," Contemporary Physics **31**, 247 (1990).

3. S. Ismail and E. V. Browell, "Airborne and spaceborne lidar measurements of water vapor profiles: a sensitivity analysis," Appl. Opt. **28**, 3603 (1989).

4. N. P. Barnes, M. E. Storm, P. L. Cross, and M. W. Skolaut, Jr., "Efficiency of Nd laser materials with laser diode pumping," IEEE J. Quantum Electron. **26**, 558 (1990).

5. T. Y. Fan, G. Huber, R. L. Byer, and P. Mitzscherlich, "Spectroscopy and diode laser-pumped operation of Tm:Ho:YAG," IEEE J. Quantum Electron. **24**, 924 (1988).

6. S. R. Bowman, M. J. Winings, R. C. Y. Auyeung, J. E. Tucker, S. K. Searles, and B. J. Feldman, "Laser and Spectral Properties of Cr, Tm, Ho:YAG at 2.1 μm," IEEE J. Quantum Electron. **27**, 2142 (1991).

7. T. Y. Fan, G. Huber, R. L. Byer, and P Mitzscherlich, "Continuous-wave operation at 2.1 μm of a diode-laser-pumped, Tm-sensitized Ho:$Y_3Al_5O_{12}$ laser at 300 K," Opt. Lett. **12**, 678 (1987).

8. N. Sugimoto, N. Sims, K. Chan, and D. K. Killinger, "Eye-safe 2.1-μm Ho lidar for measuring atmospheric density profiles," Opt. Lett. **15**, 302 (1990).

9. Cha, K. P. Chan, and D. K. Killinger, "Tunable 2.1-μm Ho lidar for simultaneous range-resolved measurements of atmospheric water vapor and aerosol backscatter profiles," Appl. Opt. **30**, 3938 (1991).

10. R. Targ, M. J. Kavaya, R. M. Huffaker, and R. L. Bowles, "Coherent lidar airborne windshear sensor: performance evaluation," Appl. Opt. **30**, 2013 (1991).

11. S. A. Payne, L. L. Chase, L. K. Smith, W. L. Kway, and H. Newkirk, "Laser Performance of $LiSrAlF_6:Cr^{3+}$," J. Appl. Phys. **66**, 1051 (1991).

12. R. Scheps, "Cr:$LiCaAlF_6$ laser pumped by visible laser diodes," IEEE J. Quantum Electron. **27**, 1968 (1991).

13. Eggleston et al., IEEE J Quantum Electron. **24**, 1009 (1988).

14. B. A. E. Saleh and M. C. Teich, Fundamentals of Photonics, John Wiley and Sons, Inc. N. Y. 1991. See chapter 17 (pp. 673 -692) for discussion of noise in photodetectors, and chapter 22 (pp. 907 - 910) for discussion of heterodyne detection.

15. H. Melchior et al., "Photodetectors for optical communication systems," Proceedings of the IEEE **58**, 1466 (1970).

16. R. M. Hardesty, "Coherent DIAL measurement of range-resolved water vapor concentration," Appl. Opt. **23**, 2545 (1984).

17. R. G. Frehlich and M. J. Kavaya, "Coherent laser radar performance for general atmospheric refractive turbulence," Appl. Opt. **30**, 5325 (1991).

18. M. J. Kavaya et al., "Remote wind profiling with a solid-state Nd:YAG coherent lidar system," Opt. Lett. **14**, 776 (1989).

19. M. J. Kavaya, S. W. Henderson, E. C. Russell, R. M. Huffaker, and R. G. Frehlich, "Monte Carlo computer simulations of ground-based and space-based coherent DIAL water vapor profiling," Appl. Opt. **28**, 840 (1989).

20. D. J. Dick and T. M. Shay, "Ultrahigh-noise rejection optical filter," Opt. Lett. **16**, 867 (1991).

21. Yin and T. M. Shay, "Theoretical model for a Faraday anomalous dispersion optical filter," Opt. Lett. **16**, 1617 (1991).

22. F. A. Jenkins and H. E. White, Fundamentals of Optics, Fourth edition (McGraw Hill 1976). See chapter 32 for a discussion of the resonant Faraday effect.

23. R. A. McClatchey et al., "Optical Properties of the Atmosphere," Air Force Cambridge Research Laboratories (now called the Air Force Geophysical Laboratories or AFGL), Bedford, MA Report No. AFCRL-72-0497, Third Edition (1972).

24. The Infrared Handbook, edited by W. L. Wolfe and G. J. Zissis, published by the Office of Naval Research, Arlington, VA (1985). Chapter 5 discusses atmospheric absorption.

25. E. V. Browell, T. D. Wilkerson, and T. J. Mc Ilrath, "Water vapor differential absorption lidar development and evaluation," Appl. Opt. **18**, 3474 (1979).

26. E. V. Browell, S. Ismail, and B. E. Grossman, "Temperature sensitivity of differential absorption lidar measurements of water vapor in the 720-nm region," Appl. Opt. **30**, 1517 (1991).

27. FASCODE, developed by the Air Force Geophysical Laboratory (now Phillips Laboratory's Geophysics Directorate) at Hascomb Air Force Base, is a high-spectral resolution atmospheric transmission model. A personal computer version of this code is available from Ontar Corporation, 129 University Road, Brookline, MA 02146-4532.

28 L. S. Rothman, et al., "The HITRAN database: 1986 edition," Appl. Optics **26**, 4058 (1987).

29. E. V. Browell, S. Ismail, M. P. McCormick, and T. J. Swissler, "Spaceborne lidar Systems for Measurement of Atmospheric Water Vapor and Aerosols," in Proceedings, AIAA/NASA EOS Conference, Virginia Beach, VA, Paper No. 85-2091, Oct. 8-10 (1985).

30. T. D. Raymond and A. V Smith, "Injection-seeded Ti:sapphire ring laser," Opt. Lett. **16**, 33, (1991).

31. C. E. Hamilton, "Single-frequency, Injection-seeded Ti:sapphire ring laser with high temporal precision," Opt. Lett. **17**, 728, (1992).

32. H. Patrick and C. E. Wieman, "Frequency stabilization of a diode laser using simultaneous optical feedback from a diffraction grating and a narrowband Fabry-Perot cavity," Rev. Sci. Instrum. **62**, 2593 (1991).

33. B. Dahmani, L. Hollberg and R. Drullinger, "Frequency stabilization of semiconductor lasers by resonant optical feedback," Opt. Lett. **12**, 876 (1987).

34. M. G. Boshier, D. Berkeland, E. A. Hinds, and V. Sandoghdar, "External-cavity frequency-stabilization of visible and infrared semiconductor lasers for high resolution spectroscopy," Opt. Commun. **85**, 355 (1991).

35. As of the writing of this report, two US companies fabricate and sell external cavity stabilized diode lasers. These companies are New Focus and Micracor.

36. R. G. De Voe and R. G. Brewer, "Laser frequency division and stabilization," Phys Rev A **30**, 2827 (1984).

37. R. W. P. Drever, J. L. Hall, F. V. Kowalski, J. Hough, G. M. Ford, A. J. Munley, and H. Ward, "Laser phase and frequency stabilization using an optical resonator," Appl Phys B **31**, 97 (1983).

38. The Infrared and Electro-Optical System Handbook Volume 2, Atmospheric Propagation of Radiation, edited by F. G. Smith, co-published by Infrared Information Analysis Center, ERIM and SPIE Optical Engineering Press, 167 (1993).

39. "Noise Analysis of FET Transimpedance Amplifiers," The Handbook of Linear IC Applications, Burr-Brown Corporation, 187 (1987).

40. "Photodiode Monitoring with Op Amps," The Handbook of Linear IC Applications, Burr-Brown Corporation, 192 (1987).

APPENDIX A
Mathematical Symbol Definitions and Units
(in alphabetical order)

A	Signal due to the amplifier noise power. Units: Photoelectrons.
A_o	Area of the receiver telescope (collecting optics). Units: m^2.
A_v	Amplifier open loop gain. Units: Volts per Volt ($V\ V^{-1}$)
$B(\lambda)$	Signal due to the solar background radiation at wavelength λ. Units: Photoelectrons.
B_{amp}	Bandwidth of the amplifier. Units: Hertz (Hz).
B	Electrical system bandwidth($B=\frac{1}{2t}$). Units: Hz.
c	Speed of light: 2.998×10^8 m sec^{-1}.
C_d	Detector capacitance. Units: Farads (F).
C_1	Feedback capacitance in the transimpedence amplifier. Units: F.
d	Distance between the reflectors in the Fabry-Perot etalon. Units: Centimeters (cm).
d_l	Apparent distance to the leading edge of the laser pulse. Units: Meters (m).
d_t	Apparent distance to the trailing edge of the laser pulse. Units: m.
$D(\lambda)$	Signal due to the detector noise power at wavelength λ. Units: Photoelectrons.
E	Energy of the laser(transmitter) pulse. Units: Joules (J).
E''	Ground-state rotational energy level. Units: cm^{-1}.
f_{3dB}	Required receiver integrator bandwidth. Units: Hz.
f_{laser}	Frequency of the laser pulse. Units: Hz.
F	Excess noise factor for an avalanche photodiode. Units: None.

F	Finesse of the Fabry-Perot etalon. Units: None.
FOV	Field-of-view of collecting optics. Units: Milliradian (mrad).
FSR	Free spectral range of Fabry-Perot etalon. Units: Gigahertz (GHz).
G	Internal gain of the detector. Units: None.
h	Planck's constant: 6.626×10^{-34} J sec.
I_i	Amplifier input current. Units: Amps (A).
I_{na}	Amplifier noise current. Units: A $Hz^{-1/2}$.
k	Boltzmann's constant: 1.381×10^{-34} J K^{-1}.
l	Optical length of Fabry-Perot etalon. Units: cm.
l_o	Inner scale in turbulence theory. It establishes the minimum spatial extent over which turbulence can occur. Units: cm.
L_o	Outer scale in turbulence theory. It sets the maximum spatial limit over which homogeneity can be reasonably expected. Units: m.
L_λ	Solar Spectral radiance at the top of the atmosphere at wavelength λ. Units: W m^{-2} μm^{-1} sr^{-1}.
LED	Laser energy density at the earth's surface. Units: J m^{-2}.
m	Integer order of Fabry-Perot interferometer. Units: None.
$\overline{m}$	Mean number of photoelectrons counted in resolution interval t. Units: None.
n	Molecular (water vapor) concentration. Units: molecules m^{-3}.
n	Index of refraction of the medium between the reflectors in the Fabry-Perot etalon. Units: None.
N	Number of DIAL laser shots (measurement cycles) averaged to make a measurement (determines the horizontal resolution of an airborne or space-based DIAL system). Units: None.

$N(R)$	Number density of air molecules at altitude R. Units: molecules m^{-3}.
$NEP(\lambda)$	Noise equivalent power of the detector at wavelength λ. Units: W $Hz^{-1/2}$.
P_s	Optical power of lidar return signal. Units: Watts(W).
q	Electron charge: 1.602×10^{-19} Coulombs (C).
r	Power reflectivity of the coatings for the reflectors in a Fabry-Perot etalon. Units: None.
R	Altitude (with respect to sea level) at which a lidar measurement is being made. Units: m.
R_d	Detector resistance. Units: Ohms (Ω).
R_1	Feedback resistor in the transimpedance amplifier. Units: Ω.
R_{DIAL}	Altitude (with respect to sea level) where the DIAL instrument is located. Units: m.
R_{LIDAR}	Altitude (with respect to sea level) where the lidar instrument is located. Units: m.
ΔR	Vertical resolution of the lidar instrument often referred to as the range bin ($\Delta R=2c/t$). Units: m.
ΔR_{min}	Theoretical minimum vertical resolution possible for a given lidar system. It is limited by the laser pulse width of the transmitter. Units: m.
s	Laplace variable. Units: None.
S_o	Absorption line strength measured at T_o. Units: cm $molecule^{-1}$.
S(T)	Absorption line strength. Units: cm $molecule^{-1}$.
$S(\lambda,R)$	lidar backscattered return signal at wavelength λ and altitude R. Units: Photoelectrons.
SNR	Signal-to-noise ratio. Units: None.

t	Time interval over which the lidar measurement is performed. Units: Seconds (sec.).
t_1	Time in which we observe the instantaneous backscattered return signal. Units: sec.
T	Temperature. Units: Kelvin (K).
T_o	Temperature constant: 296 K.
V_o	Amplifier output voltage. Units: V.
α	Thermal expansion coefficient. Units: cm cm^{-1} K^{-1}.
$\beta(\lambda,R)$	Total volumetric backscatter coefficient at wavelength λ and altitude R. Units: m^{-1} sr^{-1}.
$\beta_{Aerosol}(\lambda,R)$	Volumetric backscatter coefficient due to aerosol scattering at wavelength λ and altitude R. Units: m^{-1} sr^{-1}.
$\beta_{Rayleigh}(\lambda,R)$	Volumetric backscatter coefficient due to Rayleigh (molecular) scattering at wavelength λ and altitude R. Units: m^{-1} sr^{-1}.
$\frac{\partial d}{\partial T}$	Partial differential of the Fabry-Perot etalon spacing with respect to temperature. Units: cm K^{-1}.
$\frac{\partial n}{\partial T}$	Partial differential of the refractive index of the medium between the reflectors in the Fabry-Perot etalon with respect to temperature. Units: K^{-1}.
$\frac{\partial \nu}{\partial T}$	Partial differential of the optical frequency of the laser with respect to temperature. Units: Hz K^{-1}.
η	Detector quantum efficiency. Units: electrons $photon^{-1}$.
$\eta(\lambda)$	Detector quantum efficiency at wavelength λ. Units: electrons $photon^{-1}$.
θ_{FWHM}	Laser beam divergence measured at full width half maximum. Units: mrad.

$\kappa(\lambda,R)$	Atmospheric attenuation coefficient at wavelength λ and altitude R. Units: m^{-1}.
λ	Wavelength of light. Units: Microns (μm).
$\Delta\lambda$	Wavelength bandwidth of solar rejection filter. Units: μm.
ν	Optical frequency of the laser ($\nu=c/\lambda$). Units: Hz.
ν_i	Idler wave frequency generated by an OPO. Units: Hz.
ν_p	Frequency of laser used to pump OPO. Units: Hz.
ν_s	Signal wave frequency generated by an OPO. Units Hz.
π	3.1415927. Units: None.
ρ_e	Earth's albedo. Units: None.
σ_q	Circuit noise variance. Units: None.
$\sigma(\lambda)$	Backscatter cross section for Rayleigh scattering. Units: $m^2\ sr^{-1}$.
$\Delta\sigma$	Differential absorption cross section of water vapor line used to make the measurement ($\Delta\sigma=\sigma_{on}-\sigma_{off}$). Units: m^{-2}.
τ	Temporal FWHM pulse width of the laser transmitter. Units: sec.
$\tau_o(\lambda)$	Transmission of the collecting optics at wavelength λ. Units: None.
$\tau_{atm}(\lambda,R)$	Atmospheric transmission at wavelength λ between R_{DIAL} or R_{LIDAR} and R. Units: None.
ω_1	Frequency of the microwave oscillator. Units: GHz.
ω_2	Frequency of the r.f. oscillator. Units: Megahertz (MHz).

This page intentionally left blank.

APPENDIX B
Abbreviations and Acronyms
(in alphabetical order)

AC	Alternating current
ADC	Analog-to-digital converter
ADOF	Anomalous dispersion optical filter
AFGL	Air Force Geophysics Laboratory
ANSI	American National Standards Institute
APD	Avalanche photodiode
BBO	β-Barium Borate
CALIOPE	Chemical analysis by laser interrogation of proliferation effluents
DC	Direct current
DIAL	Differential absorption lidar
FADOF	Faraday anomalous dispersion optical filter
FOV	Field-of view
FSR	Free spectral range
FWHM	Full-width at half maximum
HEMPT	High electron mobility phototransistor
HEMT	High electron mobility transistor
KTP	Potassium Titanyl Phosphate
LASA	Lidar Atmospheric Sounder and Altimeter
LASE	Lidar Atmospheric Sensing Experiment

LBO	Lithium Triborate
LDRD	Laboratory directed research and development
LED	Laser energy density
LIDAR	Light detection and ranging
LLNL	Lawrence Livermore National Laboratory
MPE	Maximum permissible exposure
NASA	National Aeronautics and Space Administration
NEP	Noise equivalent power
OPA	Optical parametric amplification
OPO	Optical parametric oscillator
PC	Printed circuit
PMT	Photomultiplier tube
PZT	Piezoelectric transducer
RADAR	Radio detection and ranging
SADOF	Stark anomalous dispersion optical filter
SOH	State-of-Health
SNL	Sandia National Laboratory
SNR	Signal-to-noise ratio
STP	Standard temperature and pressure
TEC	Thermoelectric cooler
TIA	Transimpedance amplifier
UAV	Unmanned Aerospace-vehicle
UV	Ultraviolet

VAC	Volts AC
YAG	Yttrium Aluminum Garnet

This page intentionally left blank.

APPENDIX C
Lidar Applications

Wind

Doppler Lidar applications

1. CO_2 lasers for Doppler wind lidar applications
2. Application of Doppler radar and lidar to diagnose phenomenon
3. Accuracy of wind measurements using airborne and infrared Doppler lidar
4. Mapping global winds with satellite borne Doppler lidar
5. Doppler lidar for measuring winds in the atmosphere
6. Doppler lidar observations of a downslope windstorm
7. Dual-Doppler lidar measurement of winds in the JAWS experiment
8. Doppler lidar observations of airflow in the Grand Canyon

Turbulence

9. Refractive turbulence profiles by high-resolution lidar
10. Measurements with lidar
11. lidar measurements of the entrainment zone and the turbulent kinetic energy budget of the atmospheric mixed layer
12. Lidar observations of the daily variation of boundary layer winds and turbulence
13. Lidar-generated artificial guidestars for atmospheric turbulence compensation

Wind Measurement in General

14. Measurement of winds, backscatter, and return signal properties using pulsed coherent lidar
15. Wind profiling by a conical-scanning time-correlation lidar
16. Coherent lidar wind measurements for the space station base using 1.5 m all-reflective optics
17. Ascent guidance algorithm using lidar wind measurements
18. Monitoring Alpine Valley wind circulation by airborne lidar
19. Daytime lidar measurements of tidal winds in the mesospheric sodium layer at Urbana, Illinois

Wind Shear and Airspeed

20. CO_2 lidar for low-level wind shear detection and airspeed
21. Coherent lidar airborne wind shear sensor--performance evaluation
22. Infrared lidar wind shear detection for commercial aircraft and the edge technique a new method for atmospheric wind measurement
23. Derivation of atmospheric extinction profiles and wind speed over the ocean from a satellite lidar

Vegetation

24. Vegetation remote-sensing--a new field for lidar applications
25. Floodplain mapping based on a lidar derived data set

Transport Processes

26. Airborne downlooking lidar studies of intermediate and long range atmospheric transport processes

Clouds

General

27. Lidar observations of cloud top structure and scattering polarization
28. An analysis of lidar observations of polar stratospheric clouds

Cirrus

29. Lidar observations of cirrus cloud parameters
30. The use of an airborne lidar for mapping cirrus clouds in FIRE, phase 2
31. Airborne lidar/radiometric measurements of cirrus cloud parameters and their application to LOWTRAN radiance evaluations
32. Determination of particle effective radii using radar and lidar scattering

Marine Stratus

33. Lidar determinations of extinction in stratus clouds
34. Airborne lidar observations of Arctic polar stratospheric clouds
35. Hydrogen Chloride measurements with a DAS lidar in the marine atmosphere
36. Multiple scattering depolarization in marine stratus clouds; lidar experiments

Ocean

37. Lidar cross section for light scattering by ocean water
38. Lidar bathymetry
39. Lidar for the remote measurement of subsurface ocean parameters
40. Estimate of maximum penetration depth of lidar in coastal water of the China Sea
41. Lidar applications in the remote sensing of ocean properties
42. Time-resolved fluorosensor for sea pollution detection
43. Application of the NASA airborne oceanographic lidar to the mapping of chlorophyll and other organic pigments

Water Vapor

44. DIAL and Raman lidar for water vapor profile measurements
45. Measurement of atmospheric water vapor using DIAL
46. Airborne DIAL system for water vapor investigations
47. Spaceborne lidar and Raman lidar systems for measurement of atmospheric water vapor and aerosols
48. Lidar monitoring of the tropospheric water vapor mixing ratio

Macroscopic Characteristics of Atmosphere

Pressure, Temperature, and Density

49. Two-frequency lidar technique for mesospheric Na temperature measurement
50. Lidar system for measuring atmospheric temperature and pressure
51. DIAL measurements of atmospheric temperature and pressure profiles
52. Lidar techniques for temperature and humidity profiles in the atmosphere
53. DIAL in space for temperature and humidity profiles in the atmosphere
54. Application of lidar to atmospheric measurement of density and temperature
55. On the measurement of atmospheric density using DIAL in the O_2 A-band (770 nm)

Aerosols, Particulates, and Gases

General

56. Lidar probing of the atmospheric aerosol
57. Lidar applications to aerosols and particles

Aerosol Concentrations and Profiles

58. Quantitative determination of aerosol concentrations by lidar
59. Quantitative determination of aerosol optical parameters from monostatic lidar measurements
60. Rapid acquisition lidar system for aerial spray diagnostics
61. Lidar mapping of a mixture of aerosol concentrations in the atmosphere
62. Spectrochemical lidar for analyzing the elemental composition of the atmospheric aerosol
63. Lidar instrument to measure H_2O and aerosol profiles
64. Some results of aerosol lidar measurements and their relationship to meteorological parameters
65. Visibility and aerosol measurement by diode-laser random-modulation cw lidar

Particulates

66. Remote sensing of atmospheric gases and particulates by lidar
67. Particulate extinction and backscatter properties determined from lidar measurements

Scattering

68. A high-resolution lidar-Thomson scattering diagnostic for JET
69. Lidar investigations of hydrosols: notes on the determination of scattering matrix elements
70. Lidar measured vertical atmospheric scattering profiles
71. High spectral resolution lidar to measure optical scattering properties of atmospheric aerosols. II: calibration and data analysis
72. Lidar observations of anomalous scattering in the atmosphere

Aerosols in the Stratosphere and Troposphere

73. Application of lidar to stratospheric aerosol studies
74. Infrared lidar measurements of crustal aerosol mixing in the troposphere
75. Airborne DIAL system for remote tropospheric sensing: the spatial distribution of gases and aerosols are measured
76. Lidar sensing of aerosols, clouds, and ozone in the troposphere and stratosphere
77. Remote sounding of aerosols in the lower atmosphere using a bistatic cw He-Ne laser
78. Boundary-layer sounding of humidity and aerosols using Raman lidar
79. Study of atmospheric aerosols in a terrain-induced nocturnal boundary layer using bistatic lidar

Aerosols due to Volcanic Eruptions

80. Volcanic eruptions and the increases in the stratospheric aerosol content - lidar measurements from 1982 to 1986
81. Lidar measurements of the El Chicon aerosols from 1982 to 1983
82. Lidar measurements of Mount St. Helens effluents

Gases

83. Improved Raman lidar system for the remote measurement of natural gas releases into the atmosphere
84. Gas dispersion measurements using a mobile Raman lidar system

Weather

85. Range measurements of humidity by a parametric light oscillator lidar
86. Lidar study of storm tops
87. Lidar indication of artificial dissipation of supercooled fogs
88. Demonstration of a high pulse rate lidar for studying airflow
89. Details of colliding thunderstorm outflows as observed by Doppler lidar

Pollution

Detection and Monitoring

90. Laser lidar system for measurement of atmospheric pollution
91. IROE-lidar remote sensing of the environment
92. Investigation of episodic air quality using airborne lidar
93. Air pollution measurement by lidar
94. NO_2 - SO_2 DIAL for routine emission and imission measurements
95. Lidar remote measurements of space shuttle ground cloud emissions
96. Estimation of pollutant transport and concentration distributions over complex terrain of Southern California using airborne lidar
97. Lidar evaluation of smoke and dust clouds

Plumes

98. Lidar applications: plume tracking and modeling
99. Lidar observations of the plumes of incineration ships

100. Investigation of a 1000 mw smoke plume by means of a 1.064 μm lidar II. Determination of diffusion characteristics of the plume particles
101. Lidar remote sensing techniques for regulatory compliance of plume opacity
102. Utilization of Aerosol lidar for the measurement of aerosols in the atmospheric boundary layer: application to plume investigation
103. Three-wavelength lidar method to measure mass concentration in an unknown pollutant cloud

Detection of Compounds in the Atmosphere

Measurement and Detection of Sulfur Dioxide, Nitrogen Dioxide, and Ozone

104. Path lidar for measuring the concentration of SO_2 in the atmosphere
105. NO_2 detection in the atmosphere using DIAL
106. Mobile DIAL for range-resolved measurements of SO_2, O_3, and NO_2
107. Lidar measurements of SO_2 and O_3 in the boundary layer in the 1983 FOS Berre Campaign
108. Solar-blind DIAL for ozone detection
109. Stratospheric ozone measurements using a ground based, high power lidar
110. Lidar method of measurement of atmospheric extinction and ozone
111. Ozone and Aerosol Measurements with an airborne lidar and DIAL systems

Detection of Mercury

112. Lidar measurements of atmospheric Mercury
113. Atmospheric atomic Hg monitoring and mapping using DIAL techniques

The Sodium Layer

114. Lidar observations of the mesospheric sodium layer
115. Lidar observations of the nighttime sodium layer at 33 deg N

Detection of Miscellaneous Compounds

116. Laser remote sensing of Hydrazine, MMH, and UDMH, using a CO_2 DIAL
117. Iron atom densities in the polar mesosphere from lidar observations
118. Shuttle lidar resonance fluorescence investigations - 1. Analysis of Na and K measurements
119. Shuttle lidar resonance fluorescence investigations - 2. Analysis of thermospheric MG^{**} plus measurements
120. Resonant lidar detection of Ca and Ca^{**} plus in the upper atmosphere
121. Gas correlation lidar for Methane detection

The Atmosphere in General

Atmospheric Probing and Measurements

122. Spaceborne lidar investigations of the atmosphere
123. Coherent CO_2 lidar systems for remote atmospheric measurement

124. Lidar techniques for measuring multiple fluorescent tracers of atmospheric motions
125. The use of lidar to obtain three-dimensional refraction data (atmospheric probing)

Tropospheric, Stratospheric, and Planetary Boundary Layer Studies

126. Lidar measurements of tropospheric parameters
127. Remote measurement of tropospheric and stratospheric winds by ground based lidar
128. Lidar observations of the planetary boundary layer

Sounding of the Atmosphere

129. Some results of lidar soundings of the atmosphere along slant paths
130. Lidar measurements of slant visual range

Transmittance and extinction coefficients of the atmosphere

131. Determination of atmospheric transmittance in tunnel by slope method using lidar
132. Automated lidar system for determining atmospheric extinction coefficient

General Topics

133. Spaceborne lidar applications to meteorology and environmental studies
134. Lidar applications to the geochemical field
135. Sodium resonance fluorescence lidar applications in atmospheric science and astronomy
136. Applications of laser and lidar spectroscopy to meteorological remote sensing

Miscellaneous

137. Application of upconversion detection to pulsed CO_2 lidar
138. Lidar detection of metallic species at the mesopause level
139. Gross-merchantable timber volume estimation using an airborne lidar system
140. Vertical structure and mapping of Arctic haze observed by lidar
141. Lidar observations and modeling of cold air outbreaks during Masex and Gale
142. Lidar measurements of thermal structure
143. Design of a spaceborne lidar for measurements from operational satellites
144. Lidar studies of polarization anisotropy in multiple backscattering
145. Lidar techniques for search and rescue
146. Elastic backscattering lidar system for atmospheric measurements in Antarctica
147. Lidar measurements of atmospheric trace constituents and physical parameters at the Observatorie de Haute Provence

148. Lidar correlation measurement of the atmospheric drift velocity
149. Lidar profiling of thermodynamic properties of the atmosphere
150. Detecting the conditions of the ultrashort wave waveguide propagation over the sea by means of lidar
151. Scanning hydrographic operational airborne lidar survey system
152. Heterodyne lidar for wire detection an obstacle warning
153. Atmospheric moisture structure revealed by Raman lidar
154. Coherent laser radar at 1064 nm using Nd:YAG lasers

This page intentionally left blank.

APPENDIX D
AFGL Standard Atmospheric Parameters

Figure D-1 shows a composite plot of the water vapor molecular number density as a function of altitude for the five AFGL standard atmospheres. Note that for all of the models, the water vapor density decreases over 3 orders of magnitude from sea level to 14 km. Also, at sea level, the water vapor density for the standard tropical atmosphere is an order of magnitude greater than for the subarctic winter atmosphere. Figure D-2 shows a composite plot of the temperature as a function of altitude for the five AFGL standard atmospheres. It is worth emphasizing that these model atmospheres represent average conditions, and that the actual atmospheric conditions that a DIAL may attempt to measure may vary by several orders of magnitude from these standard atmospheres. Nevertheless, these standard atmospheres are useful input data for simulations, and the results of simulations can be compared to those of other workers in the field who have used these same data sets.

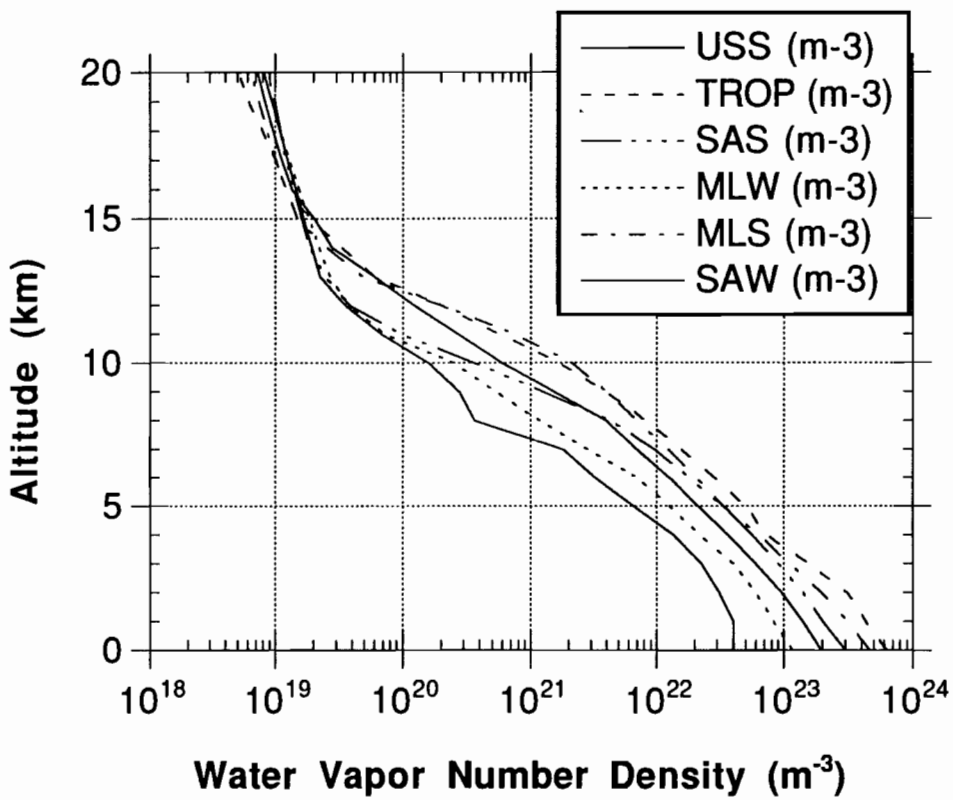

Figure D-1. Composite Plot of the Water Vapor Number Density as a function of Altitude for the five AFGL Standard Atmospheres.

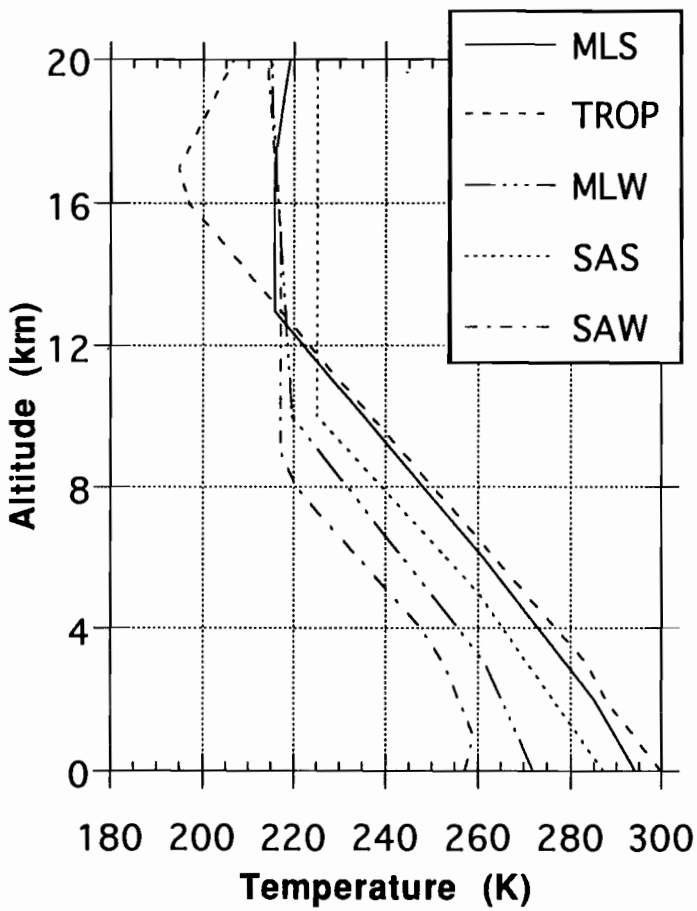

Figure D-2. Composite Plot of Temperature as a function of Altitude for the five AFGL Standard Atmospheres.

This page intentionally left blank.

APPENDIX E
Terminology and Definitions

absolute humidity: mass of water vapor per unit volume present in the atmosphere. It also may be expressed in terms of the pressure of water vapor present.

relative humidity: the ratio of the quantity of water vapor present in the atmosphere to the quantity which would saturate at the existing temperature. It is also the ratio of the pressure of water vapor to the pressure of saturated water vapor at the same temperature

mixing ratio: the ratio of the mass of water vapor in the atmosphere to the mass of dry air. It is typically expressed in units of grams of water vapor per kilogram of dry air.